Doctorate course in:

"Energy and Environment Engineering Science"

XXXV° cycle

Thesis Title

"Design of a thermo-photo catalysis laboratory plant to investigate the plasmonic activation of CO_2"

Dottorando

Gianmarco Miroddi

Supervisore

Prof. Marta Boaro

Anno 2025

Summary

The increasing concentration of atmospheric CO_2 represents a major environmental challenge, directly linked to climate change and ocean acidification. To address this issue, CO_2 valorization through hydrogenation emerges as a promising option, enabling its conversion into chemicals and fuels. This strategy not only reduces greenhouse gas emissions but also promotes the adoption of sustainable energy sources, contributing to a transition towards a low-impact environmental society.

This doctoral thesis investigates the thermo-photocatalytic conversion of CO_2 to methane through hydrogenation, employing rhodium nanoparticles supported on cerium-titanium mixed oxides (Rh/Ce-TiO_x). Motivated by the critical need for scalable CO_2 mitigation technologies, this work pioneers the integration of plasmonic excitation and thermal activation to overcome kinetic limitations in catalytic CO_2 reduction. The Ce-TiO_x support was selected for its good thermal stability, dynamic redox properties (Ce^{3+}/Ce^{4+} and Ti^{3+}/Ti^{4+} cycling), and synergistic interactions with Rh nanoparticles, which collectively enhance charge transfer and intermediate stabilization. An important aspect of this research is the role of Surface Plasmon Resonance (SPR) in promoting the CO_2 conversion over these heterogeneous catalysts.

Surface Plasmon Resonance (SPR) is a phenomenon in which free electrons in a metallic material oscillate in response to incident light. This effect, characteristic of metallic nanoparticles, is particularly relevant in catalysis as it enhances various physicochemical phenomena.

In the field of plasmonic catalysis, SPR increases light absorption and the generation of hot electrons, facilitating charge transfer and the activation of reactive molecules on the catalyst surface. This mechanism has been reported effective also for CO_2 reduction reactions, where hot electrons can facilitate CO_2 molecule cleavage and hydrogenation, lowering energy barriers and improving selectivity toward desired products such as methane or carbon monoxide.

The effectiveness of SPR is strongly dependent on the nature of the material used. Noble metals such as gold, silver, and rhodium exhibit well-defined plasmonic resonances in the visible and near-infrared spectrum, making them optimal for catalytic applications under solar illumination. However, less expensive materials such as copper and metal alloys have also shown a significant SPR effect, broadening the design possibilities for efficient new catalysts.

The ability of plasmonic catalysis to combine photonic and thermal effects enables local heating and hot electron transfer, both critical to enhancing reactivity. This dual effect is especially valuable for metal oxide-supported systems like Rh-functionalized CeO_2-TiO_2, where interactions between support and active metal improve dispersion and catalyst longevity.

Building on these theoretical insights, a dedicated **experimental setup** was designed incorporating a multi-channel gas feed line, a quartz reaction chamber a quartz reaction chamber optimized for light absorption, a 300W Xenon light source simulating solar irradiation, and a mass spectrometer for real-time gas analysis.. This setup enabled systematic evaluation of catalyst performance under controlled thermo-photocatalytic conditions.

The **catalysts synthesis** was carried out using methodologies aimed at maximizing their efficiency and stability under reaction conditions. Mixed cerium and titanium oxides were synthesized via sol-gel, a method that yields materials with high surface area and good dispersion of active elements, a key factor in enhancing reactivity and long-term stability. This technique also allows control over material morphology and porosity, fundamental aspects for ensuring strong interaction between the support and the active catalytic phase.

Rhodium, known for its high activity in CO_2 methanation and its plasmonic effect facilitating hot electron transfer and activation of reactive species, was subsequently deposited using two different techniques: wet impregnation and ball milling, to compare the effects of deposition methodology on metal dispersion and its interaction with the support. Wet impregnation allows for controlled metal distribution, minimizing aggregate formation and optimizing the ratio between exposed surface and available metal for the reaction. Ball milling, on the other hand, facilitates deeper integration between metal and support, positively impacting thermal stability and sintering resistance.

Catalysts characterization was performed using various analytical techniques to determine their structure, porosity, and redox properties. N_2 Physisorption analyses (Brunauer-Emmett-Teller, BET method) assessed the specific surface area and porosity distribution, essential properties for correlating catalysts behaviour under reaction conditions. X-ray diffraction (XRD) was employed to identify present crystalline phases, highlighting any structural modifications induced by synthesis and subsequent thermal treatments. Transmission electron microscopy (TEM) provided detailed information on morphology and Rh nanoparticle dispersion, revealing significant differences between catalysts obtained through the two deposition techniques. Finally, temperature-programmed reduction (TPR) was used to study the system's redox properties, offering insights into the reducibility of active species and their interaction with the support.

A catalytic campaign of tests was systematically conducted to comprehensively evaluate the influence of both operational conditions and catalyst composition on catalytic performance. Specifically, the study aimed to determine the individual and combined effects of the support material, rhodium loading, and illumination on CO_2 methanation reactivity. By varying these parameters across controlled experiments, it was possible to identify their role in modulating catalytic activity, selectivity, and stability under thermo-photocatalytic conditions.

Results showed that the photocatalytic contribution is evident under specific operating conditions. Comparative experiments under dark and light conditions revealed up to a 35% increase in CO_2 conversion under illumination, indicating the role of the plasmonic effect in improving process efficiency. The conversion enhancement was correlated to the generation of hot electrons and charge transfer facilitated by the support.

The comparison of catalysts supported on CeO_2, TiO_2, and mixed cerium-titanium oxides revealed that the Ce:Ti(80:20) system offers the best performance, with higher stability and superior efficiency in methanation reaction. This result was confirmed by diffuse reflectance spectroscopy (DRS) and temperature-programmed reduction (TPR) data, which demonstrated an optimal interaction between rhodium and the support in this specific composition.

Surface catalytic investigations via FT-IR DRIFT enabled the identification of adsorbed intermediate species and clarification of the reaction mechanism under light and dark conditions. The results highlighted the formation of carbonyl and formate species on the catalyst surface, with altered reaction kinetics under illumination.

Finally, metal-support interface analysis revealed that charge transfer between rhodium and the support directly influences reaction selectivity. The presence of oxygen vacancies in mixed supports played a crucial role in facilitating hydrogen transfer and improving catalyst stability over time.

In conclusion, this study confirms the synergistic benefits of thermo-photocatalysis for CO_2 methanation, with enhanced conversion and selectivity achieved through the integration of light-driven and thermal activation mechanisms. The Ce:Ti (80:20) support emerged as the optimal composition, combining favorable redox properties with strong metal-support interaction to achieve high catalytic performance.

The key achievements include:

- Confirmation of the role of illumination in enhancing catalytic activity through the plasmonic effect.
- Demonstration of the influence of support composition on catalyst stability and selectivity.
- Identification of electron transfer between metal and support mechanisms facilitating CO_2 reduction.

However, some limitations remain. Long-term catalyst stability and an in-depth understanding of charge transfer mechanisms require further studies. Additionally, optimizing catalyst synthesis could lead to further performance improvements.

Future research developments will focus on:

- Optimizing catalyst stability to ensure efficiency on an industrial scale.
- Developing new synthesis methodologies to improve metal-support interaction.
- Applying thermo-photocatalysis to other energy conversion processes, such as methanol or synthetic fuel production.

Through a multi-analytic approach, this dissertation provides new mechanistic insights into thermo-photocatalytic CO_2 methanation, representing a valuable step toward the development of practical and sustainable CO_2 valorization solutions for the energy transition.

Contents

1 Introduction 13

1.1 CO_2 environmental challenge 13

1.2 CO_2 Hydrogenation 15

1.2.1 Catalytic Methanation 16

1.2.2 Photo-catalytic Methanation 18

1.3 Thermo-Photo Catalysis 19

2 Surface Plasmon Resonance 20

2.1 SPR Applications 21

2.2 LSPR in Photo-Thermo Catalytic (PTC) CO_2 methanation 25

2.3 Factors Photo-Thermo-CO_2 methanation optimization 29

3 Reaction test bench 32

3.1 Project 33

3.2 Plant building 34

3.2.1 Hardware 34

3.2.2 Software 40

3.2.3 Mass Spectrometer 48

4 Materials and Methods 49

4.1 Catalyst preparation 49

4.1.1 Cerium-Titanium mixed oxide 49

4.1.2 Rhodium metal Functionalization 49

4.2 Experimental reaction conditions 51

4.2.1 Methanation Chemistry and Thermodynamics 51

4.2.2 Temperature parameter 53

4.2.3 Gas flow parameter 54

4.3 Thermo-photo catalytic activity test 55

4.3.1 Light-off experiment evaluation 56

4.3.2 Isothermal steps experiment evaluation 58

4.3.3 Light contribution evaluation 60

4.3.4 Metal loading impact 64

4.4 FT-IR DRIFT 66

4.4.1 Experimental Equipment 66

4.4.2 FT-IR DRIFT investigation 66

5 Material Characterization 69

5.1 Support characterizations ... 70
5.2 Rhodium supported catalytic materials characterizations. ... 80
6 Experimental campaign ... 93
6.1 Experimental Data collection ... 93
6.2 Experimental Data discussion ... 95
6.3 Investigation on metal/support interface characteristics ... 98
6.4 Experimental Hypothesis ... 100
6.4.1 Experimental Setup ... 102
6.4.2 Experimental Data ... 105
7 Conclusions ... 118
Key Achievements and Insights ... 119
Limitations and Lessons Learned ... 121
Perspectives for Future Research ... 121
Closing Reflections ... 122
Bibliography ... 123

Fig. 1.1 Overview of the possible reaction pathways of CO2RR for C1, C2+ products, reproduced from ref. [1] Copyright (2021), with permission from American Chemical Society. 15
Fig 3. 1 Reaction test bench schematic representation: 5 gas feed lines, Xenon Lamp 300W solar simulator, Reactor heating resistance, reactor chamber, Temperature measure of the Chamber and the sample, Mass Spectrometer, moisture unit, a gas spectrometer, a PC station for bench control, a six-way valve for double operational mode. 34
Fig. 3. 2 Reactor project scratch with quotes 35
Fig. 3. 3 Final product of the reactor body, window assembly 36
Fig. 3. 4 300W Xenon Lamp Solar light simulator full spectrum Quantum Design® 37
Fig. 3. 5 Reactor housing assembly 39
Fig. 3. 6 The complete reaction system setup assembly 39
Fig 3. 7 Main Controls panel: a) Software communication initialization, b) Global software Stop and reset, c-d) serial communication port and status, e) Acquire data (Graph and Charts start), f) Save Data (saving path (g) automatic request) 43
Fig 3. 8 Heating control Panel: a)Heater manual control section, b)Chamber, Sample, Resistance temperature indicators, c)Safety alarms led (Critical alarm-software abort), d)PID Controlled variable selector, e)PID parameters monitor, f) Arduino TC module configuration file path 44
Fig 3. 9 Gas Flow Panel: a)Gas feed, single line electrovalves, b)Main electrovalve gas mix, c)Gas parameter manual control switch, d)Gas parameter setting controls: MFC full scale, flowrate SP, MFC gas calibration factor K, flowrate monitor 45
Fig 3. 10Experiment profile set panel: a) Exp. Start button, b)Exp. Pause button, c)Counter re-initialization button, d)Raw progress counter, e)Gas Set-point profile enable, f) Step time, Temperature set-point, Heating slope selector, g)Gas feed flowrates, mix composition (common time reference for each step) 46
Fig 3. 11Graph&Charts Panel: a) Temperature reading Chart, b)Gas feed flowrates chart 47
Fig. 4.1: CO_2 Conversion X% , CH_4 Yield Y% and CO Yield Y% Vs 100-800 °C Temperature range, for pure reactants and products system (solid line) and 80% He diluted system (dash line) 52
Fig. 4.2:Concentration of CH_4 produced in the total gas mix outcoming the reaction chamber and $T_{chamber}$ as a function of time: the controlled variable is a) T_{sample} and b) $T_{chamber}$ 54
Fig. 4.3 CH_4 and CO_2 concentration in the exhausts, showing three consecutive experiments in temperature ramp 15°C/min, 100-400°C, 61%H_2/11%CO_2/28%He 35ml/min 57
Fig. 4.4: Typical structure of an Isothermal steps experiment 58
Fig. 4.5: Gas mix concentration plot Vs Time; Typical experimental design 59
Fig. 4.6: CH_4 Yield% Vs CO_2 Conversion% graph type example 59
Fig. 4.7: Temperature profile measured by T_{sample} thermocouple on the alumina bed in presence or absence of catalyst, respectively black and red lines, in inert atmosphere 61

Fig. 4.8 Rate enhancement Factor due to light contribution as a function of increasing light Intensity for different catalysts – Tchamber =250°C, 61% H2/11% CO2/28% He, ϕ=35ml/min 62
Fig. 4.9 Rate enhancement Factor due to Photothermal and Hot-electron Injection contribution as a function of increasing light Intensity for different catalysts – Tchamber =250°C, 61% H_2/11% CO_2/28% He, ϕ=35ml/min 64
Fig. 4.10 CO2 conversion % Vs CH4 yield % compared at the same reaction conditions: Tchamber =250°C, 61% H2/11% CO2/28% He, ϕ=35ml/min in Dark/Light condition 65
Fig. 4.11 Graphical representation of typical vibration modes of molecules as a consequence of IR absorption 67
Table 5. 1 Catalysts characterizations resuming table. 69
Fig. 5. 1 Adsorption and Desorption (solid and dashed lines respectively) Isotherms for all support materials, pure oxides and compositions of mixed oxides. a) CeO_2 , b)$Ce_{0.8}Ti_{0.2}O_2$, c) $Ce_{0.5}Ti_{0.5}O_2$, d) $Ce_{0.2}Ti_{0.8}O_2$, e) TiO_2. 70
Fig. 5. 2 Pore Volumes as a function of the pore width, distribution of the pores size. 71
Fig. 5. 3 XRD spectra of a) pure Ceria, b) $Ce_{0.8}Ti_{0.2}O_2$, c) $Ce_{0.5}Ti_{0.5}O_2$, d) $Ce_{0.2}Ti_{0.8}O_2$, e) pure Titania; with blue solid and empty diamonds are reported the diffraction peaks of Rutile and Anatase Titania phases respectively, with purple circles are reported the diffraction peaks of Ceria cubic fluorite structure 72
Table 5. 2 Crystalline Structure, Lattice Parameter, and Crystallite Size of TiO_2-CeO_2 Mixed Oxides. 72
Fig. 5. 4 Synthetized CeO_2 TEM image reporting measures of the crystallites 75
Fig. 5. 5 Synthetized TiO_2 TEM image reporting measures of the crystallites 75
Fig. 5. 6 Synthetized CeO_2-TiO_2 (80:20) TEM image reporting measures of the crystallites 76
Fig. 5. 7 H_2-TPR profile of synthetized support oxides; a) CeO_2 , b)$Ce_{0.8}Ti_{0.2}O_2$, c) $Ce_{0.5}Ti_{0.5}O_2$, d) $Ce_{0.2}Ti_{0.8}O_2$, e) TiO_2 76
Table 5. 3 Ceria - Titania MO reduced ratio calculated on the hydrogen consumption measured during the H_2-TPR experiment 77
Fig. 5. 8 Water and CO_2 as product of reduction (left axes) and weight loss % (right axes) as a function of temperature. 78
Fig. 5. 9 Tauc plot of the absorbance Kubelka-Munk function F(R) for Ceria and Titania Oxides – Calculated semiconductor band gap E_g 79
Fig. 5. 10 Tauc plot of the absorbance Kubelka-Munk function F(R) for Ceria-Titania Mixed Oxides – Calculated semiconductor band gap E_g 79
Table 5. 4 Band gap energy in eV calculated with Tauc Method 79
Fig. 5. 11 Adsorption and Desorption (solid and dashed lines respectively) Isotherms for all loaded support materials, pure oxides and compositions of mixed oxides. a) Rh/CeO_2 , b) Rh/$Ce_{0.8}Ti_{0.2}O_2$, c) Rh/$Ce_{0.5}Ti_{0.5}O_2$, d) Rh/$Ce_{0.2}Ti_{0.8}O_2$, e) Rh/TiO_2 81

Fig. 5. 12 XRD Spectra comparison between CeO_2 and TiO_2 supported catalyst (A and B respectively) : a) pure support, b) Rhodium supported catalysts synthetized alternatively by Ball Milling, c)) Rhodium supported catalysts synthetized alternatively by Incipient Wet impregnation 81
Fig. 5. 13 XRD Spectra comparison between CeO_2 -TiO_2 mixed oxides, Ce:Ti(80:20) and Ce:Ti(50:50) respectively A and B: a) pure support, b) Rhodium supported catalysts synthetized by Ball Milling (BM), c) Rhodium supported catalysts synthetized by Incipient Wet impregnation (IW) 82
Table 5. 5 Crystalline Structure, Lattice Parameter, and Crystallite Size of TiO_2-CeO_2 Mixed Oxides supported Rhodium with different techniques. 82
Fig. 5. 14 TPR profile of BM (solid line) and IW (dash line) rhodium supported catalyst on Ceria-Titania pure and mixed oxides (dot-dash line); a) Rh/CeO_2, b) Rh/CeO_2-TiO_2 (80:20), c) Rh/CeO_2-TiO_2 (50:50), d) Rh/CeO_2-TiO_2(20:80),e)Rh/TiO 86
Table 5. 6 Reduction temperature of differently supported IW and BM rhodium samples, for different reducing species at different temperature intervals - H_2 Spillover percentage on different Incipient Wet impregnated samples 86
Fig. 5. 15 TEM images of Rh/TiO_2 a) Ball Milled, b) Incipient Wet impregnation..... 88
Fig. 5. 16 DRS derived Absorbance of Ceria and Titania pure and mixed oxide supports as a function of the wavelenght. a) CeO_2 , b)$Ce_{0.8}Ti_{0.2}O_2$, c) $Ce_{0.5}Ti_{0.5}O_2$, d) $Ce_{0.2}Ti_{0.8}O_2$, e) TiO_2 89
Fig. 5. 17 DRS derived Absorbance of Ceria and Titania pure and mixed oxide supported Rhodium catalysts as a function of the wavelenght. a) Rh/CeO_2 , b) $Rh/Ce_{0.8}Ti_{0.2}O_2$, c) $Rh/Ce_{0.5}Ti_{0.5}O_2$, d) $Rh/Ce_{0.2}Ti_{0.8}O_2$, e) Rh/TiO_2 89
Fig. 5. 18 DRS derived Absorbance of Ceria and Titania pure and mixed oxide supported Rhodium catalysts as a function of the wavelength (solid line), comparison with pure support DRS profiles (dash line). 91
Fig. 6.1 Comparison in Dark(solid) and Light (empty) condition, : Tchamber =300°C, 61% H2/11% CO2/28% He, ϕ=35ml/min, for different supports metal loaded by Incipient Wet impregnation (IW) and Ball Milling (BM) 96
Fig. 6.2: Comparison in Dark(solid) and Light (empty) condition, : Tchamber =300°C, 61% H2/11% CO2/28% He, ϕ=35ml/min, for different Ceria-Titania mixed oxide composition supporting Ball Milling (BM) loaded 4%wt Rhodium. 97
Fig. 6.3: Metal-to-Support Spillover% VS Yield% comparison in both Light and Dark experimental conditions (empty and solid symbols respectively), for a set of catalyst metal loaded at 4%wt by Ball Milling, orange and purple solid lines represent the trend of light and dark experiments respectively. 99
Fig. 6.4 Graphical representation of the whole FT-IR DRIFT in Dark/Light (Lamp ON/OFF)conditions experiment structure. The inert gas is Argon and the total flow is constant 100ml/min, controlled by Mass Flow Controls and valves. A shutter is used to switch on/off the light. 103

Table 6. 2 Reference table of carbonaceous species typically adsorbate in a CO_2 reduction reaction and their FT-IR DRIFT stretching bands. Cabonates: Monodentate (m-), Bidentate (b-), Bidentate bridged (b-br-); Bicarbonates; Formate; Carbonyl species on Rh metal: Linear (mono, geminal or tri-carbonyl), Bridged, Hollow..... 104
Fig. 6.5 illustrates DRIFT spectra of all catalyst samples collected in a 100ml/min 3% CO_2 .in Ar gas flow after 15 minutes of exposition at 50°C. Peaks of main species retrieved are reported, m-C: monodentate carbonate, bi-C:bidentate carbonate, bi-br-C: bidentate bridged carbonate, HC: hydrogen carbonate, F: formate..... 106
Fig. 6.6 Displays the Kubelka-Munk function of the DRIFT spectra collected for all sample at 50°C, with a flow rate of 100 ml/min comprising 12% H_2, 3% CO_2, and 85% Ar in the reaction atmosphere (MIX), with the lamp switched off. 108
Fig. 6.7a Displays CeO_2-Rh Kubelka-Munk function of the DRIFT spectra, in the interval 2300-1000 cm^{-1} collected at 150-200-225-250°C on BG-MIX, with a flow rate of 100 ml/min comprising 12% H_2, 3% CO_2, and 85% Ar in the reaction atmosphere (MIX), with the lamp switched off (blue solid line) and on(yellow(dash)/purple(solid) line) 111
Fig. 6.7b Displays CeO_2:TiO_2(80:20)-Rh Kubelka-Munk function of the DRIFT spectra, in the interval 2300-1000 cm^{-1} collected at 150-200-225-250°C on BG-MIX, with a flow rate of 100 ml/min comprising 12% H2, 3% CO2, and 85% Ar in the reaction atmosphere (MIX), with the lamp switched off (blue solid line) and on(yellow(dash)/purple(solid) line) 112

1 Introduction

1.1 CO_2 environmental challenge

The concentration of atmospheric CO_2 is intricately linked to climate change and ocean acidification [1], primarily due to the physicochemical properties associated with the carbon dioxide molecule. As urbanization and deforestation continue to escalate, there has been a sharp increase in the atmospheric CO_2 levels over the years.

In recent years, carbon dioxide valorization has emerged as a pivotal technology, offering profound implications for both the global economy and the pursuit of a carbon-neutral society. This innovative process involves the conversion of CO_2, a major contributor to climate change, into valuable products with hydrogen. The multifaceted impacts of CO_2 valorization can be understood through its environmental imperative, economic opportunities, role in the energy transition, and potential as a resource for achieving carbon neutrality.

At its core, CO_2 hydrogenation addresses a critical environmental concern by providing a means to capture and repurpose CO_2 emissions. By leveraging hydrogen, a clean and abundant energy carrier, this technology transforms CO_2 into useful compounds, aligning with global efforts to combat climate change and transition towards sustainable practices.

The economic dimension of this research sector is significant, as it opens new opportunities for industry and growth. The creation of a sector focused on converting CO_2 into valuable products, such as synthetic fuels and chemicals, can stimulate innovation, economic development, and job creation. Countries investing in these technologies stand to benefit from the emergence of a green economy.

Furthermore, CO_2 hydrogenation plays a vital role in the ongoing global shift towards renewable energy sources. Utilizing hydrogen produced from clean energy, such as wind or solar power, in the conversion process contributes to the decarbonization of sectors like transportation and industry. This not only accelerates the energy transition but also enhances energy security by reducing reliance on fossil fuels.

As societies strive for carbon neutrality, CO_2 hydrogenation emerges as a versatile resource. The transformed CO_2 can serve as a feedstock for various industries, reducing dependence on fossil fuels and supporting the development of a circular carbon economy. This has the potential to revolutionize traditional production methods and pave the way for a sustainable and carbon-neutral society.

In response to this environmental challenge, significant research efforts have been devoted to mitigating CO_2 through its sequestration from flue gas mixtures, employing various porous adsorbents[3, 4].

Various materials have been explored for their potential in physically adsorbing CO2 on their surfaces. These include metal-organic frameworks (MOFs)[5, 6] , zeolitic imidazole frameworks (ZIFs)[7, 8], porous organic polymers (POPs) [9, 10], porous carbons[11, 12], surface-functionalized mesoporous silicas [13, 14], covalent triazine frameworks (CTFs)[15], covalent organic frameworks (COFs)[16, 17], and more. The goal of these studies is to develop efficient strategies for reducing the concentration of this greenhouse gas and addressing the global challenge of climate change.

Major sources of CO_2 emissions to the environment include various industrial processes, with additional emissions of gases such as nitrogen, water vapor, CO, nitrogen oxides, and sulphur oxides [18]. Despite efforts to sequester CO_2 and store it in underground reserves, this method has limitations, and the potential for underground leaking poses challenges.

To address these issues, researchers have turned their attention to utilizing CO_2 as a C1 source for converting reactive organic molecules into fuels and valuable fine chemicals [19, 20, 21]. This approach offers an alternative to traditional CO_2 sequestration processes [22], potentially providing greater mitigation of CO_2 levels, proceeding toward a carbon neutral industrial architecture. However, the diversity of organic transformations using CO_2 as a reagent presents challenges, especially considering the presence of other gases and water vapor in the processes, which may deactivate catalytic sites and reduce CO_2 utilization efficiency over time.

As seen in the fixation of CO_2 with reactive epoxides or reaction with Grignard reagents, the use of a suitable catalyst or very high pressure is often essential [23]. Unlike CO_2 fixation to a reactive molecule, which enhances the carbon chain length [24, 25], the chemical reduction of CO_2 lowers the formal oxidation state of carbon present in CO_2 and leads to the formation of new C–H and C–C bonds.

In photosynthesis, sunlight provides the necessary energy to overcome the thermodynamic stability of CO_2 and its reduction processes mimic this photosynthetic route, utilizing energy in the form of chemical energy. Both homogeneous and heterogeneous catalysts are extensively studied for CO_2 reduction purposes [26, 27]. Heterogeneous catalysts offer advantages such as recyclability and sustainability, allowing their use in fixed-bed reactors for long-term operation under various reaction conditions.

Currently, CO_2 conversion into fine chemicals accounts for only 4% of total CO_2 emissions, while CO_2 conversion to fuel could potentially reduce about 30%, and notably, it has the potential to almost completely eliminate CO_2 emissions from power plants [28]. This emphasizes the importance of reducing CO_2 into fuels and chemicals for both environmental and economic reasons

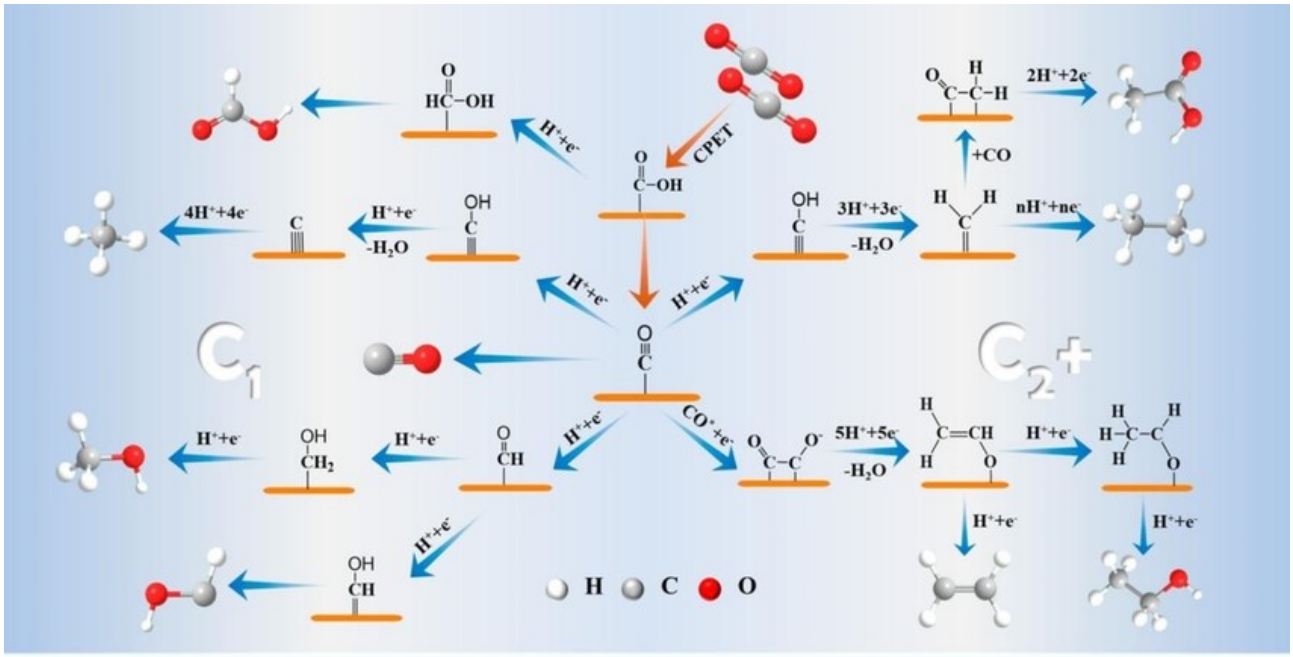

Fig. 1.1 Overview of the possible reaction pathways of CO2RR for C1, C2+ products, reproduced from ref. [2] Copyright (2021), with permission from American Chemical Society.

The resulting CO_2 conversion products include high-value chemicals (Fig.1.1), fuels, petrochemicals, or precursors for more complex chemical production. Utilizing CO_2 as a cost-effective and abundant chemical feedstock is a subject of significant research interest, driven by environmental considerations and economic factors.[29]

Nature maintains a balance in the carbon cycle through simultaneous CO_2 emission and fixation reactions. However, activating CO_2 is challenging due to its highest oxidation state and thermodynamic stability. Overcoming this thermodynamic barrier often requires high-energy substrates and extreme reaction conditions.

1.2 CO_2 Hydrogenation

At atmospheric pressure, complete reduction of CO_2 primarily yields CH_4 via CO_2 methanation and/or CO through a reverse water-gas shift (RWGS) reaction. RWGS produces CO with $\Delta H_{298\,K}$ being 41.2 kJ mol^{-1} and can serve as a feedstock for the Fischer–Tropsch synthesis [29, 30]. Several bioenzymes under physiological conditions show CO_2 conversion to CO [31].

Different mechanisms have been proposed for CO_2 reduction. Wang et al. suggested, through generalized gradient approximation (GGA) functional calculations, that CO_2 dissociates to CO and O in the rate-determining step before hydrogenation [32]. Another proposed mechanism is the Eley–Rideal (ER) mechanism, where CO_2 is initially hydrogenated to COOH* as an intermediate [33]. CO_2 hydrogenation on supported oxides proceeds through the COOH* intermediate, and the surface hydroxyl groups lower the energy barrier for the RWGS reaction.

For catalytic CO_2 reduction with supported catalysts, the support activates CO_2 while the metal activates H_2 [34]. The functionalities of the support and metal determine the dominant pathway, with CO desorption determining the RWGS pathway. Generally, Cu, Pd, and Pt-containing supported catalysts are active for RWGS, while Ni, Rh, and Ru are applicable for methanation. The activity of the metal particle is influenced by the support, oxidation state, particle size, and structure of the supported metal [35].

Previous studies have documented the effectiveness of supported Ru catalysts in the ability to dissociate hydrogen and bind with CO [36]. In the context of reducible supports such as CeO_2 and TiO_2, the metal–support interface plays a crucial role in the reaction, and it has been found to be more favourable compared to alumina. [37]

The phenomenon of strong metal–support interaction (SMSI) was investigated on CeO_2-, TiO_2-, and Nb_2O_5-supported Rh catalysts using CO_2 hydrogenation as a test reaction [38]. Tauster et al. [39] identified SMSI as the result of high-temperature hydrogen treatment of reducible oxides supporting Pt–metals. This treatment caused the reduction of the oxide and induced the migration of sub-stoichiometric oxide onto the metal particles, leading to a decrease in hydrogen adsorption capacity and catalyst activity.

In the case of Rh/TiO_2, a small positive effect was observed under steady-state conditions after high-temperature reduction, while Rh/Nb_2O_5 showed a significant decrease in activity. On Rh/CeO_2, a ~50% reduction in activity was recorded. However, when the reaction was studied using a pulse technique under unsteady-state conditions, a different behaviour was observed. The initial activity of Rh/TiO_2 and Rh/Nb_2O_5 was completely suppressed after reduction at 773 K, whereas an enhancement was observed on Rh/CeO_2. The increase in activity on Rh/CeO_2 was explained by the formation of bulk vacancies in CeO_2. In contrast, Rh/TiO_2 and Rh/Nb_2O_5 lost their activity due to encapsulation by reduced oxides. However, the water and oxygen formed in the CO_2 dissociation process re-oxidized the oxide [38].

The size of metal nanoparticles also affects product formation from CO_2. Smaller Ru clusters exhibit high selectivity for the RWGS pathway, while larger Ru particles show methane selectivity. The pre-treatment effect on the structure of supported Ru catalysts can be used to tune their catalytic selectivity. Low-temperature pre-treatment induces structural changes in Ru catalysts, affecting their dispersibility and CO_2 reduction selectivity [35].

1.2.1 Catalytic Methanation

The CO_2 methanation, first discovered by Sabatier and Senderens in 1902 [40], has been a subject of extensive investigation and development for over a century. Various metals have been explored as catalysts for the hydrogenation of CO_2, leading to a wealth of literature reviews on the subject [41, 22, 42, 43, 44, 45]. Different research groups have reported varied activity orders based on the activities and selectivity of metal catalysts, resulting in the following general order for various metals in CO_2 methanation [46]:

Ru > Rh > Ni > Fe > Co > Os > Pt > Ir Mo > Pd > Ag

Among these catalysts, Ru, Rh, and Ni have consistently exhibited the highest activity and selectivity. Metal-promoted mesostructured silica nanoparticles have been a focus of investigation for CO_2 methanation, with Rh-containing samples showing the highest rate of methane formation. However, on an area basis, Ni emerged as the most active catalyst [47].

On alumina-supported noble metal catalysts, the activity order was observed as Ru > Rh > Pt > Ir > Pd [48]. In another study, the turnover frequency of CO_2 conversion on Rh supported on TiO_2 [49] exceeded that on Ru samples, but others found that Rh/Al_2O_3 activity surpassed that of Pt only at higher temperatures [50]. The highest CO_2 conversion was achieved with supported Rh, compared with Pd and Ni catalysts supported on various oxides (SiO_2, Al_2O_3, and CeO_2) and zeolites (ZSM-5 and MCM-41) under the same experimental conditions [51].

The selectivity for methane formation was found to depend strongly on the metal, with Rh and Ru exhibiting significantly higher selectivity than Pt and Pd. Rh/Al_2O_3 and Rh/CeO_2 showed the highest methane selectivity, followed by Ni/CeO_2. Additionally, 2% Rh/PSAC (palm shell-activated carbon) demonstrated higher activity in CO_2 methanation than 2% Ni/PSAC [52].

The products formed during CO_2 hydrogenation on different metals supported on zirconia were observed to depend strongly on the nature of the metal. Cu and Ag were identified as suitable for methanol production, while Ni, Rh, and Ru predominantly yielded methane. Pd, Re, Pt, and Au produced CH_4, CH_3OH, and CO, with Rh, Pd, Au, and Pt considered less reactive metals [53].

CeO_2-supported noble metals were compared for steady-state activity, dividing the catalysts into two groups: Ru and Rh, which predominantly produced CH_4, and Pt, Pd, and Ir, which mainly produced CO, with CH_4 selectivity below 10% [36].

High-throughput screening methods revealed that Ru, Rh, and Ni promoted methanation, while Pt tended to catalyze the reverse water gas shift reaction. Rh and Ru exhibited the most active methanization, with methanation activity influenced by acidic and redox dopants [54].

In summary, many works consistently highlight Rh as one of the best catalysts for CO_2 hydrogenation, emphasizing its superior catalytic properties at low temperatures, despite the associated high costs. Rhodium remains indispensable for understanding the intricate interactions between the metal and the support, examining surface compounds formed during the reaction, and elucidating the elementary steps of the reaction.

1.2.2 Photo-catalytic Methanation

Titania (TiO_2) stands out as a well-known and extensively studied semiconductor oxide, primarily valued for its chemical and physical properties [55]. As a photocatalyst, TiO_2 generates hydroxyl radicals, making it a potent oxidant capable of oxidizing various organic compounds containing one or multiple double bonds [56]. However, its application on a large scale is limited by the fact that it can only be activated under UV irradiation with a wavelength lower than 387 nm, owing to its large band gap (3.0−3.2 eV). Since less than 5% of solar energy is emitted as UV irradiation, this limitation hampers the widespread use of TiO_2 [55].

The major drawback of TiO_2 in photocatalytic applications is the fast recombination of photo-generated electron/hole pairs (e^-/h^+), leading to reduced photonic efficiency [57, 58]. In recent developments, there has been a growing interest in extending the absorption wavelength range of TiO_2 into the visible light region. This has been achieved through the doping of TiO_2 with various species, such as metals, metal oxides, and nitrogen [59, 60, 61, 62, 63]. Research by Fan [64] highlighted that cerium (Ce)-doped TiO_2, a mixture of anatase and rutile, effectively retards the grain size development of TiO_2, decreases its crystallite size, thereby increasing the specific surface area and improving photocatalytic activity. The redox pair of Ce (Ce^{3+}/Ce^{4+}) acts as an electron scavenger, trapping bulk electrons into TiO_2 and enhancing the photocatalytic activity [65].

Several attempts to photo-reduce CO_2 using semiconducting oxides with different dopants have been made. Jeffrey C. S. Wu et al. conducted a study using a steady-state optical-fiber photo reactor with Cu/TiO_2-coated fibers, reporting increased methanol yield with higher UV irradiative intensity and Cu loadings [66]. Teng-feng Xie et al. [67] investigated hydrogen evolution and CO_2 fixation using a $Pd/RuO_2/TiO_2$ photocatalyst, observing formate as a product. Reza Nematollahi et al. [68] explored the activity of Ni-Bi co-doped TiO_2 in CO_2 methanation under visible light irradiation. The co-doped material showed significantly higher methane yield compared to pure TiO_2 and single-doped samples.

The role of dopants in influencing the characteristics of photocatalysts is evident in various studies. For instance, stabilizing Cu doping in CeO_{2-x} for CO_2 photo-reduction, as reported by M. Wang et al. [69], involves introducing O vacancies into the lattice, altering intrinsic electronic properties, enhancing visible light absorption, and promoting the separation/transfer of photo-generated charge carriers. Transition metals like Co, Fe, Cr, Cu, and Mn are commonly used dopants, theoretically improving light-absorbing properties by introducing extra energy levels into the band gap of TiO_2 [69, 70, 71, 72, 73]. The existence of metal oxide clusters, forming heterojunctions, accelerates the separation efficiency of photo-induced electron-hole pairs, facilitating electron transfer and enhancing photocatalytic activity [74].

Plasmonic Rh nanoparticles exhibit photocatalytic properties, concurrently lowering activation energies and demonstrating strong product photo-selectivity, as demonstrated in the CO_2 hydrogenation reaction. The CO_2 hydrogenation on transition metals at atmospheric pressure involves two competing pathways: CO_2

methanation ($CO_2 + 4H_2 \rightarrow CH_4 + 2H_2O$) and reverse water gas shift (RWGS, $CO_2 + H_2 \rightarrow CO + H_2O$) [75]. It is observed that mild illumination of Rh nanoparticles not only reduces activation energies for CO_2 hydrogenation by approximately 35% below thermal activation energies but also induces a strong selectivity towards CH_4 over CO. Specifically, when subjected to low-intensity (~W cm−2), continuous wave blue or ultraviolet light-emitting diodes (LEDs), the photocatalytic reactions on unheated Rh nanoparticles yield CH_4 with selectivity exceeding 86% or 98%, respectively. The reaction rate is twice that of the thermocatalytic reaction rate at 623 K (350 °C). Interestingly, this high selectivity towards CH_4 disappears when the Rh nanoparticles are not illuminated. This is in stark contrast to plasmonic gold (Au) nanoparticles that catalyze CO production whether illuminated or not. Density functional theory (DFT) calculations suggest that the photo-selectivity of the Rh photocatalyst can be attributed to the alignment of the hot electron distribution with the anti-bonding orbital of the critical reaction intermediate, CHO, thereby activating the CO_2 methanation pathway.[76]

1.3 Thermo-Photo Catalysis

Thermo-photo catalysis is an innovative and interdisciplinary field at the intersection of thermodynamics, photonics, and catalysis, aimed at harnessing light and thermal energy to drive chemical reactions. This emerging technology holds great promise for addressing environmental challenges and advancing sustainable energy solutions. By integrating principles from thermodynamics and photo catalysis, thermo-photo catalysis leverages the synergy between light-absorbing materials and catalysts to enhance the efficiency of chemical transformations.

At its core, thermo-photo catalysis relies on the absorption of photons and the subsequent conversion of this energy into thermal energy, which can drive chemical reactions that may otherwise be energetically unfavorable. This unique approach offers a pathway to overcome traditional limitations in catalytic processes, enabling the activation of specific reactions under milder conditions and with increased selectivity.

The potential applications of thermo-photo catalysis span a wide range, including environmental remediation, sustainable energy production, and the synthesis of valuable chemicals. As researchers delve deeper into the fundamental principles governing this field, the development of novel materials and the optimization of catalytic processes continue to unlock new possibilities for efficient and environmentally friendly chemical transformations.

In this dynamic and evolving field, the exploration of novel materials, the design of efficient catalytic systems, and the understanding of underlying mechanisms are central to unlocking the full potential of thermo-photo catalysis.

2 Surface Plasmon Resonance

Surface plasmons (SPs) refer to coherent and collective oscillations of electrons at the interface between two materials with positive and negative real parts of dielectric functions, such as a metal–dielectric interface. SPs can be categorized into two main types: localized (LSPR) on metal nanoparticles (NP) and propagating surface plasmon polaritons (SPPs) typical of thin films or 2D materials. The interaction between photons and materials is significantly enhanced by the greatly intensified local electric field generated by SPs. This enhancement has led to rapid developments in various fields, including plasmon-enhanced fluorescence, Raman spectroscopy, heat generation, photo-acoustics, photocatalysis, nonlinear optics, and solar energy conversion [77].

SPs originate from coupling between photons and free electrons. Conventionally, SPs are investigated inside metals, such as noble metal gold and silver, with an abundant number of free electrons and resonance wavelength located in the visible and near-infrared regions. This resonance is induced when the frequency of an incident electromagnetic field aligns with the natural frequency of surface electrons oscillating within the potential energy space of positively charged nuclei. The result of SPR is the generation of large scattering cross and absorption sections, along with a substantial enhancement of the electromagnetic field near the surface of metallic nanoparticles.

Metals are commonly regarded as excellent candidates for plasmonic applications, with silver (Ag) being considered the best material due to its low optical loss in the visible and near-infrared (NIR) spectral ranges. However, Ag is prone to oxidation and can experience significant losses due to surface roughness. Gold (Au) is another popular plasmonic material, exhibiting excellent performance in the visible and NIR spectral ranges, along with superior chemical stability under ambient conditions.

While Ag and Au are highly effective, their cost can be a limiting factor, prompting exploration of alternative materials such as copper (Cu) and aluminum (Al). However, both Cu and Al suffer from chemical instabilities under atmospheric conditions, restricting their broader applications. Alkali metals are theoretically ideal for plasmonic applications, but their extreme reactivity to air and water necessitates storage in a vacuum or inert gas, limiting their practical use.

Palladium (Pd) and platinum (Pt) have garnered attention due to their applications in catalytic activities, despite being strongly absorptive in the visible wavelength, making them less ideal for plasmonic purposes.

In addition to pure metals, alloyed metals are extensively considered for plasmonic applications. Alloying different noble metals allows for tuning the surface plasmon resonance (SPR) wavelength. For instance, alloy nanoparticles like $Au_xAg_{(1-x)}$ exhibit SPR over a broad UV–visible spectra range, and the SPR wavelength experiences a red shift with increasing particle size. These alloy nanoparticles, with varying mole fractions, typically display a single plasmon absorption band with a plasmonic strength comparable to composite gold and silver. The plasmon band shows a linear blue shift with increasing mole fractions of silver. [78, 79]

Harnessing the geometric morphologies of metallic nanoparticles and nanostructures is another crucial aspect that is widely explored to shape and manipulate plasmonic properties. Diverse shapes and structures allow researchers to tailor and optimize the plasmonic characteristics of metallic nanoparticles for specific applications.[80]

2.1 SPR Applications

Plasmon-enhanced Fluorescence

It has been extensively studied through experimental investigations and has emerged as a crucial surface-enhanced spectroscopy technique. The fluorescence emitted by a fluorophore is typically characterized by factors such as quantum yield and lifetime. Plasmon resonance can enhance either the excitation or emission of the light emitter. Achieving maximum excitation-emission efficiency involves manipulating the surface plasmon (SP) frequency between the peak excitation and emission wavelengths of the fluorophore.[81] When plasmon resonance is close to the peak excitation wavelength, excitation light can be effectively confined, resulting in the highest excitation efficiency. Conversely, when plasmon resonance is close to the peak emission wavelength, the highest emission efficiency can be achieved by optimizing the distance between the fluorophore and the plasmonic structure. Since the peak excitation wavelength generally differs from the peak emission wavelength, a compromise must be made between optimum excitation and emission efficiencies.

Plasmon-enhanced Raman Spectroscopy

Raman scattering represents a well-established class of nonlinear light–matter interaction processes, wherein photons engage with intermolecular vibrational and rotational motions. [82, 83] Consequently, Raman spectroscopy furnishes versatile tools for exploring molecular vibrations, serving as a distinctive fingerprint for precise chemical analyses and molecular identifications. Despite its versatility, the cross-section of Raman scattering is exceedingly small when compared to the fluorescence process, typically being 15 orders of magnitude smaller. To advance Raman spectroscopy and render it practically applicable, there exists a strong aspiration to develop enhanced Raman spectroscopy with ultrahigh sensitivity, extending down to the single-

molecule level. Such capabilities hold significant appeal for both fundamental research and diverse industrial applications.

Surface plasmons (SP) emerge as an ideal mechanism for augmenting Raman scattering processes. As elucidated earlier, the energy of light can be concentrated at the hot spots on the surface of metallic nanostructures, thereby remarkably intensifying the interaction strength between light and molecules during Raman scattering. Specifically, plasmon-enhanced Raman scattering is under thorough investigation within two distinct categories: surface-enhanced Raman scattering (SERS) and tip-enhanced Raman scattering (TERS). [84, 85, 86, 87, 88, 89]

Plasmon-induced Heat Generation

The excitation of hot electrons through plasmon-enhanced photon absorption is a well-established phenomenon. This process results in the efficient generation of heat due to electron–phonon interactions, giving rise to a burgeoning field known as thermo-plasmonics. [90, 91, 92] Metallic nanostructures, thoughtfully designed, offer control over local or global temperatures under light illuminations, establishing surface plasmons (SP) as potent sources of heat. This capability has paved the way for diverse applications in nanotechnology.

SP, acting as ideal heat sources, has facilitated numerous potential applications, including but not limited to photothermal melting of nanomaterials [93, 94, 95], nanofluidics [96, 97], photoacoustic imaging [98, 99], photothermal imaging [100, 101], cancer therapy [101, 102, 103, 104], drug delivery [105], nanotherapeutics [106], and steam generation. [107]

Upon the excitation of Localized Surface Plasmon Resonance (LSPR) on plasmonic nanostructures, the coherent oscillation of electrons undergoes non-radiative decay, resulting in the generation of hot electron-hole pairs. This process occurs through various mechanisms such as phonon absorption, interband absorption, electron-electron scattering absorption, or the Landau damping process [108, 92, 109]. The hot carriers initially exhibit a non-thermal distribution but rapidly thermalize to a Fermi-Dirac distribution within 100 fs – 1 ps through electron-electron and electron-phonon scattering events, leading to local heating and an increase in lattice temperature. These hot carriers typically possess an energy of about ±1 eV relative to the Fermi level, corresponding to an electronic temperature of thousands of K, which cannot be achieved through heat energy transfer [92].

The development of a Rh/Al nanoantenna catalyst for wide-spectrum photothermal CO_2 methanation has been reported [110], demonstrating an unprecedented CH_4 yield rate and nearly 100% selectivity. This innovative catalyst combines Rh and closely packed Al nanostructures to construct the Rh/Al nanoantenna photocatalyst. In this configuration, Rh contributes abundant active sites for CO_2 methanation, while the

strong Localized Surface Plasmon Resonance (LSPR) effect of the Al nanostructure converts solar energy into hot electrons. This process generates a high surface temperature and strong localized electric fields, effectively activating the absorbed reactants. The synergistic effect of Rh and Al in this nanoantenna catalyst enhances the efficiency of photo-thermal CO_2 methanation across a broad spectrum.

Plasmon-enhanced Photocatalysis

When the electron-accepting orbitals of a nearby adsorbate or semiconductor are accessible, and their energy matches the energy of the hot carriers (i.e., hot electrons or holes), electrons can be injected from the plasmonic nanoparticles into these species [111]. There are two pathways for interfacial electron transfer: the conventional indirect transfer and the recently proposed direct transfer [108, 112]. In the case of indirect electron transfer, electrons are injected to the adsorbate or semiconductor after hot carrier generation, competing with electron-electron and electron-phonon scattering events. The charge transfer mainly occurs toward adsorbate states near the Fermi level due to the energy distribution of hot carriers. In the presence of strongly adsorbed molecules on NP surfaces or adjacent semiconducting material, an additional dephasing channel known as chemical interface damping (CID) becomes possible. CID triggers the direct generation of hot electrons in the electron-accepting orbitals of the adsorbate or semiconductor [108, 109, 112]. CID is induced by the coupling between hybridized unoccupied NP-adsorbate states and excited surface plasmons, accelerating the overall plasmon dephasing process. In contrast to indirect electron transfer, which occurs after hot electron generation, direct electron transfer is completed during plasmon dephasing, on a femtosecond timescale [108]. The direct-electron-transfer process is characterized by higher electron transfer efficiency and lower energy loss compared to indirect electron transfer, which suffers from significant energy loss due to electron-electron scattering [108, 113].

The thermal effect significantly influences photo-catalysis, as an increase in temperature typically accelerates chemical reaction rates following the empirical Arrhenius law. As established earlier, plasmons can be considered a type of heat source characterized by localized spatial distribution and controllable temporal behaviour. Consequently, plasmon-induced thermal effects are anticipated to efficiently assist chemical reactions at the local level. For instance, rhodium (Rh) nanoparticles have already proven effective as thermal catalysts due to plasmon-induced heat generation. [114, 115]

To decipher the microscopic mechanisms of plasmon-induced photo-catalysis, the CO_2 methanation reaction was meticulously designed to discern contributions from thermal factors (including photo-thermal heating or thermal gradients) and non-thermal factors (including hot-carrier-driven reactions, photo modification of the catalyst, or enhanced near-field effects).[116] Experimental results revealed that both thermal and non-thermal mechanisms play a crucial role in significant photo-catalysis effects.[116] Moreover, an ultrafast surface-enhanced Raman thermometry technique was employed to comprehend the dynamics of photo-

catalysis on an ultrafast timescale.[108] Surprisingly, it was concluded that plasmonic photo-catalysis was not primarily attributable to thermal contributions, as ultrafast measurements disclosed rapid energy dissipation from the adsorbates into the surroundings in less than 5 ps.[108] This insight suggests that a better understanding of the underlying mechanisms will be crucial for the future design of highly efficient plasmon-enhanced photocatalysis techniques.

Efficient utilization of hot carriers in plasmonic photochemistry faces challenges arising from the competition between thermalization, back-charge transfer, and charge transfer processes occurring at comparable timescales. Hybrid plasmonic-semiconductor photocatalysts have been developed to partially overcome these limitations, extending the lifetime of hot carriers and reducing electron-phonon scattering effects [117, 118].

Critical aspects and future prospective

In conclusion, in the realm of applied technology, thermo-photo catalysis stands out for its significant aspects and potential prospects. This innovative approach can offer efficient energy utilization and enhanced catalytic activity. The precision it allows in controlling reaction conditions makes it particularly valuable for applications requiring selectivity and specificity, such as fine chemical synthesis.

However, critical aspects need careful consideration for the widespread adoption of thermo-photo catalysis. Material stability and durability are paramount, as the components must withstand high temperatures, intense light, and corrosive environments. Addressing cost and scalability challenges, especially in the manufacturing of advanced materials like plasmonic nanoparticles, is crucial for economic viability. Integration and engineering present additional challenges, requiring seamless coupling between light sources and catalytic materials, as well as efficient heat transfer. Overcoming these hurdles is vital for practical implementation in diverse industries.

Looking forward, prospects hinge on advancements in nanomaterial design, particularly in tailoring structures at the nanoscale for specific catalytic reactions. Interdisciplinary research collaborations will play a pivotal role, bringing together experts in materials science, chemistry, physics, and engineering to unravel the complexities of thermo-photo catalytic systems.

The goal is to translate these advancements into real-world applications. Thermo-photo catalysis holds promise for diverse applications, including sustainable energy production, environmental remediation, and advanced manufacturing processes. As the technology matures, it is poised to offer innovative and sustainable solutions for future energy and chemical transformations.

2.2 LSPR in Photo-Thermo Catalytic (PTC) CO_2 methanation

PTC-CO_2 methanation has garnered special attention since the ground-breaking work by Gratzel and co-workers in 1987 [119]. They discovered that PTC-methanation on titania (TiO_2)-supported Ru/RuOx catalysts can proceed four to five times faster than methanation in the dark (without illumination) at room temperature [119]. In a comparative study on Ru/TiO_2 in 1988, Melsheimer et al. attributed the enhancement in PTC-CO_2 methanation to a thermal effect rather than an intrinsic photochemical process [120]. Subsequently, numerous articles have presented arguments for both sides, debating whether the function of light relies on the ability to generate heat or its synergistic effects with photochemical activation [121, 122].

For instance, Ghoussoub et al. found that the interaction of hot carriers and thermal effects can increase the overall reaction rate in PTC [123]. The significance of each mechanism may depend on the operating environment. Therefore, it is crucial to comprehend the fundamentals of both photochemical and photothermal mechanisms. This understanding can aid in the rational design of catalytic systems for efficient PTC-CO_2 methanation.

Photochemical effect (non-thermal effect)

Most of the PTC-CO_2 hydrogenation catalysts involve transition metal nanostructures with a high free charge density, an unfilled d-band for suitable CO_2 adsorption, excellent hydrogenation capability, and relatively good stability at high temperatures. These features enable transition metal-based PTC materials to strongly absorb light, efficiently generate hot charge carriers, release heat energy, and serve as active catalytic centers for H_2 or CO_2 activation [124]. Therefore, the discussion on the mechanism will primarily focus on transition metal-based catalysts for PTC-CO_2 methanation.

It is also important to note that the physical process of a photochemical effect results from the injection of energetic carriers into surface-adsorbed intermediates or semiconductors through an indirect or direct charge transfer pathway. Moreover, the indirect (or direct) charge injection depends on whether there is a moderate (or strong) interaction of the metal with adsorbed molecules or semiconductors.

Indirect electron Transfer (non-thermal effect)

As previously introduced, when the incident light wavelength is much longer than the size of the plasmonic NPs, the excited plasmon can be confined to the particle surfaces, referring to the Localized Surface Plasmon Resonance (LSPR) phenomenon. LSPR materials can serve as light antennas, creating a high electric field on the particle surface to enhance light absorption and hot charge generation. The reported LSPR particles for CO_2 methanation include some metal NPs, such as noble metals (Au, Ag, Ru) [124, 125, 126, 127, 128, 129], non-noble metals (Cu, Al) [130, 131], and metal-like titanium nitrides (TiN) [132], as well as certain heavily vacancies-doped semiconductors (such as WO_{3-x} and MoO_{3-x}) [133, 109].

The photo-generated hot electrons can be injected from the metal NPs into the antibonding orbitals of adsorbed *CO_2, *H, *HCO, *HCOO, or other species [109, 134, 76, 135] on a timescale of picoseconds [117]. Then, these adsorbates can be chemically activated by coupling with hot electrons, forming transient negative ion species [136, 137], which allows for weakening and even breaking the chemical bonds of critical intermediates for CO_2 methanation [76]. There are some important discoveries on indirect hot electron injection into key intermediates to promote CO_2 reduction [76, 135, 136, 137]. One of the key surface reaction steps of CO_2 methanation is the H2 activation by the H_2 dissociation into H. The hot electrons generated in metal NPs can enter a Feshbach resonance (1σv*) of H_2 molecules adsorbed on the metal surface, promoting H_2 dissociation to generate hydrogen radical *H on the metal surface [137]. Halas et al. have demonstrated that hot electrons generated on Au NPs can indirectly move into the antibonding orbital of molecular H_2, forming negatively charged $H_2^{\delta-}$ species [136]. Ultimately, $H_2^{\delta-}$ species return to their electronic ground state, releasing enough accumulated vibrational energy for the H_2 dissociation.

Additionally, the selectivity of CH_4 over CO during CO_2 methanation can be dictated by the easiness of the hydrogenation of formyl species (*HCO) or the desorption of carbonyl (*CO) intermediate, which is the rate-determining step (RDS) of Sabatier or RWGS reactions, respectively [138]. Liu et al. have discovered that the hot electrons on the photoexcited Rh NPs can selectively activate the important intermediates of *HCO over *CO, resulting in the cleavage of the C-O bond (i.e., favourable for *HCO hydrogenation) over Rh-C bond (i.e., favourable for *CO desorption) [76]. This selective activating *HCO capability enables photo-excited Rh NPs to exhibit a much higher CH_4 selectivity and lower activation energy than the dark condition at the same external temperature [76]. Moreover, with the assistance of time-resolved operando IR spectroscopy, Ma et al. have revealed that the LSPR effect can cathodically polarize the Ag25 clusters by elevating the EF, which can favor the hot electron injection into adsorbed CO_2 forming CO2* or *H_xCO_2 species (RDS), followed by the formation and deep hydrogenation of *H_xCO species into CH_4 [135].

In addition to the metal-based catalysts, some hybrid semiconductors have also manifested the effect of electron transfer for boosting PTC-CO_2 hydrogenation [139, 140, 141, 142]. It is highly debated that light irradiation can tune reaction pathways or intermediate consumption kinetics, which is essential to be clarified. Zhang et al. have experimentally verified that light illumination can alter the reaction pathways of CO_2 hydrogenation over Co-MnO nanosheet catalysts from formate mechanism under TC condition to RWGS + CO-hydro route under PTC condition [141]. In contrast, recent studies have affirmed that light irradiation can facilitate the conversion of critical intermediate species [139, 140, 142]. For example, with the help of isotope-assisted diffuse reflectance infrared Fourier transform spectroscopy (DRIFT-FTIR) studies, Scott et al. have discovered both TC- and PTC- CO_2 methanation on $NiO_x/La_2O_3@TiO_2$ dominantly proceeds in the formates pathway, wherein *HCOO species is the critical intermediate of the RDS [139]. Compared to the dark condition, the visible light-illumination can enhance the amount of *HCOO, which is converted into *H_3CO

species for CH_4 formation [139]. Similarly, for the catalyst of molybdenum carbides, the photo-assisted decomposition of *HCOO intermediates is the main reason for the enhanced CO_2 methanation activity [140]. Therefore, visible light enables overcoming the high-temperature requirement for the direct dissociation of CO_2 under dark [140].

Besides the metal/adsorbates or semiconductor/adsorbates systems, semiconductors can also adopt hot electrons through an indirect injection pathway in metal/semiconductor heterostructures. Hot electrons with an energy higher than the Schottky barrier height (ϕ_{SB}) (i.e., the difference between the EF of metal and conduction band (CB) edges of semiconductors) can transfer from metal to CBs of adjacent semiconductors [117, 143]. The Schottky barrier is formed by the energy band bending of semiconductors due to the charge redistribution between metals and semiconductors for EF equilibria. Only hot electrons with energies above the ϕ_{SB} threshold can inject into CBs of semiconductors for subsequent reactions at the semiconductor surface. The lower ϕ_{SB} promotes more charge carriers to pass through the barrier for participating in chemical reactions. However, it is also crucial that the CB band bending at the interface is strong enough to avoid electrons from returning to the metal, thus ensuring the spatial separation, and extended average lifetime of charge carriers [126]

Direct electron Transfer

Direct electron transfer based on chemical interface damping has been proposed [144], which might enable hot electrons with low energy to tunnel into the adsorbates [145]. The reported near-field effect and direct electron transfer originate from the same physical mechanisms [116]. The lowest unoccupied molecular orbitals (LUMOs) are dominated by the adsorbed molecules' empty orbitals (i.e., the antibonding orbitals) for a strongly molecular adsorption system. In contrast, the highest occupied molecular orbitals (HOMOs) in the complex structure are mainly filled with metal electrons. In the direct transfer method, hot electrons are directly transferred to the strongly hybridized states between the metal substrates and the adsorbed molecules [146]. The in situ ultraviolet-visible (UV-vis) spectroscopy and theoretical studies have shown that the molecular orbitals of CO_2 and the atomic orbitals of Ru or Rh metals can hybridize strongly, forming a CO_2-coordinated metal complex [147]. The apparent photo-enhancement in methanation only occurs for Ru and Rh with strong CO_2 binding strength compared to other metals [147].

Like the metal/adsorbate systems, the prerequisite of the direct electron transfer for metal/semiconductor heterostructures is the strong orbital hybridization between metal and semiconductors, as evidenced by the appearance of an absorption peak in the UV-vis spectrum for Au/CdSe composites [144]. The metal/semiconductor heterostructures with a direct electron injection are found for those systems where hot electrons are generated from the non-radiative damping of surface plasmons in metals. Such a direct hot

electron injection mechanism has been reported for plasmonic metal/semiconductor hybrid materials, such as Au/CdSe nanorod composite [144, 148, 149, 150].

Photo-thermal effect

In competing with the hot electron injection into adsorbed molecules or semiconductors, the electron-lattice collisions between low-energy electrons and phonon modes can release heat, raising the metal lattices' local temperature throughout several picoseconds [76, 151]. Later, this heat can be dissipated from the metal lattice to the environment by phonon-environment scattering on a time scale of 100 ps [140]. Consequently, the hot electrons cool down as transferring energy to lattices and then the surrounding medium, accumulating heat energy macroscopically as temperature rises. Most recent reports on metallic nanostructures-based CO2 methanation have included the systems of Ni/Al_2O_3, Ru/Al_2O_3 [152], Ru/TiN [132], $CoFe/Al_2O_3$ [153], Ni/TiO_2 [154], Ni@C [155], and Co/Al_2O_3 [156]. The reaction temperature can be generally elevated by around 150-300°C with a light intensity ranging from 100 mW cm^{-2} to 620 mW cm^{-2} [157, 152, 132, 153]. It should be emphasized that some oxide semiconductors, in addition to metals, can also serve as the only active component for raising the system's temperature. Similar to mechanisms of those metallic nano-heaters.

In general, he photochemical contributions and thermal heating effect are not mutually exclusive [158], and instead, they can work synergistically to facilitate CO_2 methanation [76, 116, 159, 160]. This synergistic relationship between photo-thermal and photo-chemical effects poses difficulty in decoupling their contributions.

The relationship between light intensity and PTC-CH_4 yield has been studied to investigate the mechanisms [147]. At a low light intensity below 35 mW/cm^2, the temperature rise due to the photothermal effect might be ignored compared to the photochemical contribution [147]. Besides, many studies have concluded photothermal heating or photochemical-driven methanation from the exponential or linear relationship between CH_4 production rates and light intensity [132, 147]. However, such a criterion may not be rigorous. The multiple excitations of the vibrational mode of the adsorbed key intermediates due to hot electron injection can also follow a super-linear dependence on the high light intensity, in contrast to a linear correlation for single excitations of the vibrational mode [132, 76, 161].

Additionally, it is noted that the photochemical pathways can specifically activate the adsorbates and lower the activation energy, which is different from photo-thermal heating [76]. The decrease in the activation energy of methanation generally indicates the role of photochemical contribution. [76]

Some studies debating the photochemical or photo-thermal roles of PTC have been devoted to quantitative analysis through theoretical computation, precise controls on variables, and single-particle- or single-

molecule-level spectroscopy or microscopy characterization [116, 147, 162, 111]. For example, Liu and co-workers have quantified the non-thermal and photo-thermal effects of CO_2 methanation by developing the direct and indirect illumination catalytic systems of Rh/TiO_x catalysts [159]. Besides, Willets et al. have reported using scanning electrochemical microscopy to quantitatively probe the temperature rise at the particle surfaces derived from the shift in the equilibrium potential with the assistance of a mass transfer mold [163]. The development of advanced spectroscopy or microscopy analyses has fuelled the research interest in probing the PTC mechanisms for various chemical transformations [164], which promises a future demonstration of CO_2 methanation systems.

2.3 Factors Photo-Thermo-CO_2 methanation optimization

The efficient catalysts for PTC-CO_2 methanation should exhibit a high light-harnessing ability, high charge density, long lifetime of free charges, high photon-to-heat efficiency, and rich active sites for H_2 splitting and CO_2 adsorption. Meeting all these requirements is challenging in single pristine component catalysts. Strategies of constructing hybrid composites integrating with other components, forming metal/substrate systems, or engineering defects in a single component are effective in improving the PTC efficiency. Hence, those factors, such as the types, sizes, and shapes of metal or substrates, the metal-support interaction, defect effect, and the operational conditions, are essential to be discussed for designing efficient PTC-CO_2 methanation systems rationally.

Metal Effect

The selectivity and activity of PTC-CO_2 conversion into CH_4 generally depend on the nature of metal catalysts, which are believed to exhibit a similar mechanism to the TC process. The *HCO hydrogenation or *CO desorption can affect the selectivity of CH_4 or CO, respectively. The plasmonic Group IB metals (Ag, Cu, and Au) usually exhibit much weaker adsorption capability of $*CO_2$ and *CO than the other Group VIII transition metals (such as Ni, Co, Rh, and Ru), originating from their greater extent of d-band filling states [165] and then poor CO_2 methanation ability [117, 166]. Besides, theoretical studies on a scaling relations analysis, derived from examining the thermodynamic and kinetic parameters based on a microkinetic model, have confirmed that the *O adsorption energy related to the *HCO dissociation barrier can be the descriptor dictating the CH_4 selectivity for a series of metals [138]. Ru, Rh, and Ni metals with more exothermic adsorption energy enable a higher CH_4 selectivity than Pt and Pd [138].

Kim and co-workers have studied the PTC-CO_2 methanation by the catalyst of Ru, Rh, Pt, Ni, and Cu NPs with sizes in several nanometers supported by silica substrates [147]. Only Ru and Rh exhibit the photo-enhanced CO2 methanation activity among the studied metals due to their strong CO_2 binding abilities for a direct hot electron injection [147]. To modify the poor methanation ability of Au, the presence of Ru in RuAu alloys can

increase the adsorption strength of CO_2 and *CO, which is favorable for the *CO deep hydrogenation into CH_4. [124]

Defect Effect

Most pristine metal oxide semiconductors exhibit a wide band gap with weak light-harvesting ability and a lack of catalytic sites, resulting in inferior PTC-CO_2 methanation. One promising strategy is the introduction of suitable amounts of oxygen vacancies (VO) in metal oxides. VO sites in metal oxides can serve multiple functions for PTC-methanation. For example, VO can act as electron-trapping sites to promote electron-hole separation [167], broaden the light absorption spectrum [168, 169, 170], increase the interaction of metal NPs with the oxide support [171], increase metal dispersion [171, 167], and serve as CO_2 adsorption centers with metal or metal oxide clusters. [157, 139, 156, 172, 173] However, an excess of VO amounts can deteriorate PTC performance because they act as recombination centers for photo-generated charge carriers [174]. Hence, an optimized VO amount should be attained to improve CO_2 methanation performance.

Shape Effect

Control over unique geometries of metal or substrate nanoparticles (NPs), such as hollow structures, metallic nanorods, core-shell shapes, and particle-in-tube configurations, has proven effective in tuning the activity of PTC-CO_2 methanation [175, 176]. For example, TiO_2 microspheres with hierarchical hollow mesoporous nanostructures exhibit a considerable acceleration in the kinetics of PTC-CO_2 methanation compared to commercial Degussa P25 TiO_2 [175]. The enhanced CH4 production is attributed to the large mesoporous pores serving as channels for rapid mass transfer and the hollow structure enabling multiple light reflections to enhance light-harvesting capabilities [175].

It is known that small-sized Pt group metal NPs (such as Rh, Ru, and Pt) generally exhibit an LSPR peak in the UV- or near-UV region. In contrast, increasing the particle sizes or changing the morphology, which can alter the charge distribution and dielectric function, might red-shift the peak position to the visible range for driving the reaction. Sastre and co-workers prepared control samples of spherical Ru (~11 nm in diameter) and rod-shaped Ru (~153 nm in length and ~14 nm in diameter) NPs [176]. The LSPR peak of spherical Ru/g-Al_2O_3 is located in the UV region, while the rod-shaped Ru counterpart exhibits strong and broad light absorption across the UV-vis-NIR region, with LSPR peaks at around 400 nm and 650 nm [176].

Metal-support interaction

The interactions between support and metal NPs are essential for PTC since they can adjust the charge redistribution, tune metal dispersion, or form a protective layer on metal surfaces [177, 178]. Different morphologies (cube, rod, and polyhedron) of hydrothermally prepared CeO_2 substrates have been used as the supports for loading an equal amount of Ru NPs through a photo-deposition method to investigate the

effect of interfacial interactions [178]. The cube-like Ru/CeO_2 shows significant visible light-enhanced CO_2 methanation activity, in contrast to the minimal enhancement for the other samples [178]. It is because the strong interfacial interaction between Ru with cube-like CeO_2, as revealed by spectroscopic tests, can promote the electron transfer from CeO_2 to Ru; Then, the electron-rich Ru promotes the H2 spillover to form abundant vacancies in CeO_2 [178]. Similar observations on metal-support interaction-enhanced PTC-CO_2 methanation have been reported [177, 157, 171]. In the case of Ni-TiO_2, their strong metal-support interaction promotes the formation of oxygen vacancies (VO) along with Ti^{3+} species [157]. The strong interaction of Ni NPs with $BaTiO_3$ supports leads to boosted charge transfer efficiency and higher PTC-CH_4 production rates than the Ni/TiO_2 or Ni/Al_2O_3 [177].

Besides the consequence of facilitated charge transfer between metal and supports, strengthening metal-support interaction can benefit the dispersion of metal NPs. It has been reported that the strong interactions between Ni and La in NiO_x/La_2O_3@TiO_2, related to the formation of $NiLaO_3$ perovskite phase, enables a good dispersion of NiO_x particle on La_2O_3@TiO_2 [139]. Such Ni-La_2O_3 interfacial interaction promotes the activation of *HCOO on photo-excited NiO_x and allows the La atoms to reduce the valence state of Ni to zero for the H_2 activation [139]. Additionally, the strong Ru-$Mg(OH)_2$ interactions are attributed to the narrow variable range of Ru sizes (2.3-2.8 nm) with good dispersion even though the loading amount is increased from 1.0 to 11.5 wt% [179]. Therefore, developing efficient strategies to obtain highly dispersed metal NPs is crucial for PTC-methanation.

3 Reaction test bench

To overcome the challenges inherent in our research goals, we undertook the task of establishing a dedicated research bench tailored to the investigation of plasmonic materials in gas-phase CO_2 hydrogenation reactions under atmospheric pressure conditions. Given that our research group had not previously explored this specific area, the development of a novel research setup became essential.

A thorough review of the existing literature on similar systems was conducted to identify widely accepted configurations that could serve as inspiration for designing the necessary hardware. Our focus was particularly on gas-phase CO_2 hydrogenation reactions at atmospheric pressure, while also aiming to create a versatile system for potential future investigations.

Fixed Bed (FB) or Packed Bed (PB) reactors are often a convenient choice in thermocatalytic applications such as CO_2 hydrogenation, enclosed plug-flow tube reactors usually host this kind of Catalyst configuration, for implications the temperature interval observed is 200-500°C range. [180, 35, 181, 182, 183, 184, 185, 186, 187, 188]

In theory, the most favourable operational range for CO_2 methanation is at low temperatures, where both CO_2 conversion and CH_4 selectivity can approach 100%. Nevertheless, the reaction rate is elevated with higher temperatures. Temperatures exceeding 500°C are conducive to the Reverse Water-Gas Shift (RWGS) reaction, so investigations are typically limited to the range below 500-600 °C. Moreover, elevated temperatures necessitate enhanced catalyst stability and may lead to carbon deposition [189].

In accordance with Le Chatelier's principle, CO_2 methanation is more favourable at higher pressures. Within the common temperature range of 200-500 °C, raising the pressure proves effective up to a certain threshold, beyond which further pressure increases become less impactful. A pressure range of 10 to 30 atm is regarded as moderate in terms of catalyst stress, and it is not expected to induce sintering for the catalyst [190].

Furthermore, another important operative parameter to consider is the effect Gas Hourly Space Velocity (GHSV) which is defined as the ratio of the volumetric flow rate of reactants under standard conditions (25 °C and 1 atm) to the total catalyst volume. If the quantities of catalyst and reactants share the same units, GHSV is often expressed in h^{-1} (inverse time). In some cases, GHSV is also denoted in SmL $(g\_cat.h)^{-1}$. A higher GHSV indicates a shorter time during which the reactants are in contact with the catalyst. The latter parameter is crucial to optimize catalyst performance; to increase the contact time, fixed bed catalysts are often packed, unavoidably lowering the exposed external surface in a quartz glass tube.

On the other hand to maximise the exposed surface area, the catalyst needs to be spread as much as possible on a plane as in case of thin film deposition of the photocatalyst[191, 192, 193], the solid/gas interaction happens typically with tangential flow of reagents, high volume semi-batch photo-reactors can be a solution to extend as much as possible the contact time between reagents and the irradiated catalyst. [194, 195, 196, 197, 198]

Designing an experimental setup for photo-thermal catalysis requires careful consideration, especially since conventional systems used for gas-solid heterogeneous catalysis may not be well-suited for light-based applications because of both geometrical (maximization of the catalyst surface exposed to light) and technical limitations of this kind of configurations. Existing solar thermal reactors, exemplified by the design from Palumbo et al., can be adapted for photo-thermal catalysis under concentrated solar irradiation [199]. In a study by Meng et al. [200], a water splitting rig was retrofitted for tandem hydrogen generation and photo-thermal CO_2 reduction using a xenon arc lamp (20 mW/cm_2) as the illumination source. However, a notable drawback of such designs is the absence of a secondary heating system to differentiate between photothermal heating and photo-induced charge transfer effects.

To address this challenge, both Westrich et al. and Tan et al. utilized external heating elements to raise the temperature of the catalyst bed from the base while exposing the top to continuous illumination [201, 202]. Alternatively, Upadhye et al. [203] adapted a commercially available reactor (Harrick Scientific, HVC-MRA-5), initially designed for in-situ spectroscopy analyses, to investigate the impact of visible light illumination on CO_2 reduction by oxide-supported Au catalysts. In these studies, secondary heating systems were employed to achieve temperatures up to 400 – 600°C, enabling the examination of non-illuminated (i.e., dark) thermal catalysis, while minimizing thermal heating from the irradiation sources using specific bandwidth sources and/or filters.

3.1 Project

Based on the concepts discussed above, we opted for a reaction system which could take those points into account with the principal aim of finding the best possible conditions in which experimentally validate thermo-photo catalysis principles in a univocal way, effectively distinguishing between alternative contribution of energy stimuli to the reaction dynamics.

A few points are the pillar on which the project of the system was founded:

- The correct choice of materials to withstand the thermal stress of many reaction cycles up to the maximum operative temperature of 600°C.
- The optimization of the exposed catalyst surface, also granting a sufficient contact time for flexible use is an objective.

- A sufficiently precise measure and control of temperature of both the catalyst bed and the reaction chamber, a sufficient heating power for the heating element to reach the desired maximum operative temperature.
- The light source shouldn't be affected by light distortion caused by erroneous choice of materials present on the light path.
- A multi-line gas feed for calibrations, pre-treatment and experimental operations was considered.
- Safety requirements for safe laboratory operation.

3.2 Plant building

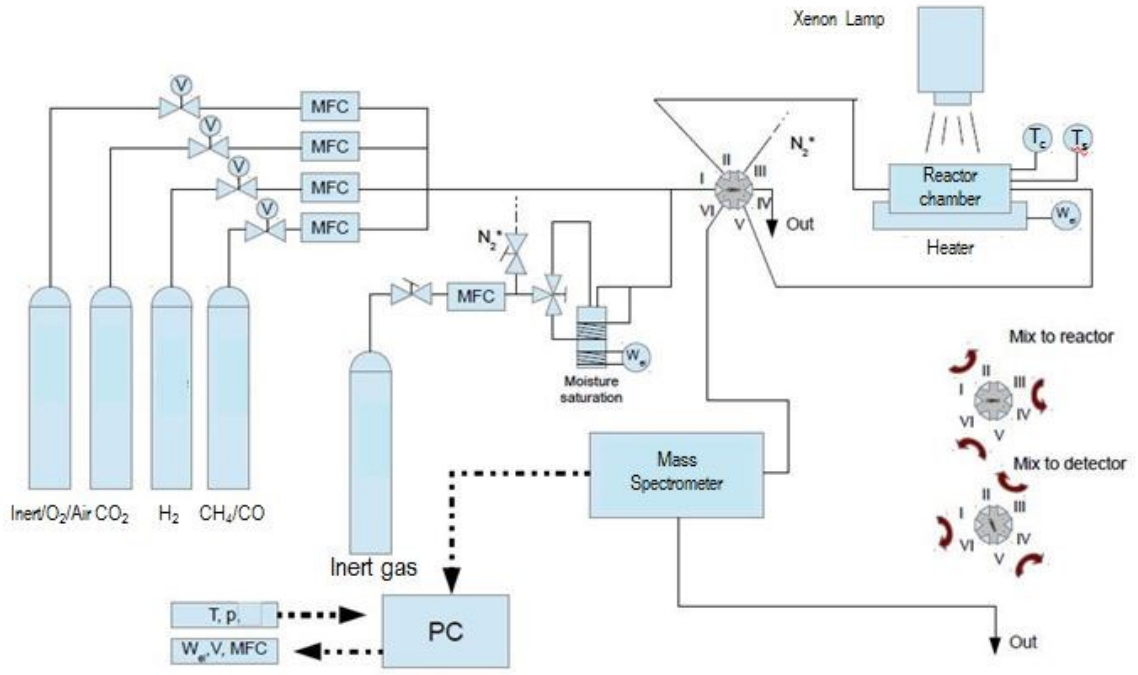

Fig 3. 1 Reaction test bench schematic representation: 5 gas feed lines, Xenon Lamp 300W solar simulator, Reactor heating resistance, reactor chamber, Temperature measure of the Chamber and the sample, Mass Spectrometer, moisture unit, a gas spectrometer, a PC station for bench control, a six-way valve for double operational mode.

3.2.1 Hardware

Gas Feed

In the scheme in Fig.3.1 the reaction system is represented. The gas feed lines are five, each isolated by mean of electrovalves after the two-stage gas pressure regulator directly fixed on the gas cylinder and remote-controlled Mass Flow Controller (MFC) it is also present a further manually controlled inert gas line. It's MFC has 300ml/min maximum operational flowrate, it is the biggest and can be used for rapid flushes of the reaction chamber.

The other four MFC nominal gas flows output are: 100/50/25/15 ml/min. This formats, have been choose with completely different bottom scales to achieve the highest flexibility when composing the gas mix.

The nominal operating relative pressure is about 2 atm. The gas flows are then mixed in a single line which can be operated by mean of the six-way valve directly feeding the Mass Spectrometer, by-passing the reaction chamber. This feature is very useful to check the gas mix stability and calibrations without affecting the catalyst material. The output line is then discharged into the fume hood for safety reason.

Reaction Chamber

The reaction chamber has been projected and realized from scratch. As previously introduced, it has been conceived to withstand temperature up to 600°C without damage. For this reason, the choice of the materials for this element was crucial and a specific attention was given to this aspect. Moreover, its structure had to be unique to fulfill the prefixed requirements. In fig 3.3 it is reported the scratch drawing of the reaction vessel.

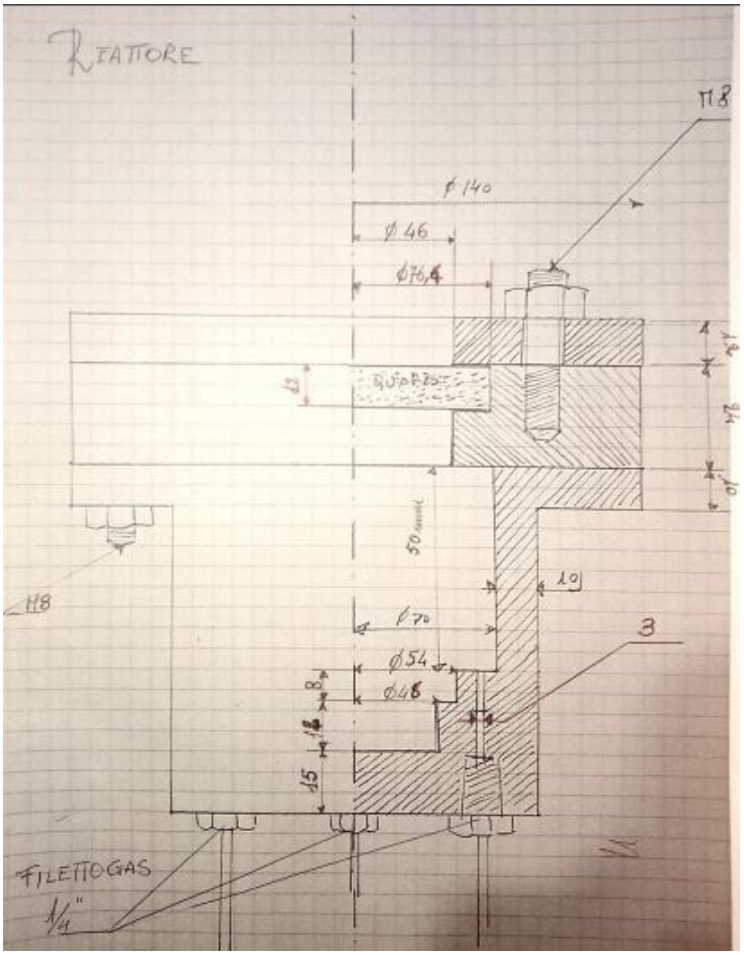

Fig. 3. 1 Reactor project scratch with quotes

The body, screws and nuts of the reactor were custom realized of highly temperature resistant AISI 316 stainless steel. This kind of material, if used within the project limits, is also resistant to hydrogen adsorption induced fragility. The minimum thickness of the walls is 10mm, which can guarantee up to 30 atm pressure in full safety conditions. The total volume of the reactor is about 232 ml.

Moreover, the upper 46mm diameter window was realized in 12mm thick quartz crystal to guarantee the highest transparency possible to the light beam.

3 input channels, 3mm diameter, are placed in a first ring, those can be used as the reactants feed or as the thermocouple insertion channel into the chamber. Another channel is placed in the center at the very bottom of the reactor, this is used as exhaust output, it is placed under a 54mm diameter lodging for a porous alumina foam septum (Porosity 30-35%, Pore size 2.7 to 4.1 microns, Bubble Point 8 to 10 PSI) on which an alumina mat supporting the catalyst bed is placed. This configuration was conceived to force the gas flow transversally with respect to the light exposed catalyst bed plane and, ideally, prolong the contact time.

In the figure below are reported picture of the resulting reactor after production:

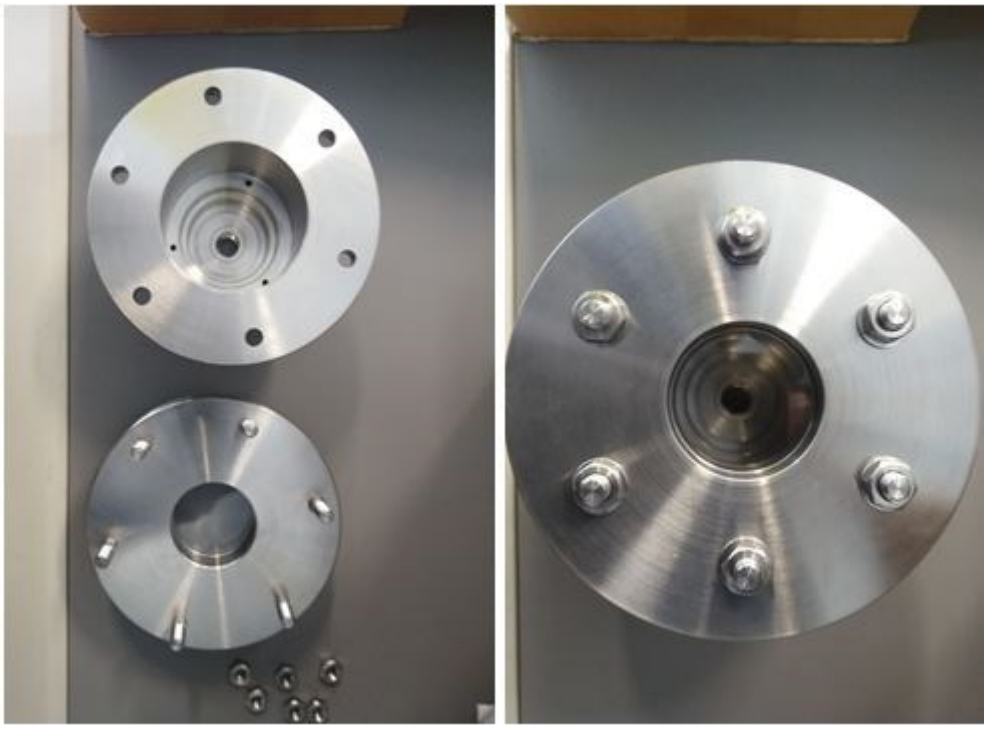

Fig. 3. 2 Final product of the reactor body, window assembly

Gas sealing was provided with hand carved Grafoil gaskets. One placed between the upper plate and the upper interception ring on the 72mm quartz window the other one between the window assembly and the flange of the body.

Light Source

As far as the studies on thermo-photo catalysis are mainly focused on how to efficiently use renewable energy sources in the field of catalysis, we decided to adopt as light source a 300W Xenon solar light simulator produced by Quantum Design® with his own power supply and accessories.

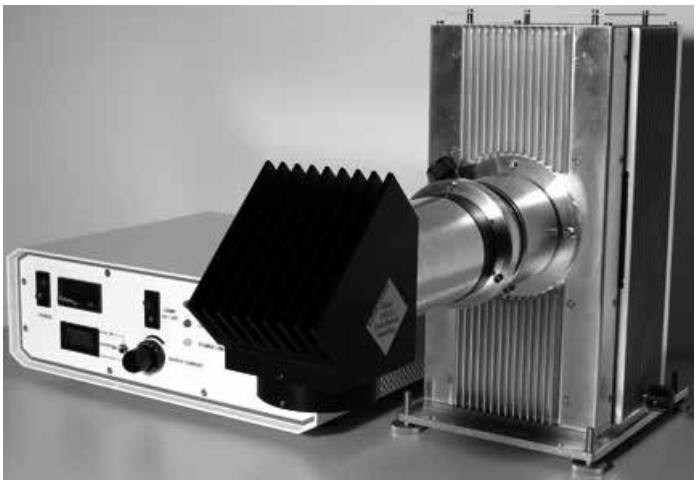

Fig. 3. 3 300W Xenon Lamp Solar light simulator full spectrum Quantum Design®

The illumination system has the following characteristics:

- Lamp type: Xenon short arc, 300 W, ozone free, average life: 1000 h
- Irradiance: 1 sun (min.) @ 180 mm
- Spectral match: AM filters: IEC 904-9, class A
- Working Distance: 160mm (recommended)
- Illumination field: 40 mm
- Beam uniformity: ±10%
- Temporal stability: 1% RMS; ASTM 927-91, IEC904-9, class A
- Input: 90 – 250 VAC; 2.8 A; 48 - 63 Hz

Moreover, accessories were bought to change the configuration of the light beam when needed.

Optical Filters:

- Air mass 1.5-global (direct and diffuse) through atmosphere, 48°.
- Heat reflecting filter, 50mm squared.
- Colored glass filter, GG395 type, 50mm squared, long pass filter.
- UVC blocking filter, 280-4400nm.

Light intensity measure:

- Handheld Optometer with built in touch screen display, carrying case and calibration.
- Attenuated 33 mm^2 silicon detector probe, QNDS2 Neutral Density Filter, W Diffuser, PIR(IPIR) Irradiance Calibration.

Spectral range: 200-1100nm, Measurement Range: $6x10^{-7}$-10 W/cm^2

The Xenon lamp light beam was positioned on the support structure and aligned with the window on the reactor.

Heating element

To ensure a sufficient heating power, starting from the dimensions of the reactor, the volume of material and, consequently, the thermal capacity of the reactor was calculated for the whole body:

$$C_R = 1782\,\frac{J}{K}$$

Which means that ideally to guarantee a minimum heating ramp of 10 K/min, around 300W heating power is needed. The power value was multiplied by 3 to ensure the fulfilling of project requirements with a sufficient safety factor. Band heater, usually employed in extruders heating systems, was chose as heating mantle for the reaction chamber, they can also provide a discrete distribution of temperature on the side wall of the reaction chamber. Many types of these heaters are commercially available, our choice felt on heating elements enclosed in stainless steel of the same type that the reactor body itself to ensure a coherent thermal deformation.

Band heaters with mineral insulation characteristics:

- sheath material Stainless steel max operating temperature 760°C
- Internal diameter 90 mm. (3.54”)
- overall width 63.5 mm. (2-1/2”)
- power supply voltage 230 Vac 50/60Hz single phase.
- power 1200 W.
- single piece construction, expandable.

Nickel stripes, covered with high temperature silicon insulation, were used to connect the power supply terminals of the heating element to the external power source.

Insulating Casing

An insulating safety housing for the reactor was also projected and realized (Fig.3.5). Composed of a 2mm thick stainless steel two pieces box, covered with 30mm thick fire bricks (Gasbeton) sized to fit the box walls. The upper piece was also equipped with two handles and a hole in the center to guarantee the light beam access to the reaction chamber, further holes were also made on the bottom side to fit the gas lines and thermocouples to the reactor body.

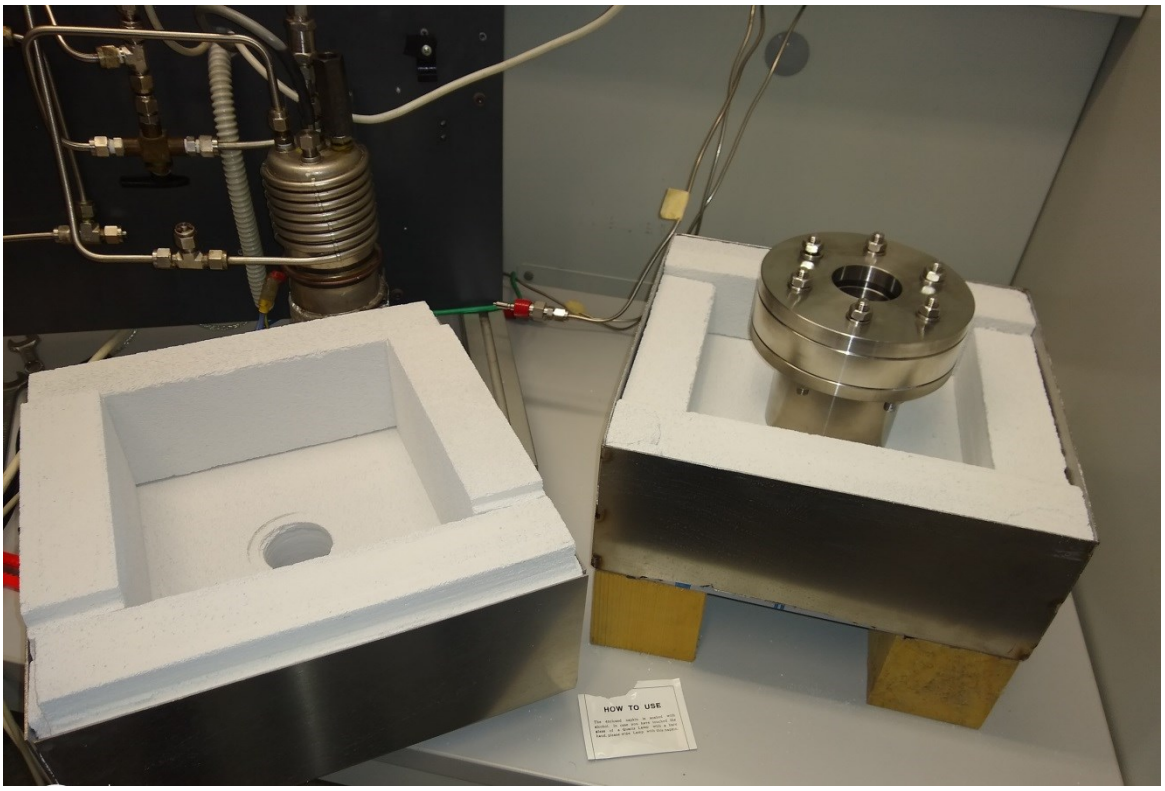

Fig. 3. 4 Reactor housing assembly

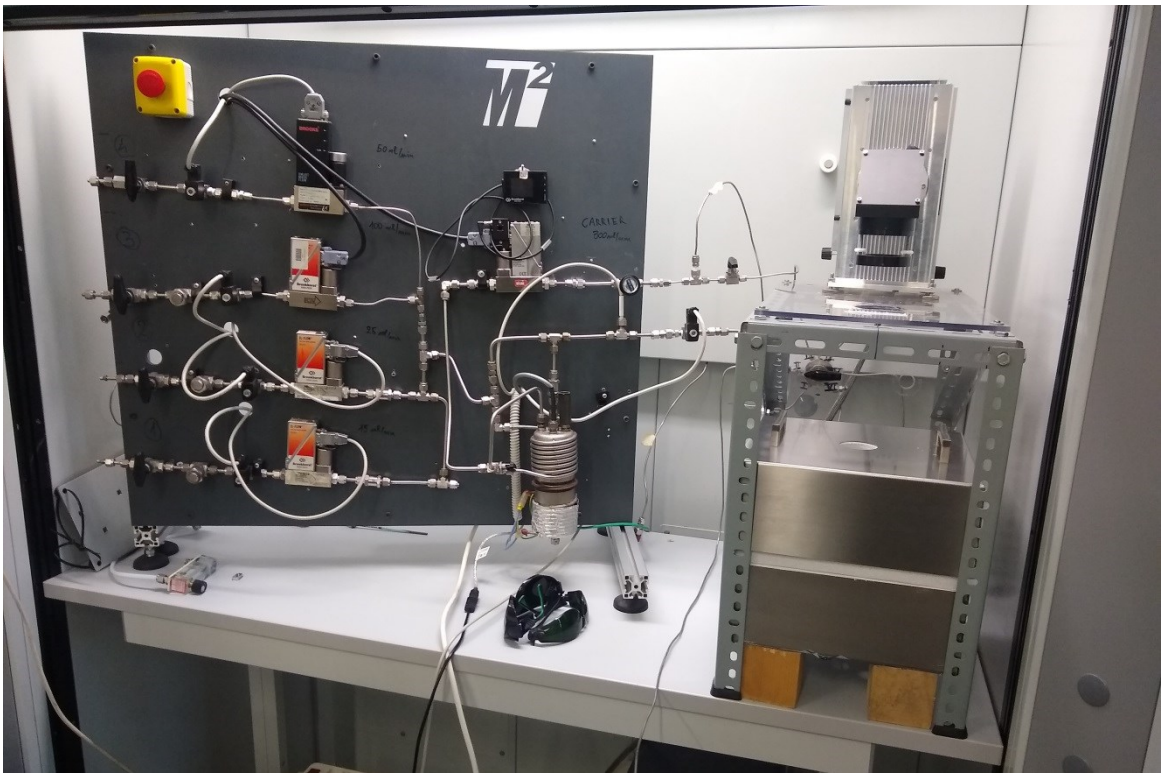

Fig. 3. 5 The complete reaction system setup assembly

3.2.2 Software

The test bench previously described along the chapter needed a software interface to operate the complexity of its components. For this aim more than 400h of work in LabView© programming environment.

LabVIEW, short for Laboratory Virtual Instrument Engineering Workbench, is a graphical programming environment developed by National Instruments. It is widely used for designing and implementing control, measurement, and testing systems, particularly in scientific and engineering applications.

Here are some key features and aspects of the LabVIEW programming environment:

Graphical Programming Language:

LabVIEW uses a graphical programming language called G, where you create programs by connecting graphical icons (nodes) with wires to define the flow of data. The graphical nature of LabVIEW makes it easy to visualize and understand the flow of data and control in a program.

Virtual Instruments (VIs):

Programs in LabVIEW are called Virtual Instruments (VIs), and they can range from simple data acquisition routines to complex control and analysis applications. VIs are created by dragging and dropping nodes onto a block diagram and connecting them with wires.

Front Panel and Block Diagram:

LabVIEW has a dual-pane interface with a Front Panel and a Block Diagram:

- The Front Panel is the user interface of the VI, where you can place controls (inputs) and indicators (outputs).
- The Block Diagram is where you design the logic of the VI using graphical nodes.

Extensive Library of Functions:

LabVIEW comes with a rich library of functions and pre-built nodes for a wide range of applications, including signal processing, data analysis, communication protocols, and more.

Hardware Integration:

LabVIEW is often used in conjunction with National Instruments hardware for data acquisition, instrument control, and automation. It also supports a variety of hardware devices and communication protocols.

Data Flow Programming:

LabVIEW follows a data flow programming paradigm where the flow of data determines the execution order of the program. When data is available at a node, that node executes.

Modularity and Reusability:

LabVIEW promotes modularity and reusability with subVIs (subroutines), allowing to encapsulate functionality into smaller, more manageable components.

Debugging and Profiling Tools:

LabVIEW provides tools for debugging and profiling applications, helping users identify and resolve issues in their programs. It is a powerful tool for engineers and scientists who need to develop applications for measurement, control, and automation. It's widely used in various industries, including academia, research, and manufacturing.

I/O Interface

The hardware/software interface consists of an Advantech ADAM-5000 system, specifically the ADAM-5000/485 variant, which is directly controlled by the control PC using the RS-232 protocol through LabVIEW. The ADAM-5000 system is utilized for the precise control and monitoring of various components in the system:

Control of Mass Flow Controller (MFC):

The ADAM-5000 interfaces with the Mass Flow Controller using analog output signals in the range of 0-10V. LabVIEW communicates with the ADAM-5000 using RS-232 to set and control the desired flow rates.

Electrovalves with Digital I/O:

Digital Input/Output (DI/DO) functionality of the ADAM-5000 is utilized for the control of electrovalves. LabVIEW sends digital signals through RS-232 to the ADAM-5000, controlling the opening and closing of gas feed and main electrovalves.

Temperature Control:

Specific Thermocouple reading module of the ADAM-5000 is employed to monitor chamber temperature (T_c) and sample temperature (T_s). LabVIEW communicates via RS-232 to retrieve the analogic input data, allowing precise temperature control.

In addition to the ADAM-5000 system, an Arduino Mega has been incorporated into the system for expansion and redundancy purposes:

Arduino Mega Integration:

The Arduino Mega serves to expand the system's capabilities with additional Analog Input (AI), Analog Output (AO), Digital Input (DI), and Digital Output (DO) ports.

LabVIEW communicates with the Arduino Mega through USB-adapted serial communication protocols, facilitated by LINX LabVIEW modules, allowing for enhanced control and monitoring capabilities.

Redundant Control:

The Arduino Mega introduces redundancy to the system, providing backup control functionalities. This redundancy ensures system reliability and continued operation in the event of a failure.

Expanded Ports:

The Arduino Mega's additional AI/AO/DI/DO ports expand the system's capacity, allowing for the integration of more devices and sensors in possible future development.

Graphical User Interfaces (GUIs) and control applications

Beyond the hardware/software communication interface, that makes available all the information to be elaborated, the whole system architecture needed to be simple and intuitive.

Flexibility in the use can be a key point while building an experimental setup, for this reason some fundamental parameters can be operated in manual mode, but on the other hand can be also programmed in time to automate the execution of the experiment and replicate it easily and continuously, increasing the productivity and the confidence degree with the data. Moreover, safety alarms and automatic cut-off have been adopted, to operate the system in the best expected conditions. A particularly cautious approach was fundamental while developing the prototype, often the real system has been only simulated to build up the backbone functions which were then integrated with the hardware, along it has been built. A big effort, in fact, went into the realization *on paper* of the system in a first instance, because all assembled bench needed one year of technical time to see the light.

Furthermore, COVID pandemic restriction inconveniences made even harder the process of development, which needed later many hours of software test and debug of the communication and operation of the system to fix some unavoidable bugs, due to the asynchronicity of the hardware and software development.

Main Reactor Control – MRC

The final executable version of the control software has been structured in 5 panels each dedicated to different functions as follows:

- Main Controls
- Heating Control
- Gas Flow Control
- Experiment profile
- Graph and Charts

Fig 3. 7 Main Controls panel: a) Software communication initialization, b) Global software Stop and reset, c-d) serial communication port and status, e) Acquire data (Graph and Charts start), f) Save Data (saving path (g) automatic request)

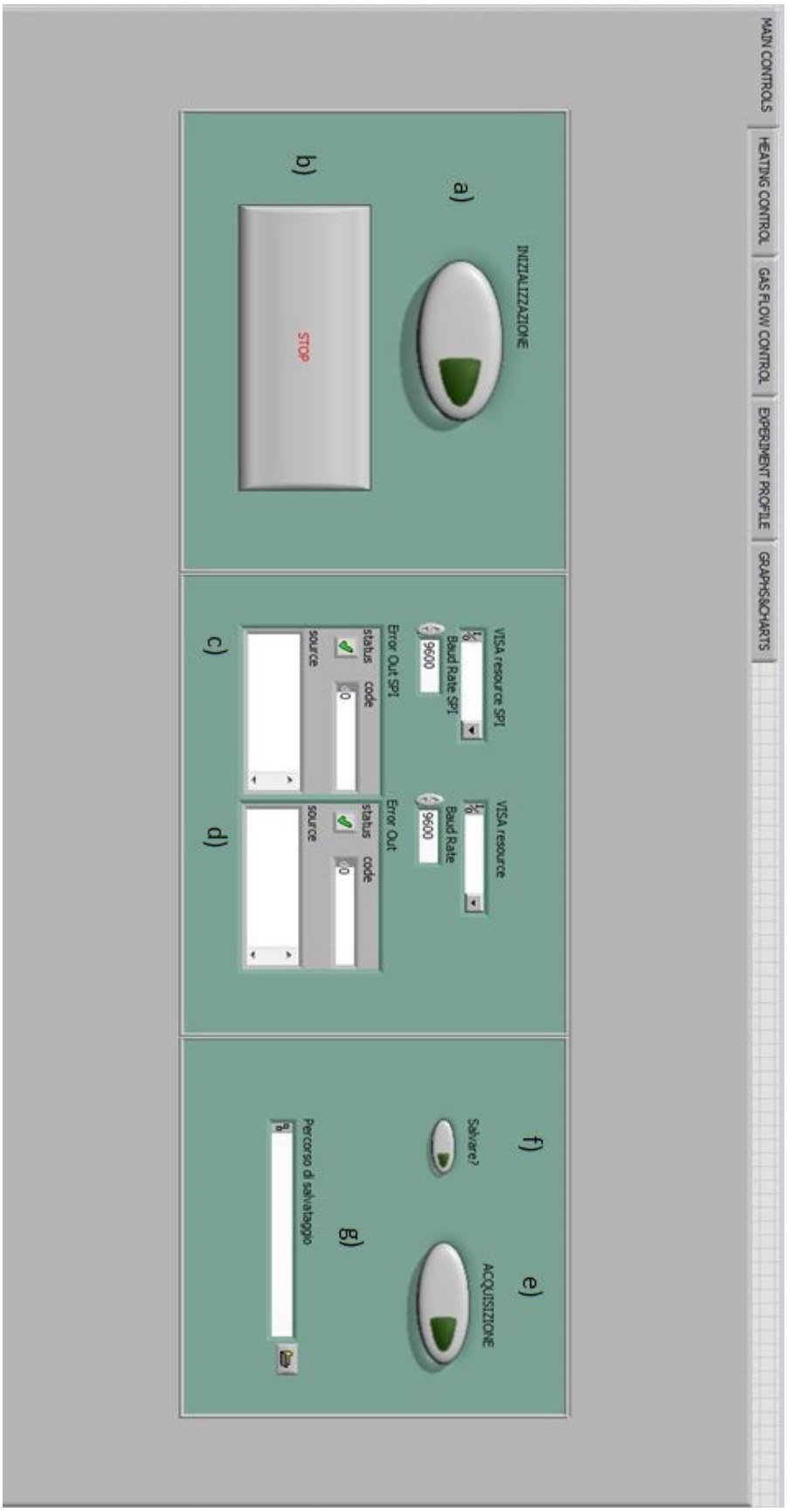

Fig 3. 8 Heating control Panel: a)Heater manual control section, b)Chamber, Sample, Resistance temperature indicators, c)Safety alarms led (Critical alarm-software abort), d)PID Controlled variable selector, e)PID parameters monitor, f) Arduino TC module configuration file path

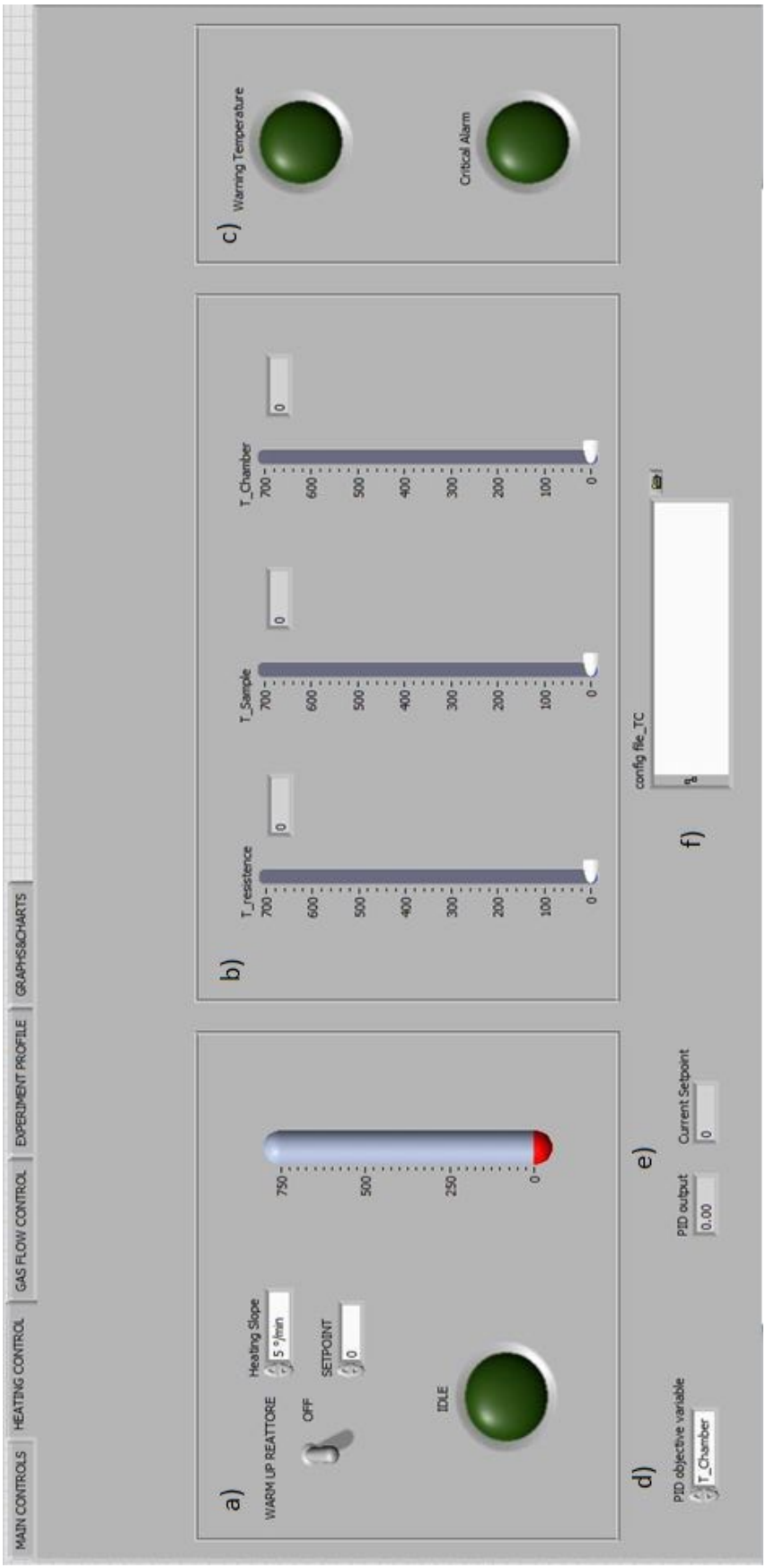

Fig 3. 9 Gas Flow Panel: a)Gas feed, single line electrovalves, b)Main electrovalve gas mix, c)Gas parameter manual control switch, d)Gas parameter setting controls: MFC full scale, flowrate SP, MFC gas calibration factor K, flowrate monitor

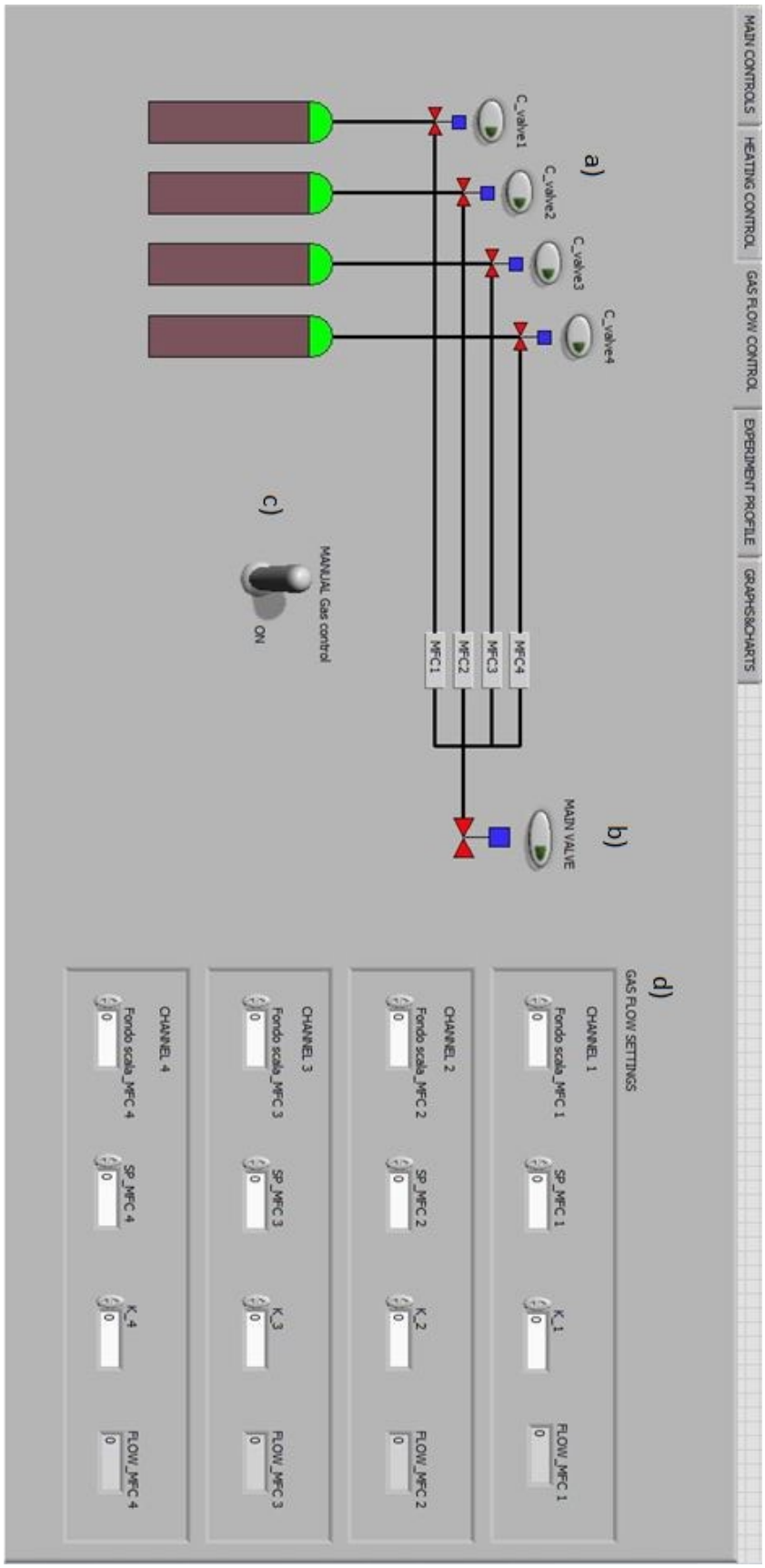

Fig 3. 10Experiment profile set panel: a) Exp. Start button, b)Exp. Pause button, c)Counter re-initialization button, d)Raw progress counter, e)Gas Set-point profile enable, f) Step time, Temperature set-point, Heating slope selector, g)Gas feed flowrates, mix composition (common time reference for each step)

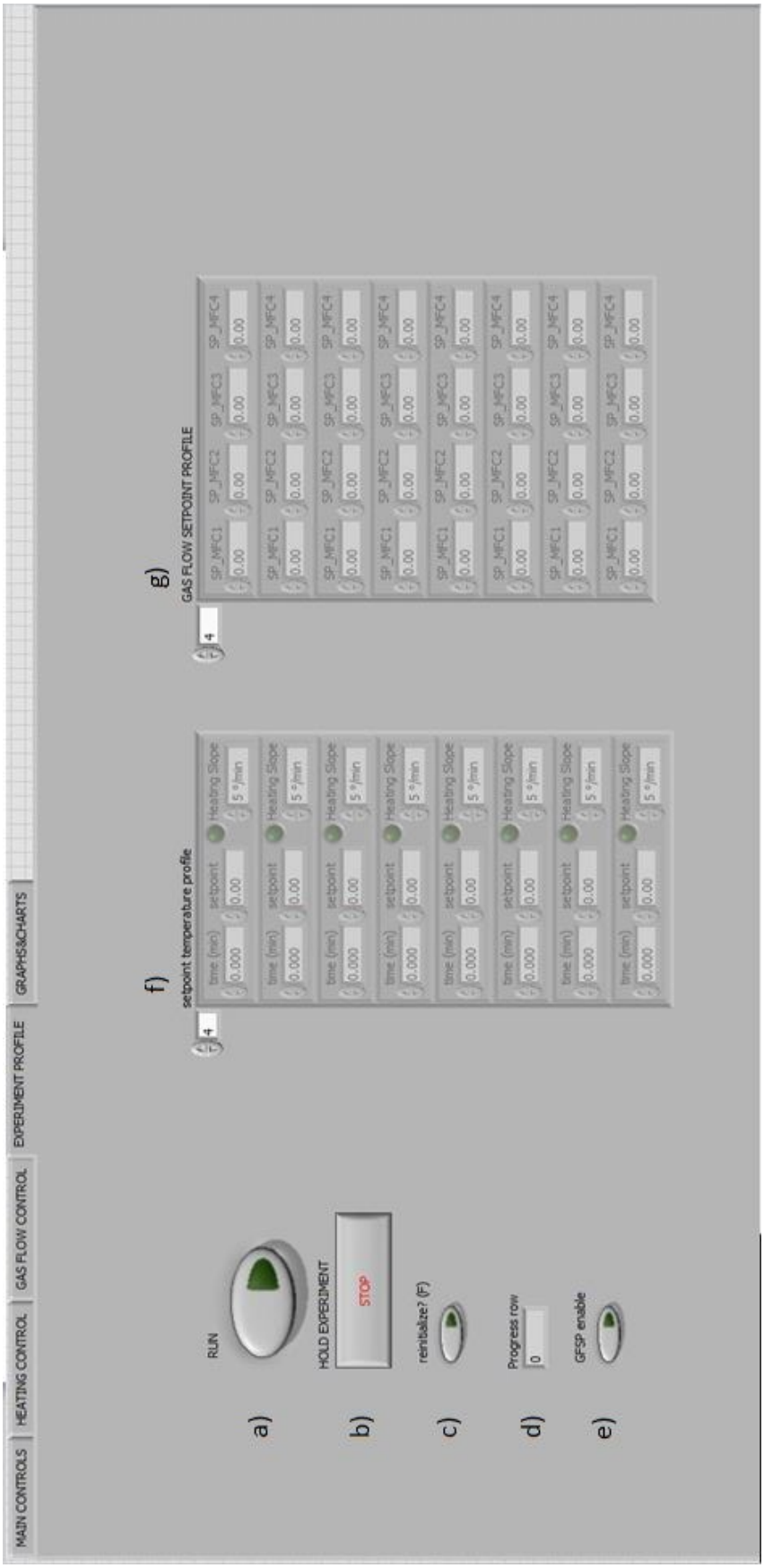

Fig 3. 11Graph&Charts Panel: a) Temperature reading Chart, b)Gas feed flowrates chart

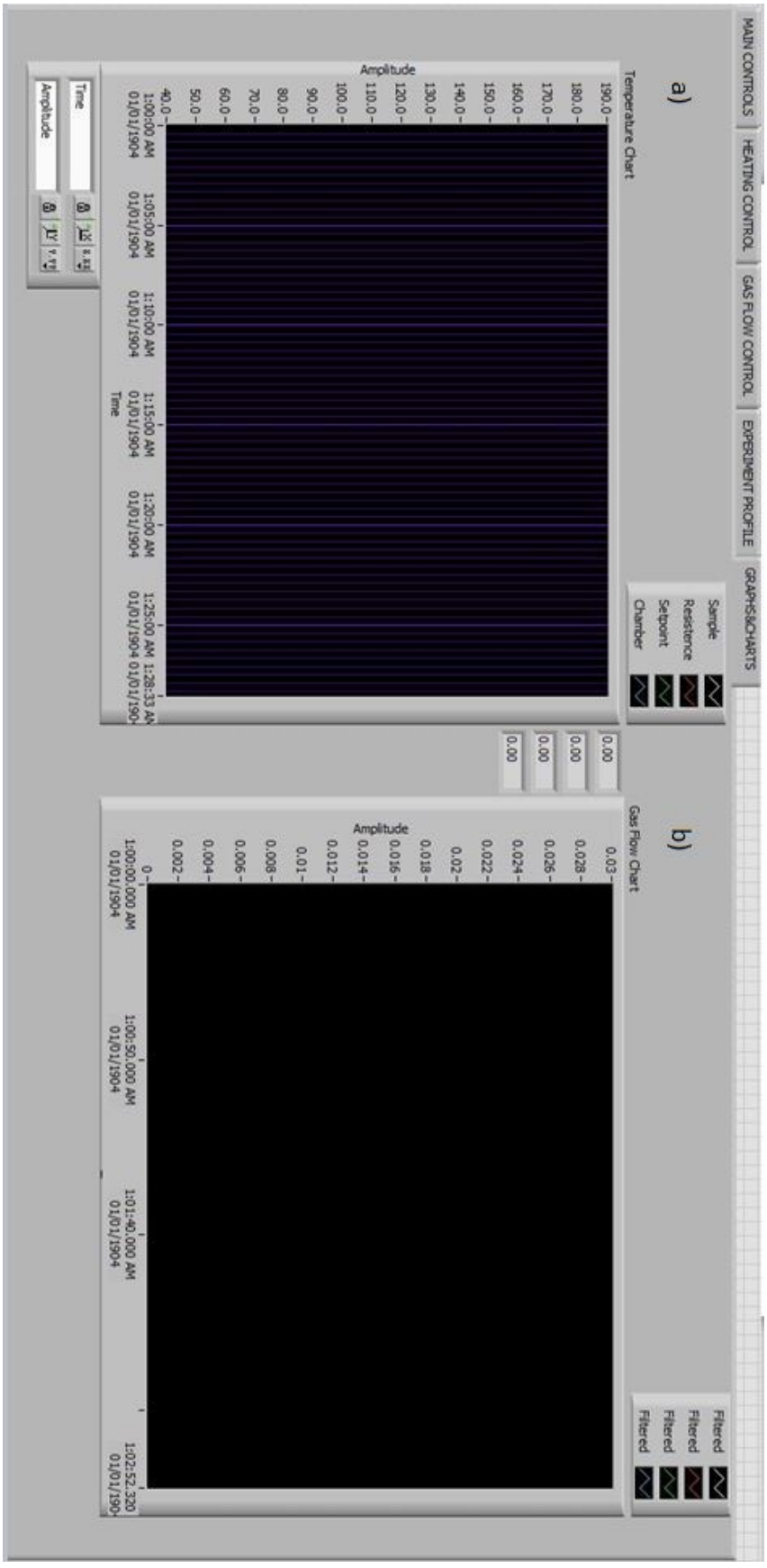

3.2.3 Mass Spectrometer

Catalyst activities were elaborated starting from continuous monitoring of reactants and products concentration in the reactor exhaust mix. This measure was made by mean of a Pfeiffer Vacuum OmniStar Quadrupole Mass Spectrometer (QMS-200). Equipped with a Faraday cup detector and a Channeltron Secondary Electron Multiplier (C-SEM) detector.

In particular SEM mode was used for measurements, which designs can be categorized into two primary groups based on their structure: (1) those employing discrete dynode systems, where electron flux multiplication occurs on separate electrodes known as dynodes, with potentials increasing in a stepwise manner, and (2) those with distributed (continuous) dynode systems, where electron flux multiplication happens along surfaces with a continuous change in potential, such as channel electron multipliers or microchannel plates.

Single-channel secondary electron multipliers (SEMs) serve as dependable and efficient detectors for both positive and negative ions, as well as electrons and photons. These devices consist of a glass tube with an inner diameter of approximately 1 mm and an outer diameter of 2, 3, or 6 mm, crafted from lead-silicate glass with a specialized composition. When appropriately treated, this glass demonstrates electrical conductivity and secondary emission properties. Importantly, these glass surfaces can endure multiple cycles between vacuum and atmosphere without experiencing performance degradation, a characteristic not shared by SEMs employing discrete copper-beryllium dynodes.

A secondary electron multiplier presents several advantages compared to a Faraday cup:

- It greatly enhances the sensitivity of the instrument, leading to sensitivity improvements of up to K = 10 A/hPa.
- It enables the scanning of lower partial pressures at shorter time intervals through the downstream electrometer amplifier.
- The signal-to-noise ratio experiences a substantial boost compared to an electrometer amplifier.
- This enhancement allows for a significant reduction in the detection limit by several orders of magnitude.

The concentrations of reactants and products at the outlet of reactor was calculated through an appropriate calibration of the following fragments: m/e= 44 for CO_2, m/e=28 for CO, m/e= 16 for methane, m/e=4 for He. A commercial moisture trap condensed water at the outlet of reactor. Calibration was performed by a proprietary software procedure with standards mixtures and considering overlapping fragmentations.

4 Materials and Methods

In order to practically apply previously mentioned principles about the photo-thermo-catalysis in general and, in the peculiar case, the surface plasmon's related quantum effect, Ceria and Titania pure and mixed oxide were prepared. Furthermore, in the upcoming chapter, we will delve into the specifics of our experimental setup and methodology. Numerous considerations were carefully weighed when selecting the optimal conditions to ensure the credibility and reliability of our experimental data. Moreover, our objective extends beyond the mere collection of data; we aim to elucidate the role of the Light-Induced Plasmon Resonance (LPSR) effect in the context of a CO_2 methanation reaction. It's worth noting that the general methodology employed in this study has been consistent throughout our entire experimental campaign. This approach allows us to draw meaningful comparisons and insights from the data collected across various experiments and conditions.

4.1 Catalyst preparation

4.1.1 Cerium-Titanium mixed oxide

Pure ceria (CeO_2) and titania (TiO_2) oxides, as well as their mixed oxides with different compositions, were prepared using a sol-gel synthesis method under basic conditions. This synthesis method is reported in the literature as a reliable approach [204, 205]. Mixed oxide compositions $(1-x)CeO_2$-$(x)TiO_2$ were decided to be x=0.2,0.5,0.8 (mol%).

Sol-Gel syntesis

The synthesis involved adding stoichiometric amounts of titanium isopropoxide (Aldrich 99.999%) dropwise, with vigorous stirring, to 20ml Ethanol solution of cerium nitrate hexahydrate ($Ce(NO_3)$-$6H_2O$, Treibacher 99.99%). This resulted in the formation of a thick yellow gel of which thickness is proportional with the content of Cerium, whereas a cloudy white solution is observed when pure Titania is produced with the same preparation. 80ml of additional ethanol where added followed by Ammonium hydroxide 34% solution dropwise until the solution reached a pH of 9. This resulted in the precipitation of a brown coloured solid, while a white solid precipitates when pure Titania is produced with the same method. The precipitate was dried slowly overnight in air at 373 K to remove excess solvent. Subsequently, it was calcined at 973 K in air for 4 hours to produce the mixed oxides.

4.1.2 Rhodium metal Functionalization

As mentioned earlier, our focus was on preparing Rhodium-supported catalysts for the methanation reaction. The size of metal particles and the overall lattice morphology play a crucial role in influencing plasmon resonance phenomena [80]. Leveraging the expertise of our research group, particularly in the field of metal

dispersion and the mechano-synthesis of supported metal nanoparticles [206, 207], we aimed to gain insights into optimizing these catalysts for plasmonic applications.

Functionalization Methodology

The creation of an intimate contact between the nano-dispersed metal and the support has been demonstrated to generate surface arrangements conducive to the catalyst's activity [207]. Achieving such a specific morphology is not easily accomplished, but mechano-synthesis emerges as a promising, simple, and cost-effective method for obtaining an especially active metal/support interface.

The process of mechanical synthesis, as observed in studies on solid-state amorphization [208], reveals interesting phenomena. Mechanical alloying involves repetitive actions like deformation, cold welding, and fracturing among powder particles during milling. This induces various alterations at the atomic level.

During mechanical stress, an increase in vacancies within the crystal lattice occurs, signifying the disturbance and reorganization of atoms in the material. The process also leads to chemical disarray at the atomic level, contributing to the heightened free energy of the crystalline phase. Additionally, nanocrystalline grain boundaries are formed, representing regions where the material's structure transitions from one crystalline orientation to another.

These conditions are especially favourable to the formation of polaritons on the surface of plasmonic metal nanoparticles (NPs). It has been documented that edges and corners play a crucial role in such phenomena, and the morphology significantly influences the plasmon modes [209].

The overall effect of mechanical alloying is the amplification of the amorphous (non-crystalline) state, particularly at the nanometer scale. Amorphization often begins at the edges of crystalline structures and may progress through the creation of a crystalline solid solution, subsequently transforming into the amorphous phase.

One key aspect induced by milling is the generation of point and lattice defects, including vacancies and dislocations. These defects play a role in the amorphization process and have been proposed as the step that limits the reaction rate. [210]

Incipient Wet Impregnation

In the comparison between the ball milling and impregnation techniques, the impregnation method was employed as a reference technique. Initially, the wettability of 300 mg of the support in ethanol was assessed. Subsequently, 29.4 mg of Rhodium acetate was dissolved in an adequate quantity of solvent. This resulting solution was utilized to impregnate the support, achieving a metal loading of 4% by weight. The impregnated

product was then dried at 100°C for 3 hours and subjected to calcination at 450°C in a stable air environment for 2 hours.

Ball Milling

The selection of appropriate milling conditions is crucial for achieving an active surface morphology that effectively exploits the surface plasmon resonance quantum effect. It has been proposed that mild milling conditions may lead to the formation of a broad, amorphous active metal/support interface [211]. To pursue this, we opted for low-energy milling. Specifically, 300 mg of oxide support and 29.4 mg of rhodium acetate solid powder were milled using a Pulverisette 23 Minimill. The milling process took place in a zirconia jar with zirconia balls (15 mm diameter, 10 g) for 20 minutes at 15 Hz. The mixed powders were subsequently transferred into a crucible and calcined at 450°C for 2 hours in a stable air environment.

4.2 Experimental reaction conditions

The objective of this study is to demonstrate the potential of using light as a "booster" for catalytic reactions, specifically in the context of CO_2 reduction reactions. As previously reported in Chapter 2, certain metals that exhibit the surface plasmon resonance effect can also serve as catalytically active species, either independently or in conjunction with active oxide supports. The primary aim is to distinguish the distinct contributions of various catalyst properties. To simplify the inherent complexity of the system, given that this work serves as an initial step towards a more comprehensive and long-term project, we opted to focus on the simplest CO_2 reduction reaction, which is methanation. This choice allows us to compare our results more extensively with existing literature. Moreover, catalyst development typically emphasizes achieving high selectivity for CH_4. Nevertheless, improving conversions at lower temperatures remains a significant objective. Furthermore, it's crucial to recognize that several reaction conditions, such as temperature, pressure, Gas Hourly Space Velocity (GHSV), can exert significant influences on both CO_2 conversion and methane selectivity.

4.2.1 Methanation Chemistry and Thermodynamics

Methanation, as the name itself recalls, is the exothermal reaction (Eq. 4.1) in which one mole of CO_2 gas reacts with 4 moles of H_2 gas to produce 1 mole of CH_4 gas and 2 moles of H_2O_{vap}:

$$CO_2(g) + 4\,H_2(g) \rightarrow CH_4(g) + 2H_2O(g) \qquad \Delta H = -165\frac{kJ}{mol} \qquad \text{(Eq. 4.1)}$$

The most widely accepted mechanism of the methanation reaction is the combination of an endothermic reverse water gas shift (RWGS) reaction and an exothermic CO methanation, as shown in equation 4.2 and equation 4.3, respectively.

$$CO_2(g) + H_2(g) \rightarrow CO(g) + H_2O(g) \qquad \Delta H = 41\frac{kJ}{mol} \qquad \text{(Eq. 4.2)}$$

$$CO(g) + 3H_2(g) \rightarrow CH_4(g) + H_2O(g) \qquad \Delta H = -206\frac{kJ}{mol} \qquad \text{(Eq. 4.3)}$$

By mean of HSC-Chemistry software, species amounts at the thermodynamic equilibrium were calculated as a function of the Temperature value (100-800 °C), this calculation was executed for a volume of pure reactants or in presence of 80% He gas as a diluent. Moreover, data were further labored to calculate conversion X% of CO_2, selectivity S% and yield Y% to CH_4 as the following expressions show:

$$X\%_{CO_2} = (1 - \frac{CO_2[mmol]}{CO_2[mmol] + CH_4[mmol] + CO[mmol]}) \times 100 \qquad \text{(Eq. 4.4)}$$

$$S\%_{CH_4} = \frac{CH_4[mmol]}{CO[mmol]+CH_4[mmol]} \times 100 \qquad \text{(Eq. 4.5)}$$

$$Y\%_{CH_4} = \frac{X\%_{CO_2} \times S\%_{CH_4}}{100} \qquad \text{(Eq. 4.6)}$$

The data obtained were then plotted as follows:

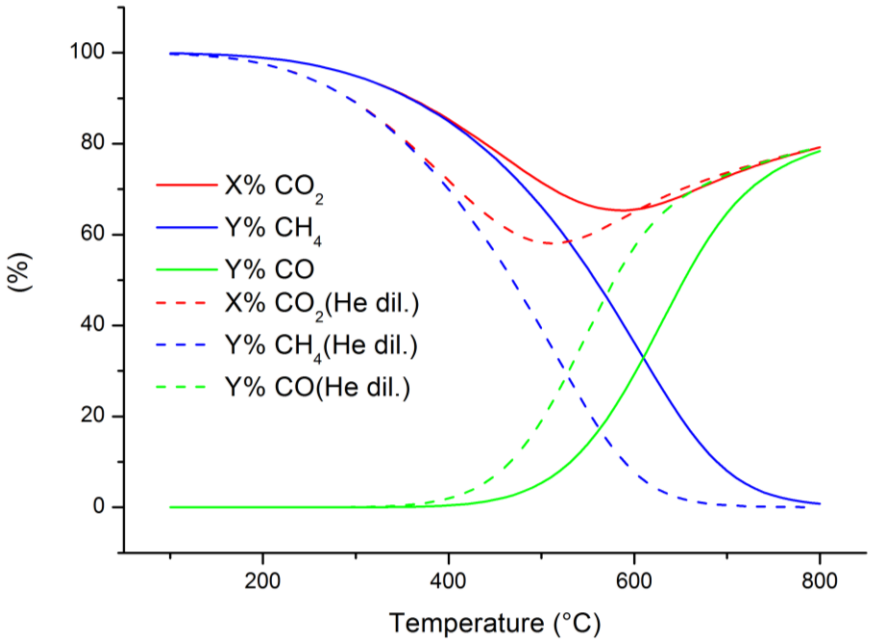

Fig. 4.1: CO_2 Conversion X% , CH_4 Yield Y% and CO Yield Y% Vs 100-800 °C Temperature range, for pure reactants and products system (solid line) and 80% He diluted system (dash line)

The overall reaction in equation 4.1 is favored at lower temperature, but due to kinetic limitations, a catalyst needs to be utilized [212]. Carbon deposition theoretically does not occur if the H_2/CO_2 ratio is equal to or higher than the stoichiometric ratio [213]. Furthermore, it's important to acknowledge that the reduction temperature required for the active metal is significantly lower than the reaction temperature, as evidenced by Temperature-Programmed Reduction experiments conducted with hydrogen (H_2-TPR). This understanding

leads us to consider the use of a hyper-stoichiometric reaction gas mixture. Such a mixture would have the potential to fully reduce the metal catalyst even before reaching the reaction conditions. This could render a pre-reduction step unnecessary, streamlining the process and ensuring efficient utilization of the catalyst.

4.2.2 Temperature parameter

In theory, the most favorable temperature range for CO_2 methanation is at lower temperatures, where both the conversion of CO_2 and the selectivity for CH_4 can approach nearly 100%. However, it's important to acknowledge that as the temperature increases, the rate of the reaction also accelerates leading to higher conversions and consequently yields. Temperatures beyond 500 °C are more conducive to the Reverse Water-Gas Shift (RWGS) reaction, which is why investigations typically avoid operating above the temperature range of 500-600 °C.

Several critical reasons underlie this temperature constraint:

1. **Catalyst Deactivation**: Temperatures exceeding 500 °C can induce catalyst deactivation due to sintering, a phenomenon where catalyst particles agglomerate and lose their catalytic activity.
2. **Carbon Deposition**: Higher temperatures can promote the deposition of carbon on the catalyst surface. This carbon accumulation can obstruct active sites on the catalyst, diminishing its effectiveness.
3. **Temperature Control**: Precise temperature control is imperative in large-scale operations because the exothermic nature of the methanation reaction can lead to apparent temperature increases. This means that even if the process begins at a lower temperature, the heat generated by the reaction can cause a significant temperature rise.
4. **Catalyst Stability**: Elevated temperatures necessitate catalysts with enhanced stability to endure the rigorous conditions and uphold their catalytic activity over time.

The temperature range we decided to work with in our experimental campaign was 200-400°C and specifically the sample tested were overall compared at 250°C. Moreover, as outlined in the description of the experimental hardware, the reaction chamber was equipped with two separate thermocouples, denoted as $T_{chamber}$ and T_{sample}. $T_{chamber}$ was responsible for monitoring the temperature at a location sufficiently distant from the catalyst bed, while T_{sample} was positioned in direct contact with the catalyst itself. The control logic for the heater was programmed to select which of these two temperature measurements to use as feedback for the temperature control loop. It is essential to emphasize the significance of making the correct choice regarding this temperature measurement. The choice of temperature measurement source is critical because it directly influences the control of the reaction chamber's temperature. Accurate temperature control is paramount for ensuring the reliability and reproducibility of experimental results, especially in catalytic studies where even slight temperature variations can significantly impact the reaction kinetics and outcomes. Therefore, understanding this temperature measurement selection is crucial for interpreting and assessing the experimental data accurately, as shown in the following figures.

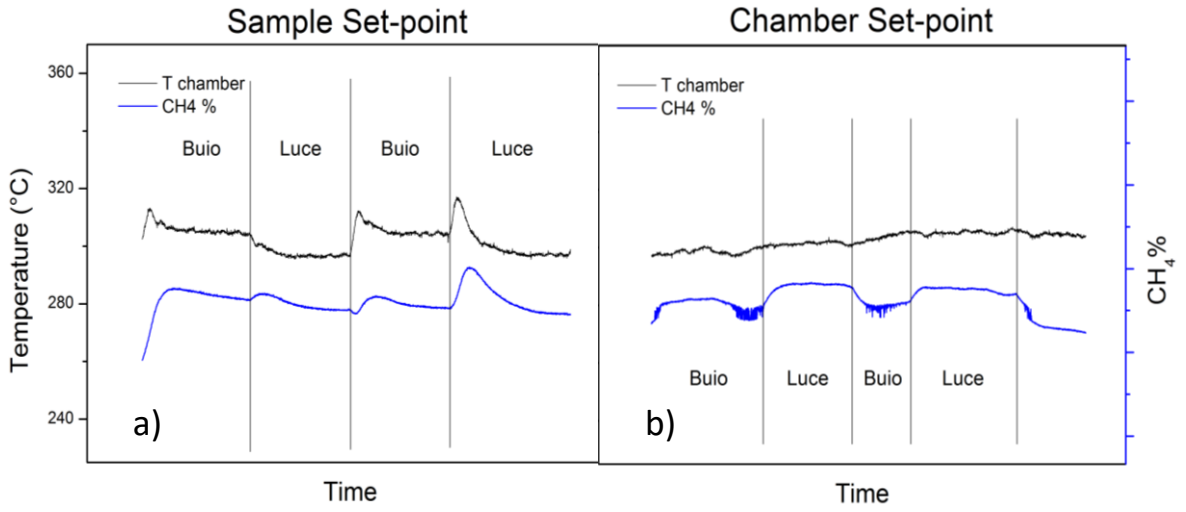

Fig. 4.2:Concentration of CH_4 produced in the total gas mix outcoming the reaction chamber and $T_{chamber}$ as a function of time: the controlled variable is a) T_{sample} and b) $T_{chamber}$

In the case depicted in Figure 4.2a, the control logic monitors T_{sample}. When the light is switched on, the catalyst heats up due to the photothermal effect. In response to this temperature increase, the control logic reduces the heating power supplied to the system. As a consequence, the temperature in the chamber decreases, which leads to a reduction in the reaction rate. This decrease in the reaction rate results in a lower concentration of the product being produced. In contrast, in the case shown in Figure 4.2b, the control logic is set to monitor $T_{chamber}$. When the light source is activated, the chamber's temperature remains stable because the heating power supplied to the system is not adjusted. Consequently, the increase in the reaction rate due to the contribution of light is clear, and the reaction proceeds at a higher rate. In conclusion, the choice of whether to control T_{sample} or $T_{chamber}$ as the temperature feedback parameter has a significant impact on the reaction dynamics when light is introduced. Monitoring T_{sample} results in a decrease in heating power and a subsequent reduction in the chamber's temperature and reaction rate, while monitoring $T_{chamber}$ maintains a stable temperature, allowing the light-induced enhancement of the reaction rate to be more apparent.

4.2.3 Gas flow parameter

The primary objective of examining the two extreme cases in Figure 4.1 was to explore the influence of Gas Hourly Space Velocity (GHSV) on the theoretical limits of a chemical reaction, specifically concerning the dilution of reactants. This investigation aimed to establish the experimental conditions and boundaries for further research on the actual case under study. GHSV is defined as the ratio of the volumetric flow rate of reactants at standard conditions (25 °C and 1 atm) to the total catalyst volume. It is commonly expressed in h-1 (inverse time), but it can be also expressed in SmL (gcat.h-1). The key implication of GHSV is that a higher value implies a shorter contact time between the reactants and the catalyst, which can impact reaction kinetics and product formation. In the specific study conducted by Abate et al. [214], the researchers investigated how GHSV affected a particular catalyst, Ni/Al_2O_3-TiO_2-CeO_2-ZrO_2, in a chemical reaction. The

reactant gas used had a H_2/CO_2 ratio of 4 and was diluted with 87.5% N_2. The investigation covered a temperature range from 250 to 400 °C. The findings can be summarized as follows:

- At temperatures exceeding 350°C, both CO_2 conversion and CH_4 yield were nearly identical and approached equilibrium, indicating that thermodynamics largely governed the reaction under these conditions.
- Conversely, at temperatures below 350 °C and with reduced GHSV, significantly higher CO_2 conversion and methane yield were observed. This suggests that at lower temperatures, the reaction operates below thermodynamic equilibrium, and lower GHSV values promote higher CO_2 conversions.
- While CO selectivity data did not vary substantially at different GHSV values, a higher GHSV resulted in a slightly higher CO yield. This outcome can be attributed to the reduced likelihood of CO hydrogenation at higher GHSV values.

The impact of GHSV on a specific catalyst's performance in a chemical reaction can be crucial. For the reasons mentioned above, being likely to maximize the methanation reaction, the gas mixture chosen for our work was composed of 61% H_2/11% CO_2/28% He, with a total flow rate φ=35 ml/min as the best compromise with the possible gas feed setup.

4.3 Thermo-photo catalytic activity test

Given the defined experimental conditions mentioned earlier, we needed to establish the appropriate experimental procedures to gain a better understanding of the phenomena associated with a typical thermo-photo catalytic activity test. To achieve this goal, we explored two distinct methodologies:

1. **Light-Off Experiment**: This method involves a temperature-programmed ramp within the temperature range we intended to explore. The system is heated at a specific heating rate while being exposed to the reaction mixture, and this is done alternately in both light and dark conditions. This approach allows us to observe how temperature variations affect the catalytic activity with and without light.

2. **Isothermal Steps Experiment**: In this approach, we conducted a series of discrete temperature steps within a desired temperature range. Each temperature step is maintained for a sufficient duration to ensure the system reaches a stable plateau. During these steps, we alternated between switching the light on and off. This methodology enables us to study the specific effects of light on catalytic activity under stable and controlled temperature conditions.

These two distinct experimental procedures were employed to comprehensively investigate the influence of temperature and light on the catalytic activity and gain insights into the underlying mechanisms involved in the thermo-photo catalytic reactions.

4.3.1 Light-off experiment evaluation

A light-off experiment is a common technique used in catalysis research to study the catalytic activity of a material, typically a catalyst, in the context of a chemical reaction, such as the oxidation or reduction of a specific reactant. This experiment is called a "light-off" experiment because it involves monitoring the catalytic activity as a function of temperature while the catalyst is exposed to a reactant, and the reaction is initiated by heating the catalyst with a source of heat.

Light-off experiments are valuable in catalysis research because they provide insights into the temperature range at which a catalyst is most active and can help optimize reaction conditions for industrial processes. Additionally, they can be used to compare the catalytic performance of different materials or catalyst formulations.

In our application, a preliminary test was carried out using a 4%w/w Rh/CeO_2 BM catalyst in dark conditions to verify the reproducibility of the light-off curve in sequential tests. In fact, an evaluation of the effect of light on the catalyst activity based on the comparison of light-off curves taken sequentially in dark and light conditions requires high stability of the samples in repeated light-off tests.

The experimental procedure involved loading 50 mg of the catalyst into the reactor. Afterward, the reactor was flushed with 25 ml/min of inert gas. Following a 30-minute period, the temperature in the reaction chamber was raised from ambient to 100°C. Subsequently, a gas mixture of 35 ml/min, comprising 61% H_2, 11% CO_2, and 28% He, was introduced into the reactor.

Once the Mass Spectrometry (MS) baseline became stable, indicating a steady-state condition, the experiment proceeded. A temperature ramp of 15°C/min was initiated to reach a maximum temperature of 400°C, which was maintained for 30 minutes. The reactor was then cooled down to 100°C using a flow of helium gas.

After the first temperature ramp and cooling, the experiment was repeated. Following this, an oxidation treatment was carried out at 450°C for 2 hours using a gas mixture of 30 ml/min containing 10% O_2 and 90% Ar. Finally, the light-off ramp experiment was repeated under the same conditions. The overall results of these experiments are reported in the figure below.

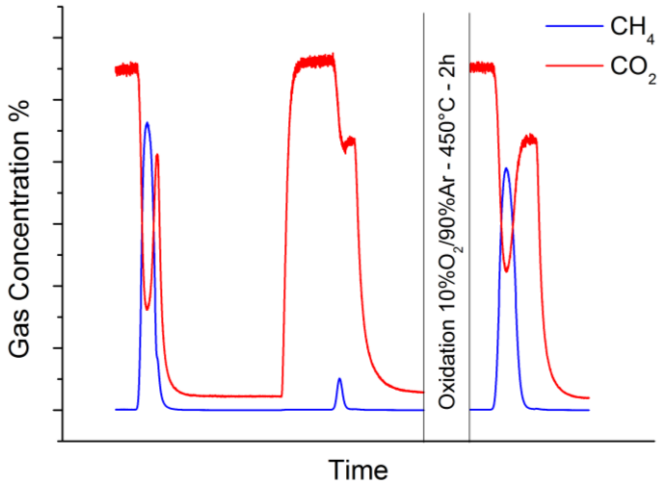

Fig. 4.3 CH_4 and CO_2 concentration in the exhausts, showing three consecutive experiments in temperature ramp 15°C/min, 100-400°C, 61%H_2/11%CO_2/28%He 35ml/min, followed m/e=16 for CH_4 and, m/e=44 for CO_2, see paragraph 3.2.3 for more details.

The first obvious observation about the figure above is the de-activation of the catalyst at the end of the first cycle. A dramatic decrease of CH_4 production such that depicted, in the same experimental conditions, clearly indicates some sort of modification of the active surface during the experiment. Furthermore, an oxidation treatment could not restore completely the initial catalyst conditions leading to the conclusion that these modifications are permanent.

Many reasons may lead to the observed phenomena: Metal active sites deactivation depending on particles size and sintering phenomena. Additionally, the nature of the support and the strength and character of the metal-support interaction play significant roles, in particular rhodium (Rh) is well known to exhibit strong metal-support interactions (SMSI) with reducible supports such as TiO_2 and CeO_2 [215]. These interactions, especially in structure-sensitive supports, can evolve depending on the thermal treatment and the exposure atmosphere, often leading to negative—and sometimes irreversible—effects on catalytic activity.

Also, it could not be excluded the formation of carbidic (C_α) and graphitic(C_β) carbon, which are two distinct forms of carbon that can deposit on the surface of catalysts during various chemical reactions involving Carbon sources as CO_2. It is reported that when CO_2 adsorbs onto a metal catalyst surface like Rhodium, it can dissociate into carbon (C) and oxygen (O) atoms. The carbon atoms can then bind strongly to the metal surface, forming C_α carbon. [214, 215]. This increased stability is due to the strong chemical bonds formed between carbon and the metal surface. In catalysis, carbidic carbon can either be an active intermediate species or a catalyst poison, depending on the specific reaction. It can participate in further surface reactions, including hydrogenation or methanation reactions. However, its accumulation in organized crystallites of graphitic carbon can also block active sites and reduce catalyst activity over time. C_β to be a catalyst deactivator rather than an active participant in reactions. It covers active sites on the catalyst surface, hindering reactant access and reducing catalytic activity [216, 217]. From a thermodynamic perspective,

during methanation, the formation of carbidic carbon is favoured due to its stronger interaction with the catalyst surface [119].

Moreover, the absorption of the carbon species onto the surface of Rhodium catalyst may led to an irreversible modification of the surface and such a modification is also linked with the temperature and the experimental conditions. [218, 219]

Taking these results into account, and since the main purpose of our work was to compare the performance of the catalysts simultaneously with the study of plasmonic phenomena, we decided to abandon the light-off experiments and adopt an approach that could ensure a longer longevity of the catalysts to compare their performance under dark and light conditions. An isothermal steps-test at different temperature up to 350°C resulted more suitable for a direct evaluation of light effect on the catalysts activity and for mitigating the risk of undesired deactivation phenomena.

4.3.2 Isothermal steps experiment evaluation

A typical isothermal-step experiment we report the structure was carried out following the scheme in Fig. 4.4:

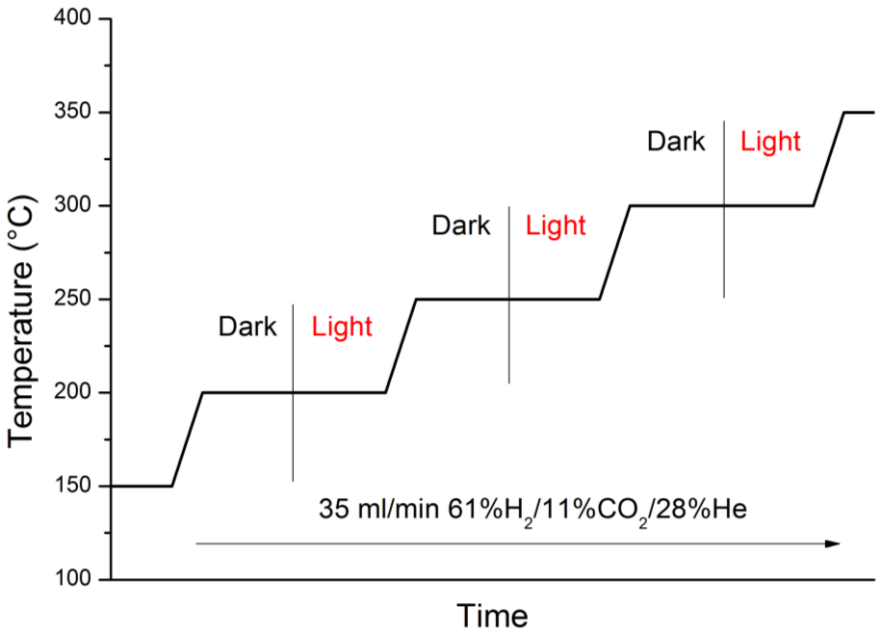

Fig. 4.4: Typical layout of an Isothermal steps experiment

The experiment was conducted using a catalyst that had been prepared following the experimental conditions previously described. The data collection process commenced after a stable baseline reading was achieved at a temperature of 150°C. In each experimental step, a carefully defined increment in product concentration was measured, eventually almost immediately reaching a stable outcome. For each step in the experiment, the temperature was held constant for a specific duration, in this case, 60 minutes. The

procedure followed a sequence wherein the temperature was initially maintained in the dark (without light) for the first 30 minutes, after which the light source was activated for the subsequent 30 minutes, and finally, the light was switched off just before the temperature was ramped up to the next step. The product (and converted reactants) quantities in kmol obtained by integrating in 30 minutes time the concentration values in both dark and light conditions were used to calculate conversion, selectivity and yield values by mean of Eq. 4.4, 4.5 and 4.6 respectively. The resulting experimental data is plotted in the figure below, illustrating the trends and outcomes observed throughout the experiment.

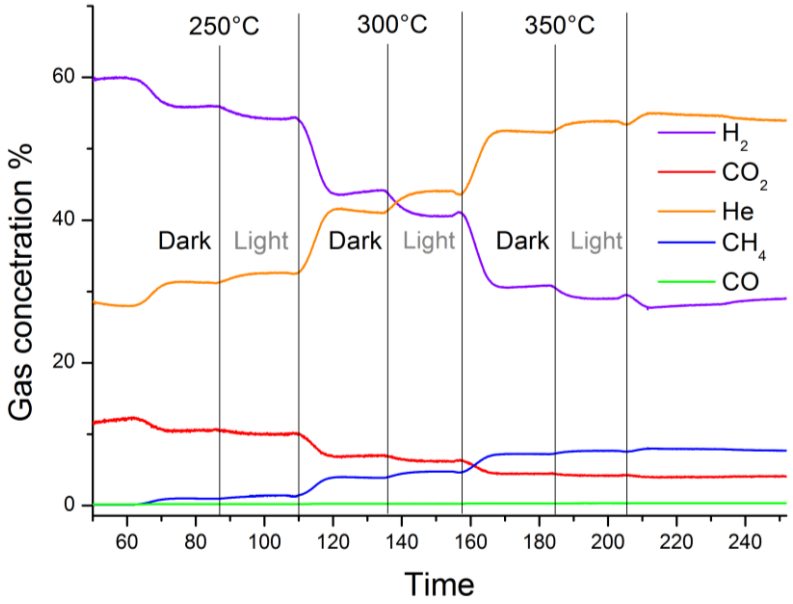

Fig. 4.5: Gas mix concentration plot Vs Time; Typical experimental design

Lastly, it is essential to introduce the graph used to succinctly compare the catalytic performance of the catalyst material in the formation of CH_4 and the conversion of CO_2.

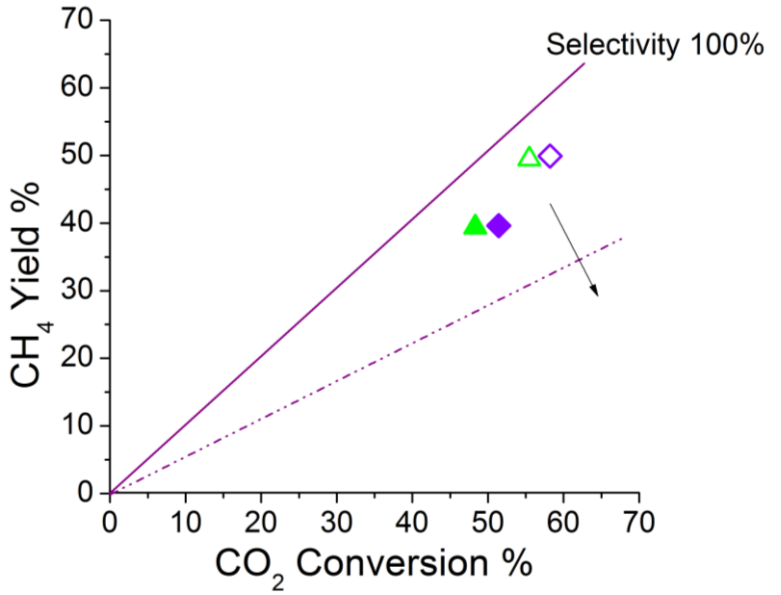

Fig. 4.6: CH_4 Yield% Vs CO_2 Conversion% graph type example, full and empty symbols represent dark and light conditions respectively.

In the figure presented above, we have % Yield to CH_4 on the ordinate axis plotted against % Conversion of CO_2 on the abscissa axis, collected in the same reaction conditions of temperature and flowing gas composition. Noticeably, both axes share the same scale. Additionally, Yield and Conversion are interconnected through equation (4.6). Consequently, the bisector of the plane corresponds to 100% Selectivity to CH_4, ensuring that no data points will ever be positioned above it.

This graphical representation serves multiple purposes:

1. It allows us to assess the catalyst's ability to activate the CO_2 molecule.
2. It facilitates a quantitative comparison of how much final product (CH_4) is generated.
3. It provides insights into the catalyst's efficiency in converting carbon dioxide to our desired product.

Furthermore, distinct symbols are utilized to represent specific materials, as detailed in the legend. Each symbol can either be solid or empty, indicating whether the experiment was conducted in Dark or Light conditions, respectively.

Through this graphical approach, we achieve a comprehensive and visual assessment of the catalytic performance of different materials, offering valuable insights into their behaviour.

4.3.3 Light contribution evaluation

The spectrum of a Xenon solar light simulator includes a significant portion of Near-Infrared (NIR) and Infrared (IR) irradiation. This characteristic introduces the possibility of overlapping effects between different phenomena:

1. **Plasmonic Non-Radiative Relaxation**: This pertains to the dissipation of energy by hot carriers generated during the Localized Surface Plasmon Resonance (LSPR) excitation of nanoparticles, leading to a photothermal effect.
2. **Non-Plasmonic Radiative Re-emission**: This involves the re-emission of heat absorbed as photons in the IR region, similar to the behaviour of dark bodies, into the surrounding medium.

To better distinguish and understand the contributions of these different phenomena to the increase in temperature as measured by the thermocouple T_{sample}, preliminary experiments were conducted. Firstly, as a fundamental reference, the temperature of the alumina felt, which serves as the support for the catalyst powder in the experimental setup, was measured under the light beam. This measurement was carried out at various increasing temperature steps while maintaining an inert gas flowing atmosphere. Then the reference temperature profile obtained from the alumina felt was then compared with the temperature

measured within the catalyst bed (4%wtRhBM/$Ce_{0.8}Ti_{0.2}O_2$), also in an inert gas flow condition. The resulting data and plots from these experiments are presented in the following figure.

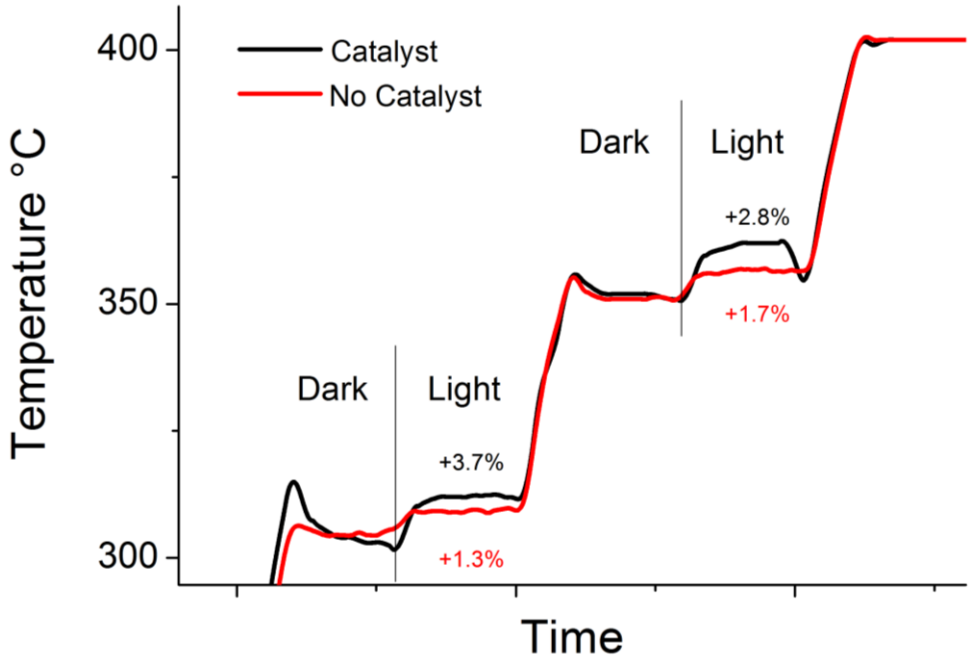

Fig. 4.7: Temperature profile measured by T_{sample} thermocouple on the alumina bed in presence or absence of catalyst, respectively black and red lines, in inert atmosphere

As evident from the data and observations, the percentage increase in temperature between the dark and light experimental conditions is notably higher in the presence of the catalyst. This outcome aligns with expectations and serves as a clear indication that the temperature increase observed in the catalyst is unrelated to the IR portion of the light spectra. This distinction is significant because it implies that the catalyst's temperature rise is primarily driven by other factors, such as the plasmonic non-radiative relaxation of hot carriers associated with LSPR excitation, rather than by the IR radiation.

To further investigate and confirm the behaviour of the photo-activated catalyst during the reaction, a valuable approach is to utilize optical filters. These filters can selectively cut off specific parts of the light spectra, allowing for controlled experimentation and data collection. Here are the optical filters mentioned along with their purposes:

1. **Air Mass 1.5-Global**: This filter replicates the solar spectrum experienced on Earth's surface, providing a baseline reference for comparison.

2. **Heat Reflecting NIR-IR Filter (800-1100 nm Cut-off)**: This filter blocks light in the Near-Infrared (NIR) and Infrared (IR) range, helping to assess the contribution of these wavelengths to the catalyst's behaviour.

3. **Colored Glass Filter (GG395 Long Pass Type, UVA/UVB Blocking)**: This filter allows longer wavelengths to pass through while blocking UVA and UVB, aiding in evaluating the impact of visible light on the catalyst.

4. **UVC Blocking Filter (280-440 nm)**: This filter blocks UVC wavelengths, allowing for an examination of the catalyst's response to shorter-wavelength UV light.

By employing these optical filters, it is possible to control the spectrum of light reaching the catalyst and collect data on its activity. Quantifying the catalyst's activity in terms of CH_4 production yield and correlating it with the specific portion of the absorbed light and its Intensity will provide precious inside on the plasmonic effect and its contribution to the overall performance.

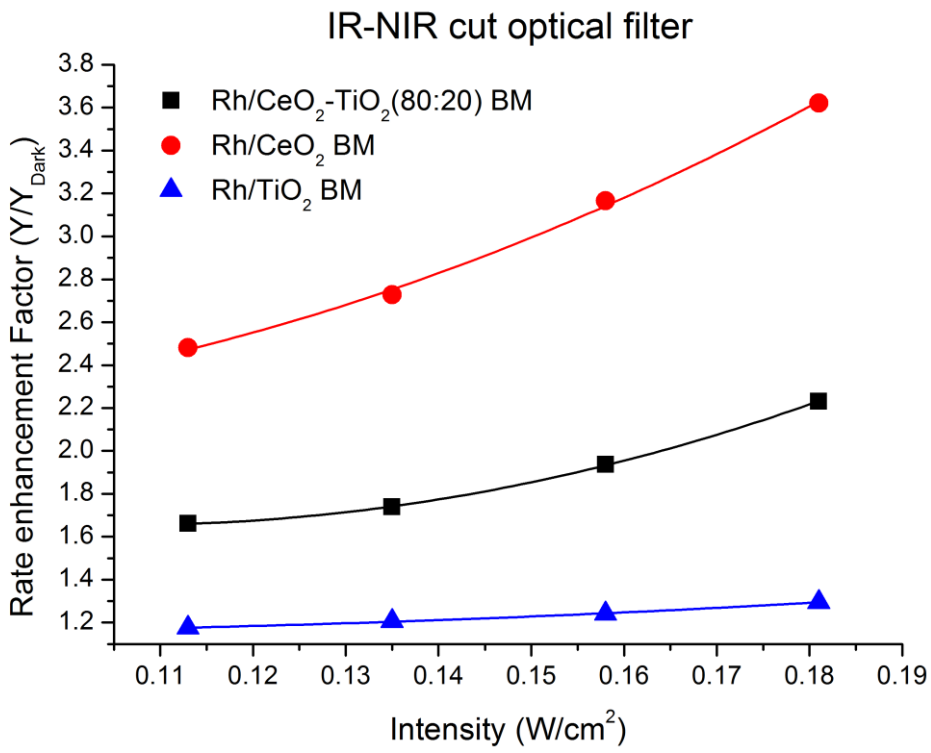

Fig. 4.8 Rate enhancement Factor due to light contribution as a function of increasing light Intensity for different catalysts – Tchamber =250°C, 61% H_2/11% CO_2/28% He, ϕ=35ml/min

In the figure above (fig. 4.8) we can observe how the increasing Intensity of light leads to an increase of the Rate enhancement factor defined as:

$$R(I) = \frac{Y\%(I)}{Y_{Dark}\%(I_0)} \quad ; \quad I_0 = 0 \qquad (Eq. 4.7)$$

Here, Y% represents the yield to CH_4 calculated in both Dark (I_0) and Light conditions for increasing light intensity (I) measured with the optometer. To ensure that any thermal contributions from thermal photons

are excluded and to highlight any potential photothermal effects due to the plasmonic metal, the light spectrum was filtered to remove the IR-NIR portion of the spectrum.

R factor is crucial for discussing the plasmonic properties of the catalyst and the enhancement of performance due to the use of light. The rate reported in Fig. 4.8 corresponds to the rate defined in the following equation:

$$R_{photo}(I) = R_{therm}(I) + R_{Hot-e}(I) \qquad (Eq. 4.8)$$

This means that the overall increase is a combination of a thermal photo-induced plasmonic effect and a hot-electron injection plasmonic effect. This combination of effects impacts the type of profile observed. Specifically, an exponential increase profile suggests a prevalent photothermal contribution, while a linear law is typical of a hot-electron injection contribution [222].

Furthermore, as previously mentioned, there are several approaches to distinguish between the photothermal and hot-electron injection contributions to the enhancement rate. In this study, one such approach is used, expressed as follows:

$$R_{Hot-e}(I) = R_{photo}(I) - R_{therm}(I) \qquad Eq. (4.9)$$

Where R_{therm} is attributed to the photo-induced heating of the sample, and the j^{th} contribution can be determined by measuring the temperature T_{sample} when the sample is illuminated with light intensity I_j Subsequently, $Y_{photo-therm}\%$ is experimentally measured in the dark at $T_{chamber} = T_{sample}(I_j)$, and consequently, $R_{therm}(I)$ is calculated as follows:

$$R_{therm}(I_j) = \frac{Y_{therm}\%(I_j)}{Y_{Dark}\%(I_0)} \qquad Eq. (4.10)$$

In the figure below are reported Photothermal and Hot-Electron Injection contribution calculated as discussed, which added together are equivalent, for each sample, to the total contribution represented in fig. 4.8:

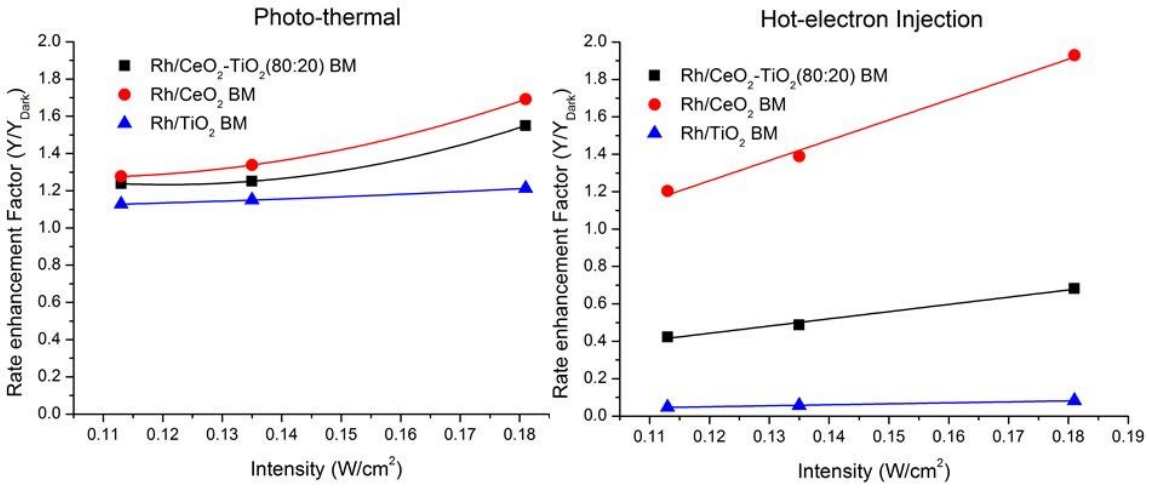

Fig. 4.9 Rate enhancement Factor due to Photothermal and Hot-electron Injection contribution as a function of increasing light Intensity for different catalysts – Tchamber =250°C, 61% H_2/11% CO_2/28% He, ϕ=35ml/min

The plots reported in fig. 4.9 show the decreasing hot-electron injection contribution with the content of Ceria, in fact while in case of Rh/CeO_2 sample it contributes of about 50%, in the case of pure Titania supported sample we can attribute to this effect just around 5% of contribution.

About the Photothermal effect we can observe a quite comparable contribution for all the sample examined with a slight increasing trend for ceria containing samples.

4.3.4 Metal loading impact

Before producing the catalyst samples for use in the experimental campaign, a preliminary study was conducted to assess the impact of metal loading on catalyst performance. To achieve this, three different Rhodium loadings were considered, each with a varying weight percentage (2,4,8 wt%) of elemental rhodium on a $Ce_xTi_{1-x}O_2$ (x=0.8) mixed oxide support. These catalyst materials were subsequently subjected to testing using an Isothermal Step Experiment approach.

The resulting data were collected under consistent reaction conditions, specifically:

- **$T_{chamber}$**: Maintained at 250°C.
- **Gas Composition**: The reaction mixture consisted of 61% H_2, 11% CO_2, and 28% He.
- **Flow Rate (φ)**: Set at 35 ml/min.
- **Experimental Conditions**: The experiments were conducted both in dark and light conditions.

The key performance metrics evaluated based on the collected data were:

- **CO_2 Conversion (X%)**: The percentage of CO_2 that was converted during the reaction.
- **CH_4 Yield (Y%)**: The percentage of methane (CH_4) produced as a product of the reaction.

By comparing the data obtained from these experiments (Fig 4.10) at different catalyst loadings, the study aimed to gain insights into how the metal loading influences the catalytic performance under these specific conditions, with and without light exposure.

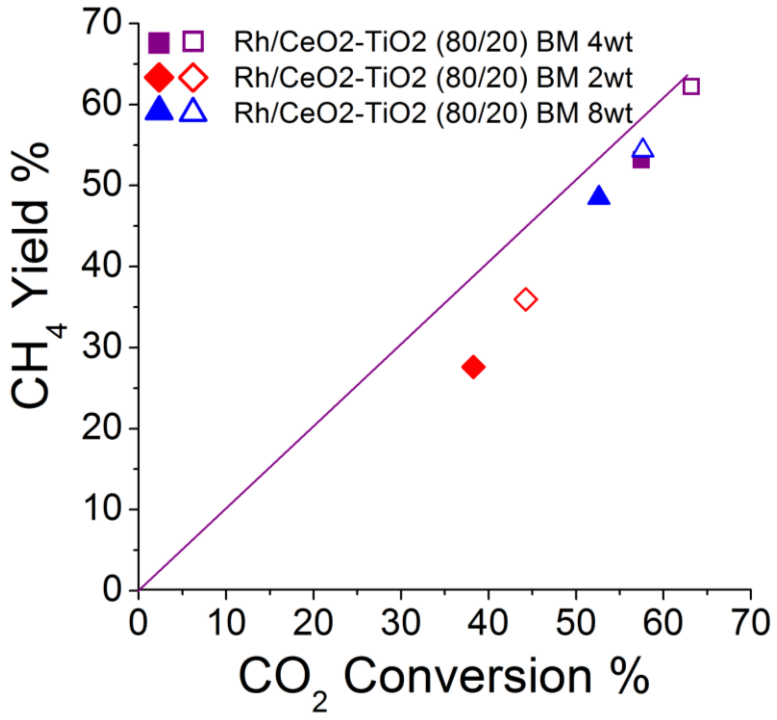

Fig. 4.10 CO_2 conversion % Vs CH_4 yield % compared at the same reaction conditions: Tchamber =250°C, 61% H_2/11% CO_2/28% He, ϕ=35ml/min in Dark/Light condition (full and empty symbols respectively)

From our observations, it becomes evident that the loading of 4%wt of Rhodium performs the best among the considered loadings. To gain a more comprehensive understanding of the results, we need to distinguish between catalytic activity, including conversion and yield, and the relative improvements between light and dark conditions.

- **Catalytic Activity:** When evaluating catalytic activity, the best performance is indicated by data points that are closer to the top-right corner of the performance graph. In this context, it's clear that the 4%wt metal loading exhibits the highest catalytic activity.
- **Relative Improvement Between Dark and Light Conditions:** When assessing the relative improvement between dark and light conditions, we observe an interesting trend: 2% > 4% > 8%. This variation can be attributed to differences in nanoparticle size and distribution within the catalyst.

Specifically, the higher the metal loading, the more likely it is that larger clusters will form. This larger particle size may lead to a reduction in the contribution of the plasmonic photothermal effect to the overall reaction efficiency. In other words, the 2%wt metal loading outperforms the others in terms of the relative enhancement of catalytic activity under light conditions compared to dark conditions. This suggests that the

nanoparticle size and distribution play a crucial role in the plasmonic photothermal effect's impact on the catalytic reaction, nonetheless the overall catalyst activity is influenced mostly by the metal quantity and a good compromise needs to be found.

4.4 FT-IR DRIFT

4.4.1 Experimental Equipment

For this experience a Nicolet Si50 FTIR Spectrometer was equipped with a Pike Technologies DiffusIR research grade diffuse reflection accessory and *in-operando* measure reaction chamber.

To address the issue of having a UV-Vis independent light source for the FT-IR-DRIFT experiments described earlier, a modification was implemented using the solar simulator that had been employed in our experimental campaign. A custom-made metallic structure was constructed to suspend the light source above the spectrometer. This setup allowed for the irradiation of the sample during the experiments with a 24mm solar light beam, which had been filtered to exclude the IR-NIR and UV portions of the light spectra using the optical filters previously described.

The elimination of the IR-NIR segment was done to prevent interference with the measurements, while the removal of UV was aimed at avoiding any potential interaction with the KBr window of the reactor. Additionally, the light beam was carefully focused to exclusively irradiate the sample, minimizing reflections that might otherwise interfere with the IR optical path. The light intensity was measured by mean of a digital optometer and resulted to be around 0.081 W/cm^2.

4.4.2 FT-IR DRIFT investigation

Fourier Transform Infrared Diffuse Reflectance Spectroscopy, commonly known as FT-IR DRIFT spectroscopy, is a specialized method used to analyse the composition and molecular structure of solid samples. It is a

variant of conventional infrared spectroscopy and is particularly well-suited for examining powdered or granular materials and surfaces that may be rough or irregular.

In FT-IR spectroscopy, the interaction of matter with infrared radiation is studied, focusing on the vibration of chemical bonds within molecules. This vibration is indicative of a substance's molecular structure and serves as a basis for identification and quantification. The main vibrational modes due to IR absorption are reported below:

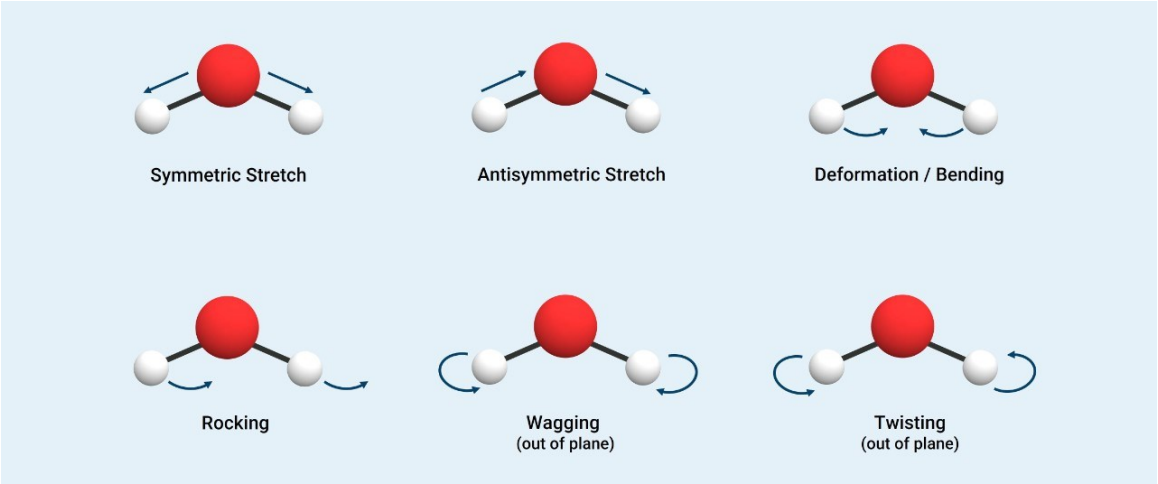

Fig. 4.11 Graphical representation of typical vibration modes of molecules as a consequence of IR absorption

Molecules can vibrate in a variety of ways, and these vibrations are observed as peaks in the infrared spectrum. There are six primary vibrational modes that can be observed in FT-IR spectroscopy:

Stretching Modes:

Symmetric Stretch (v_1): Atoms within a molecule move toward or away from each other in unison. This leads to a strong peak in the infrared spectrum.

Asymmetric Stretch (v_3): Atoms within a molecule move in opposite directions. This also results in a distinct peak.

Bending Modes:

In-Plane Bending (v_2): Atoms within a molecule bend within the same plane. This mode is typically weaker than stretching modes.

Out-of-Plane Bending (v_4): Atoms within a molecule bend out of the plane defined by the other atoms. This is often a weak absorption.

Rocking and Wagging Modes:

Rocking (v_6): Atoms oscillate back and forth with respect to a central atom.

Wagging (v_7): Atoms oscillate side to side. Both rocking and wagging are often weak absorptions.

Torsional Modes:

Twisting (v_5): Atoms rotate around single bonds, and this can result in weak to no absorption in the IR spectrum.

The precise frequency and intensity of these vibrational modes depend on the masses of the atoms involved, the strength of the chemical bonds, and the molecular structure. By analysing the IR spectrum, chemists can identify functional groups, determine the type of bonds in a molecule, and gain insights into molecular structure and interactions.

What sets FT-IR DRIFT spectroscopy apart is its utilization of diffuse reflectance. Instead of transmitting or directly contacting the sample, this method scatters incident infrared light off the sample's surface. The reflected light is then collected and subjected to Fourier transformation for analysis. To prepare a sample for analysis, it is typically transformed into a powder or granular form, ensuring uniformity, and simplifying the preparation process. This sample is evenly spread on a sample holder with a reflective surface.

As with traditional FT-IR, a Fourier Transform spectrometer is employed in DRIFT spectroscopy. The collected scattered light is interfered with a reference beam, resulting in an interferogram. This interferogram is then Fourier-transformed into an infrared spectrum, which displays the intensity of absorbed radiation at various wavelengths.

Interpreting the spectrum reveals peaks and troughs at specific wavelengths, each corresponding to molecular vibrations within the sample. These peaks provide information about the chemical bonds and functional groups present, and they can be used for both qualitative and quantitative analysis.

The in-operando FT-IR DRIFT technique is a powerful tool for gaining a better understanding of the mechanism involved in CO_2 reduction reactions. It provides valuable insights into the interaction between reactants and the active surface of the catalyst during the reaction itself. Furthermore, careful experimental planning allows researchers to deduce more information about the overall reaction conditions by isolating the individual contributions of reactants. This approach can reveal the species that emerge or disappear when reactants are introduced or removed from the reaction chamber.

Light source interference check

The introduction of an independent light source necessitated certain checks to ensure the accuracy of the measurements and prevent any distortion of the recorded signals. Typically, during the initial calibration

procedure, the instrument requires a background spectrum to be collected using a mirror insert. As a first step in verifying the new setup, a spectrum was collected with the external light source shining on the mirror. Upon comparing this spectrum with the one collected without external light, it was observed that they almost perfectly matched. This confirmation indicated that the use of an external light source was compatible with the FT-IR DRIFT experimental setup.

5 Material Characterization

The catalysts studied were characterized using various techniques such as X-Ray Diffraction (XRD), N_2 physisorption (Brunauer-Emmett-Teller method, BET and Barrett-Joyner-Halenda, BJH method as porosimetry characterization), H_2-TPR, DRS and TEM. For the reader's convenience, Table 5.1 lists the synthesized supports and catalysts with their nickname and the analysis performed on them.

Table 5. 1 Catalysts characterizations resuming table.

Catalysts	Characterization Techniques				
	XRD	BET-Poros.	H_2-TPR	DRS	TEM
CeO_2	x	x	x	x	x
Rh-CeO_2-BM	x	x	x	x	x
Rh-CeO_2-IW	x	x			x
$Ce_{0.8}Ti_{0.2}O_2$	x	x	x	x	x
Rh-$Ce_{0.8}Ti_{0.2}O_2$-BM	x	x	x	x	x
Rh-$Ce_{0.8}Ti_{0.2}O_2$-IW	x	x		x	x
$Ce_{0.5}Ti_{0.5}O_2$	x	x	x	x	
Rh-$Ce_{0.5}Ti_{0.5}O_2$-BM	x	x	x	x	
Rh-$Ce_{0.5}Ti_{0.5}O_2$-IW	x	x			
$Ce_{0.2}Ti_{0.8}O_2$	x	x	x	x	
Rh-$Ce_{0.2}Ti_{0.8}O_2$-BM	x	x	x	x	
TiO_2	x	x	x	x	x
Rh-TiO_2-BM	x	x	x	x	x
Rh-TiO_2-IW	x	x			x

The analyses were performed initially on bare oxide supports, with the aim of fully characterize the impact of solid solution's composition on the structure and morphology of the samples. Then we could compare,

were necessary, functionalization methods with respect to the support material and the functionalization methods between them for specific samples, with the aim of underline peculiar differences and tract punctual conclusion through observation about the metal reducibility, the support reducibility, defects and oxygen vacancies, as well as the optical properties useful to show the typical behaviour of catalysts owing plasmonic resonance response to light and put it in correlation with the other analytic techniques.

5.1 Support characterizations

BET-Porosimetry and XRD analysis

In Fig. 5.1 and 5.2 are reported the results of Porosimetry analysis

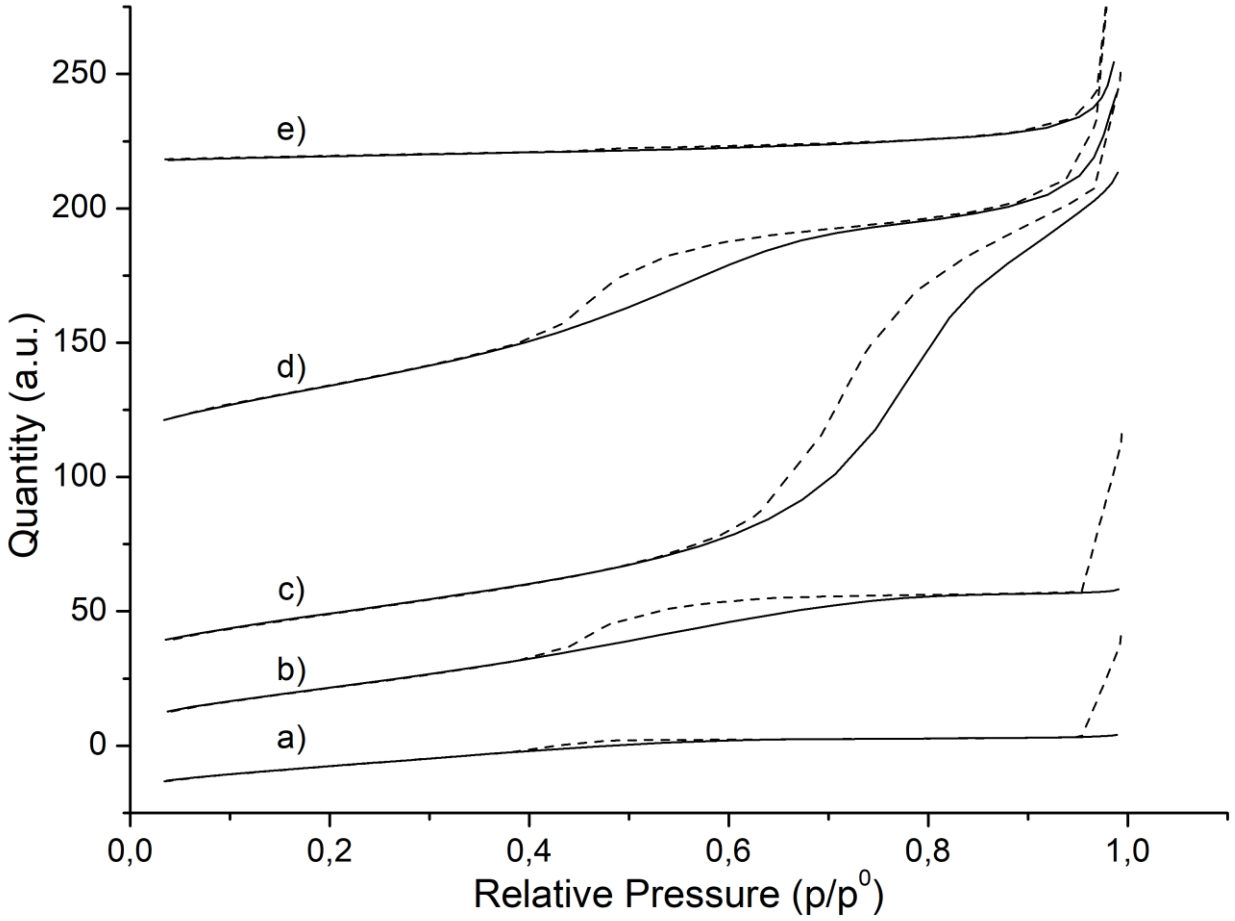

Fig. 5. 1 N_2 - Adsorption and Desorption (solid and dashed lines respectively) Isotherms for all support materials, pure oxides and compositions of mixed oxides. a) CeO_2 , b)$Ce_{0.8}Ti_{0.2}O_2$, c) $Ce_{0.5}Ti_{0.5}O_2$, d) $Ce_{0.2}Ti_{0.8}O_2$, e) TiO_2.

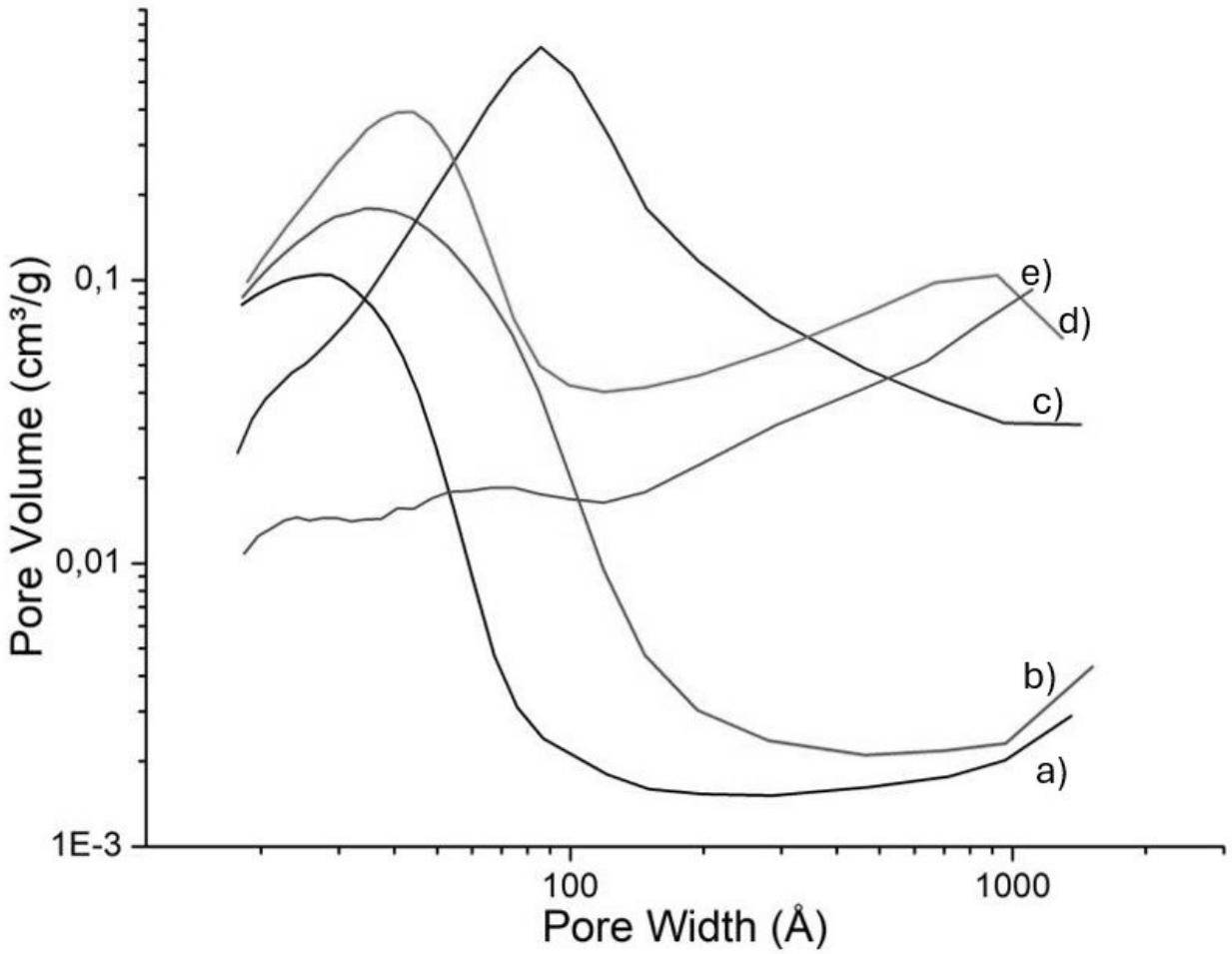

Fig. 5. 2 Pore Volumes as a function of the pore width, distribution of the pores size. a) Rh/CeO_2, b) $Rh/Ce_{0.8}Ti_{0.2}O_2$, c) $Rh/Ce_{0.5}Ti_{0.5}O_2$, d) $Rh/Ce_{0.2}Ti_{0.8}O_2$, e) Rh/TiO_2

In the comparative figure 5.3 are reported XRD diffractograms of the supports prepared as reported above:

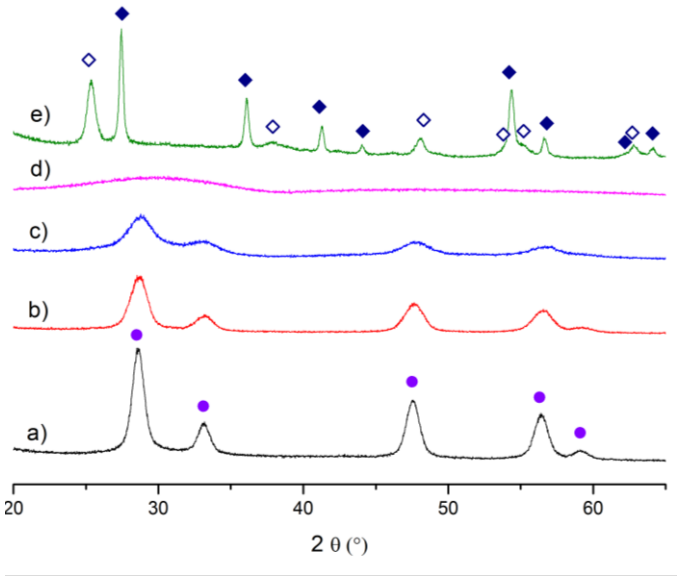

Fig. 5. 3 XRD spectra of a) pure Ceria, b) $Ce_{0.8}Ti_{0.2}O_2$, c) $Ce_{0.5}Ti_{0.5}O_2$, d) $Ce_{0.2}Ti_{0.8}O_2$, e) pure Titania; with blue solid and empty diamonds are reported the diffraction peaks of Rutile and Anatase Titania phases respectively, with violet circles are reported the diffraction peaks of Ceria cubic fluorite structure

The alteration in crystallite structure with varying Titania content is evident. Initially, a characteristic cubic fluorite structure is observed for Ceria, and this persists up to a 50:50 Ceria-Titania ratio. However, the 20:80 ratio displays indistinct peaks, resembling a relatively amorphous structure. Additionally, the Titania sample exhibits both Anatase and Rutile phases, each characterized by their di-tetragonal or di-pyramidal structure with coordination numbers Z=4 and 2, respectively [223].

Table 5. 2 Crystalline Structure, Lattice Parameter, and Crystallite Size of TiO_2-CeO_2 Mixed Oxides.

	Crystallite Structure	Lattice Parameter (nm)		Mean Crystallite size (nm)	S_{BET} [m^2/g]	Vol_{pore} [cm^3/g]	D_{pore_size} (nm)
		a	c				
CeO_2	*Fluorite*	0.5424	-	8.3	63	0.042	2.9
$Ce_{0.8}Ti_{0.2}O_2$	*Fluorite*	0.5418	-	5.6	103	0.095	3.5
$Ce_{0.5}Ti_{0.5}O_2$	*Fluorite*	0.5373	-	3.7	122	0.308	8
$Ce_{0.2}Ti_{0.8}O_2$	*N/D*	-	-	-	160	0.238	5
TiO_2	*Anatase*	0.3785	0.9332	20.7	10	0.049	17
	Rutile	0.4596	0.2959	18.5			

The analysis of cerium and titanium oxide samples reveals important correlations between crystallite size, lattice parameters, and surface properties, as outlined in Table 5.2. The average crystallite size, calculated using the Scherrer equation, is consistently below 10 nm, classifying the materials as nanostructured or

nanomaterial. This finding aligns with typical characteristics of nanostructured cerium oxides, where the lattice parameter “a“ tends to increase compared to the bulk cerium value of 0.5403 nm, as shown in previous studies [224, 225]. The observed increase in the lattice parameter for cerium nanoparticles is attributed to different lattice packing [224]. In fact, the modification of lattice parameters in cerium-based oxides is influenced by the introduction of dopants, such as titanium, which induce distortions in the crystal structure, further contributing to the changes in lattice constants and the reducibility of the material [226].

The incorporation of titanium into the cerium oxide lattice results in a contraction of the lattice parameter, as seen in the CeO_2-TiO_2 solid solutions. This contraction is driven by the substitution of the larger Ce^{4+} ion (0.97 Å) with the smaller Ti^{4+} ion (0.61 Å), leading to a compression of the crystal lattice [225]. The structural distortion caused by the presence of titanium significantly alters the material’s properties, particularly in terms of reducibility and oxygen vacancy formation, as Watanabe et al. (2009) observed [226]. The introduction of Ti into cerium oxide is not only responsible for the contraction of the lattice but also for the appearance of structural defects that affect the overall crystallographic stability and catalytic behaviour.

The inclusion of titanium also affects the surface properties of the mixed oxides. Ce:Ti(50:50), for example, exhibits a specific surface area of 122 m^2/g, a pore volume of 0.308 cm^3/g, and an average pore size of 8 nm, which significantly differs from pure CeO_2 and TiO_2. This increased surface area and pore volume suggest a more complex and developed mesoporous structure, which is also reflected in the adsorption-desorption curves from the BET analysis (see Figure 5.1). The pronounced hysteresis observed for Ce:Ti(50:50), especially at higher relative pressures, indicates the presence of bottle-necked pores or other structural features that create significant resistance during desorption. This behaviour suggests that Ce:Ti(50:50) has a more heterogeneous porosity, with a combination of large pores and narrower constrictions, leading to greater adsorption capacity but also a more difficult release of adsorbed gases during the desorption phase.

The behaviour of Ce:Ti(80:20) and Ce:Ti(20:80) also reflects their mesoporous nature, with both samples showing comparable hysteresis (see Figure 5.1). The specific surface area of 103 m^2/g for Ce:Ti(80:20) and 160 m^2/g for Ce:Ti (20:80), combined with their respective pore volumes of 0.095 cm^3/g and 0.238 cm^3/g, suggest a well-developed porous network in both cases, as supported by the pore size distribution (see Figure 5.2). The slight difference in hysteresis between these two samples can be attributed to the greater volume of pores and larger pore size (5 nm) in Ce:Ti(20:80), which allows for a higher adsorption capacity but also introduces a moderate resistance to desorption. This resistance, although not as pronounced as in Ce:Ti(50:50), reflects the complexity of the pore structure, where narrower necks or constrictions may still be present, albeit less frequent. The higher surface area of Ce:Ti(20:80) provides more active sites for catalytic reactions, making this composition particularly interesting for catalytic applications where a balance between adsorption and desorption kinetics is crucial.

In comparison, the CeO_2 sample, with a specific surface area of 63 m^2/g, exhibits a much smaller hysteresis. This suggests that, although CeO_2 has smaller pores (average size 2.9 nm), its overall porous structure is less complex than that of the mixed oxides, resulting in lower resistance during the desorption process. The relatively small hysteresis indicates that CeO_2 has a simpler mesoporous structure, where most of the pores are open and well-connected, facilitating easy desorption. Despite this, the fine mesoporosity and the moderate surface area of CeO_2 contribute to good adsorption properties, making it a viable support for catalytic applications [224].

TiO_2 sample, on the other hand, exhibits almost no hysteresis (see Figure 5.1), reflecting its low surface area (10 m^2/g) and larger pore size (17 nm). The lack of hysteresis suggests that TiO_2 has a more open and uniform pore structure, without significant constrictions or narrow necks, allowing for easy desorption. This makes TiO_2 particularly well-suited for applications requiring rapid desorption of adsorbed molecules, such as photocatalysis, where open and well-connected pores can facilitate the interaction with reactive species on the surface.

Overall, the BET and pore size distribution data highlight how the introduction of titanium into cerium oxide leads to a more developed mesoporosity and a significant increase in surface area, especially in samples like Ce:Ti(20:80) and Ce:Ti(50:50). The combination of smaller crystallite sizes, lattice parameter modifications, and enhanced porosity indicates that these materials, particularly Ce:Ti(50:50), are likely to exhibit improved catalytic performance due to the greater availability of active sites and the increased surface interaction with reagent molecules. As observed in the study by Gionco et al. (2013), the formation of mixed oxide phases between CeO_2 and TiO_2 not only increases the surface area but also enhances the reducibility and alters the optical properties of the material, making these mixed oxides especially suitable for catalytic applications where both high surface area and structural complexity are critical [224].

In conclusion, the integration of crystallographic data with BET and pore size distribution analysis underscores the importance of structural and surface property modifications in cerium-titanium oxide systems. The observed trends in surface area, porosity, and hysteresis (as seen in Figures 5.1 and 5.2) demonstrate that titanium incorporation leads to a significant improvement in porosity, while the structural distortions induced by Ti result in reduced crystallite sizes (also confirmed by TEM images reported below) and modified lattice parameters. These features, in combination, provide a strong basis for enhancing the catalytic efficiency of these materials, particularly in applications where small particle size, high porosity, and complex mesoporous structures are essential for improving reaction kinetics and overall performance [225, 226].

Transmission Electron Microscopy Analyses

TEM analysis averagely confirmed XRD calculated Crystallite size

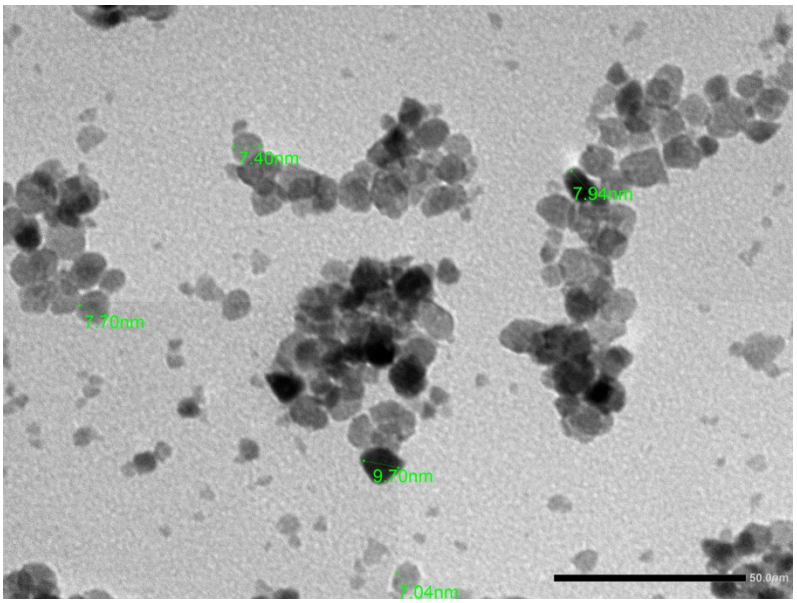

Fig. 5. 4 Synthetized CeO_2 TEM image reporting measures of the crystallites

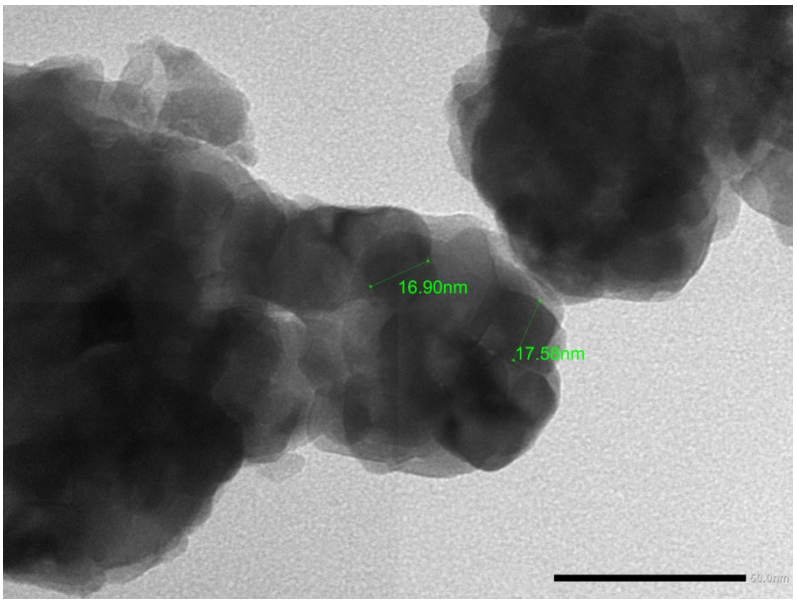

Fig. 5. 5 Synthetized TiO_2 TEM image reporting measures of the crystallites

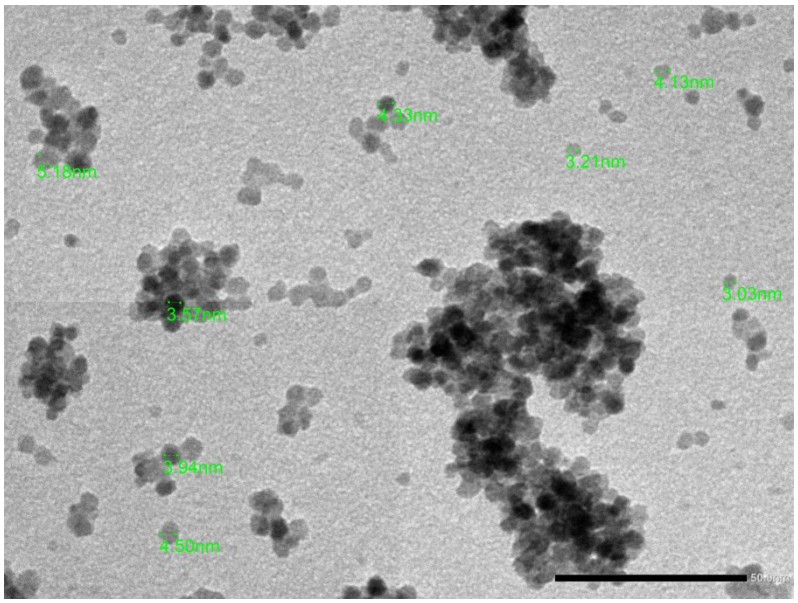

Fig. 5. 6 Synthetized CeO_2-TiO_2 (80:20) TEM image reporting measures of the crystallites

H_2 - Temperature Programmed-Reduction characterization

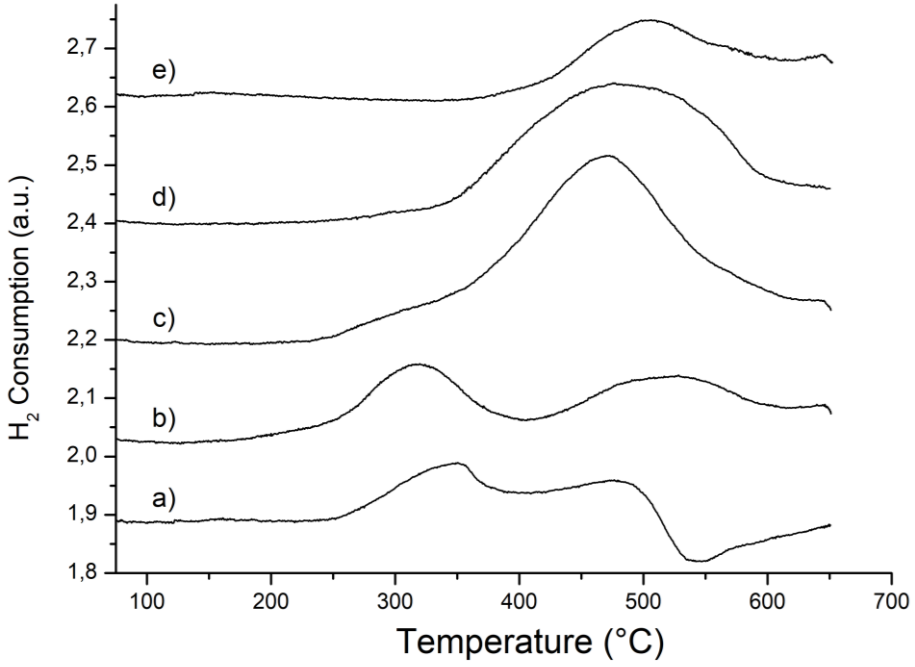

Fig. 5. 7 H_2-TPR profile of synthetized support oxides; a) CeO_2 , b)$Ce_{0.8}Ti_{0.2}O_2$, c) $Ce_{0.5}Ti_{0.5}O_2$, d) $Ce_{0.2}Ti_{0.8}O_2$, e) TiO_2

Hydrogen temperature-programmed reduction (H_2-TPR) analyses were conducted to reveal the reduction properties of the prepared supports. In Figure 5.7, the pure ceria sample exhibits two main absorption peaks at 350°C and a shoulder around 480°C, attributed to surface oxygen reduction [227] and a valley at about

540°C. However, doping ceria with titanium introduces oxygen vacancies into the structure as a result of lattice distortion caused by the substitution of smaller Ti^{4+} ions for Ce^{4+} ions. This distortion facilitates the reduction of CeO_2 at lower temperatures compared to the pure oxide [226]. This behaviour is particularly evident in Ce-Ti solid solutions that are rich in CeO_2, where the enrichment in oxygen vacancies lowers the reduction temperature.

Moreover, the reduction peaks observed between 300°C and 550°C in high surface area ceria samples should not be attributed to bulk reduction, which typically occurs above 700°C [228]. These peaks can instead be linked to structural heterogeneity, the presence of impurities, or simultaneous surface sintering phenomena common in high surface area materials (which may explain the occurrence of the small valley), as also noted by Vidal et al. (2000) [228].

Table 5. 3 Ceria - Titania MO reduced ratio calculated on the hydrogen consumption measured during the H_2-TPR experiment

	CeO_2	$Ce_{0.8}Ti_{0.2}O_2$	$Ce_{0.5}Ti_{0.5}O_2$	$Ce_{0.2}Ti_{0.8}O_2$	TiO_2
Ce^{3+}/Ce^{4+}	0.2	0.30	1	2.8	
$\frac{Ce^{3+}+Ti^{3+}}{xCe^{4+}+(1-x)Ti^{4+}}$	0.2	0.19	0.32	0.29	
Ti^{3+}/Ti^{4+}					0.06

It is important to note that the H_2 consumption integration was carried out over a temperature range consistent with the reaction conditions. When examining the first row of Table 5.3, reduction values were calculated assuming ceria as the only reducing species. However, the CeO_2-TiO_2 (20:80) sample shows a value clearly higher than unity, challenging this assumption. To address this, theoretical reduction values for Ce^{4+} and Ti^{4+} were weighted according to the stoichiometry of the solid solution, as shown in the second row of the table. The degree of reduction follows a Gaussian trend, peaking for the CeO_2-TiO_2 (50:50) mixed oxide. Although this trend is observed for the mixed oxide, it deviates from the typical behaviour of pure ceria, where reducibility tends to increase with higher surface area [229a], as shown in Table 5.2. This suggests that the incorporation of Ti^{4+} into the ceria lattice significantly modifies its reduction properties, facilitating the reduction of subsurface or bulk oxygen, similarly to what happens when CeO_2 is doped with zirconia to form a solid solutions [229b].

As discussed previously, the inclusion of Ti^{4+} ions into the ceria lattice significantly affects its reducibility. The introduction of titanium into the ceria structure induces lattice distortion, which generates oxygen vacancies that promote the reduction of bulk CeO_2 at lower temperatures than pure ceria [230]. This is particularly evident for Ce-Ti solid solutions rich in CeO_2. Additionally, the reduction peaks between 300°C and 550°C observed for ceria are primarily attributed to surface heterogeneities, the presence of impurities, or simultaneous surface sintering, but not bulk reduction, which generally occurs above 700°C [226]. The shift

in the reduction profile toward higher temperatures in Ce-Ti mixed oxides is therefore to be attributed to a convolution of surface and bulk phenomena at intermediate temperatures induced by the Ti-doping [227].

Aiming to prove an effective reduction of TiO_2 the TPR experiment was conducted analysing exhaust with mass spectrometry (TRP-MS). Moreover, a Simultaneous Differential Thermal Analysis (SDT) has been carried out and the resulting data are plotted in Fig. 5.8

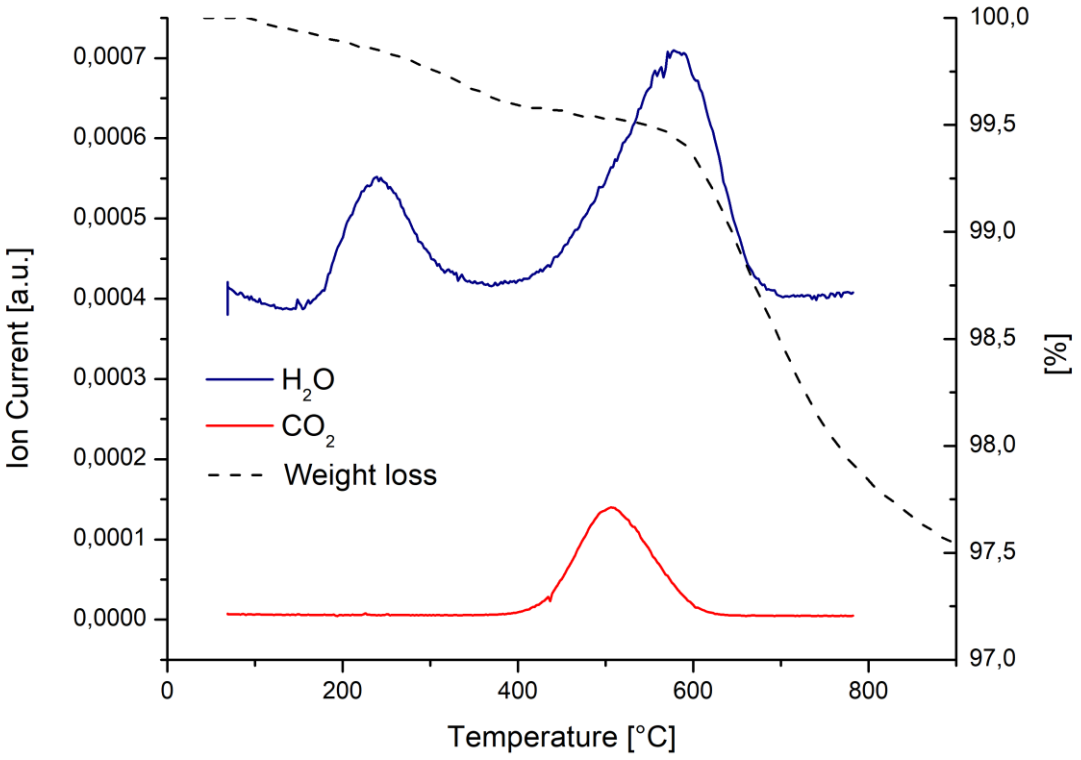

Fig. 5. 8 Water and CO_2 as product of reduction (left axes) and weight loss % (right axes) as a function of temperature.

The combined SDT and H_2-TPR-MS analysis of the TiO_2 sample, used as a support in the studied catalysts, revealed two distinct reduction processes, both accompanied by weight loss. The first reduction peak, observed at lower temperatures, is attributed to the surface reduction of TiO_2. This process is associated with the production of water (H_2O), as confirmed by mass spectrometry, and a noticeable weight loss detected by SDT, indicating the removal of surface oxygen. A second peak, appearing at a higher temperature and corresponding to a greater weight loss, suggests a deeper reduction of the material. However, at elevated temperatures, CO_2 is also released. This implies that the TPR profile (e curve in fig. 5.7) leads to an overestimation of the degree of reduction for pure TiO_2. Nonetheless, the pure titania support reduction is confirmed and the interaction between superficial reducing species in the mixed oxides is reasonable.

Diffuse Reflectance Spectroscopy – Support

Additionally, UV-diffused reflectance spectroscopy (DRS) was employed to gain insights into the photo-catalytic properties of the semiconductor mixed oxide support and calculate their related band gap according the Tauc method [231]. Figure 5.9 and Figure 5.10 shows the Kubelka-Munk function F(R)*hν in function of the incident photon energy (hν) in eV for the pure oxides and for the mixed oxides respectively while the calculated band gap for each sample is summarized in the table 5.4.

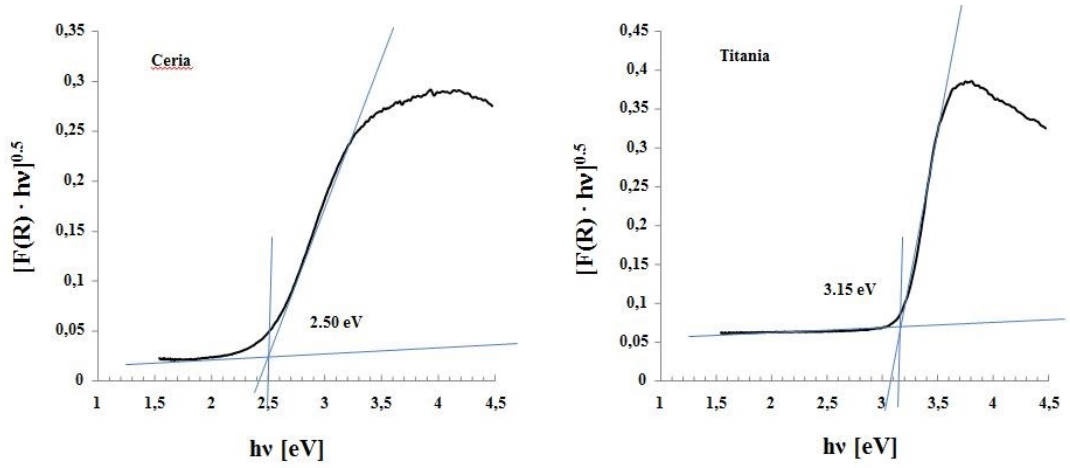

Fig. 5. 9 Tauc plot of the absorbance Kubelka-Munk function F(R) for Ceria and Titania Oxides – Calculated semiconductor band gap E_g

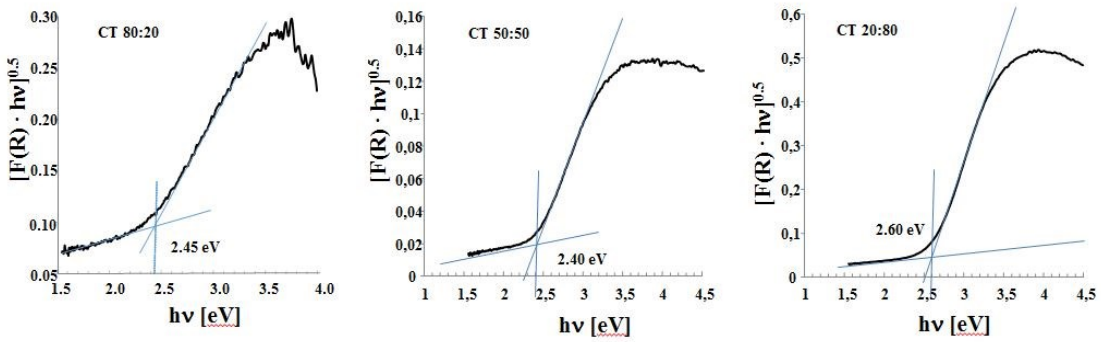

Fig. 5. 10 Tauc plot of the absorbance Kubelka-Munk function F(R) for Ceria-Titania Mixed Oxides – Calculated semiconductor band gap E_g

Table 5. 4 Band gap energy in eV calculated with Tauc Method

	E_g (eV)
CeO_2	2.50 ± 0.05
$Ce_{0.8}Ti_{0.2}O_2$	2.45 ± 0.05
$Ce_{0.5}Ti_{0.5}O_2$	2.40 ± 0.05
$Ce_{0.2}Ti_{0.8}O_2$	2.60 ± 0.05
TiO_2	3.10 ± 0.05

Ceria semiconductors typically display a band gap of around 3.3 eV, corresponding to the characteristic transitions between 4f states of Ce^{3+} sites in a sub-stoichiometric CeO_{2-x} lattice and the conduction band [232]. However, studies on nanoscale ceria have consistently reported a reduction in the band gap, with values shifting to the visible region (~2.7eV), primarily due to the generation of oxygen vacancies and lattice strain [233, 234]. This red shift aligns with the behaviour of our synthesized materials, where defect-induced modifications in ceria create localized states within the band gap, lowering the energy required for optical transitions. This effect is particularly pronounced in $Ce_{0.8}Ti_{0.2}O_2$ and $Ce_{0.5}Ti_{0.5}O_2$, where the synergistic interaction between CeO_2 and TiO_2 alters the electronic structure [235].

Titania (TiO_2), typically exhibiting a band gap of around 3.2 eV, undergoes significant electronic modifications when doped with cerium. Cerium-doped titania ($Ce_{0.8}Ti_{0.2}O_2$) demonstrates a red shift in its absorption band, extending its optical response into the visible region. This phenomenon, observed in several studies, arises from the introduction of Ce into the TiO_2 lattice, which generates oxygen vacancies, modifies the electronic structure, and introduces new defect states [236]. These alterations not only reduce the band gap but also enhance visible light absorption, a feature critical for photocatalytic applications under solar illumination.

Mixed cerium-titanium oxides with reduced band gaps, such as Ce-Ti systems, are particularly favourable for light absorption in the visible region, potentially boosting their photocatalytic performance. However, the reduction in the band gap is accompanied by challenges such as rapid electron-hole recombination, which may limit the photocatalytic efficiency of these materials, as highlighted in various studies [224].

This interplay between band gap reduction and defect state engineering highlights the dual role of doping and support interactions in tuning the optical and catalytic properties of mixed Ce-Ti oxides, making them promising candidates for visible-light-driven applications.

5.2 Rhodium supported catalytic materials characterizations.

The information about support materials is a useful baseline to analyse the impact of functionalization method described in chapter 4. X-Ray Diffraction, BET and porosimetry, H_2-TPR, DRS and TEM, were the techniques used also for the characterization of Rh-supported catalysts. The purpose was to understand any correlation between catalytic activity and catalyst properties and later explain also experimental evidence of a different catalytic behavior in reaction condition for different loading techniques. Additionally, optical properties are analysed to provide further indications of a potential plasmonic response. These and other insights are detailed in the following paragraph.

BET-Porosimetry and XRD analysis

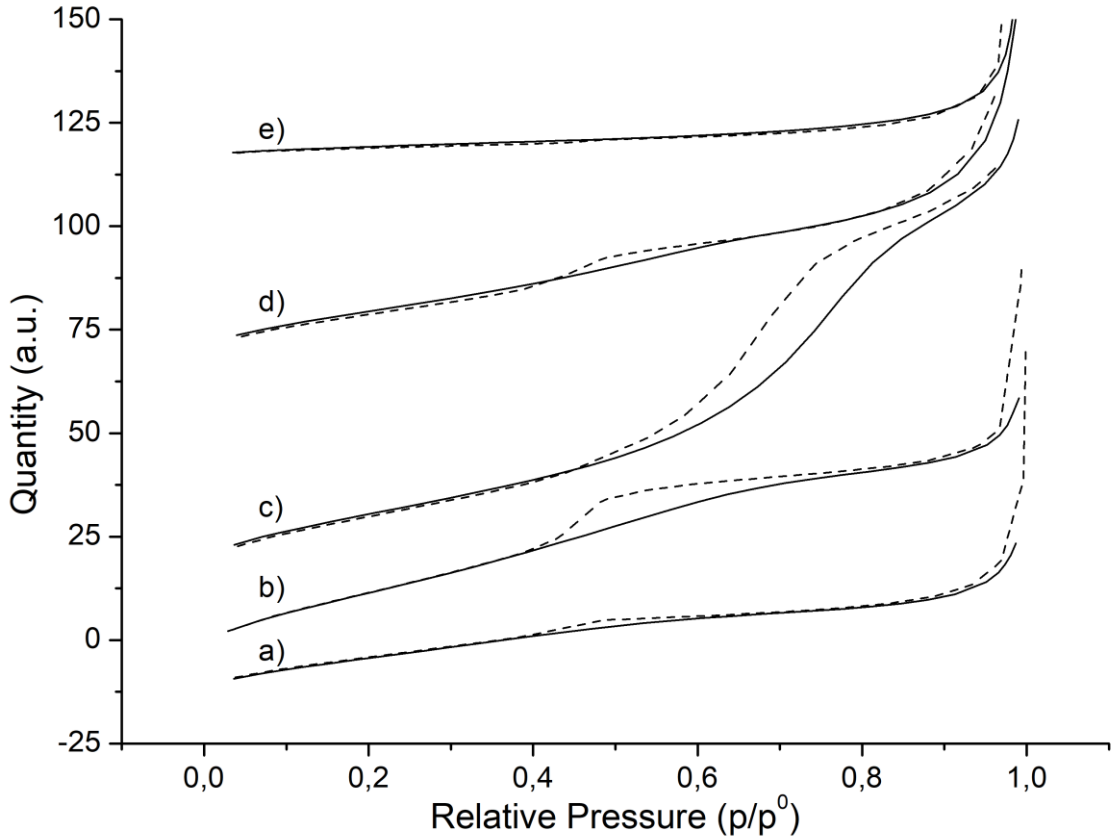

Fig. 5. 11 N_2-Adsorption and Desorption (solid and dashed lines respectively) Isotherms for all loaded support materials, pure oxides and compositions of mixed oxides. a) Rh/CeO_2, b) $Rh/Ce_{0.8}Ti_{0.2}O_2$, c) $Rh/Ce_{0.5}Ti_{0.5}O_2$, d) $Rh/Ce_{0.2}Ti_{0.8}O_2$, e) Rh/TiO_2

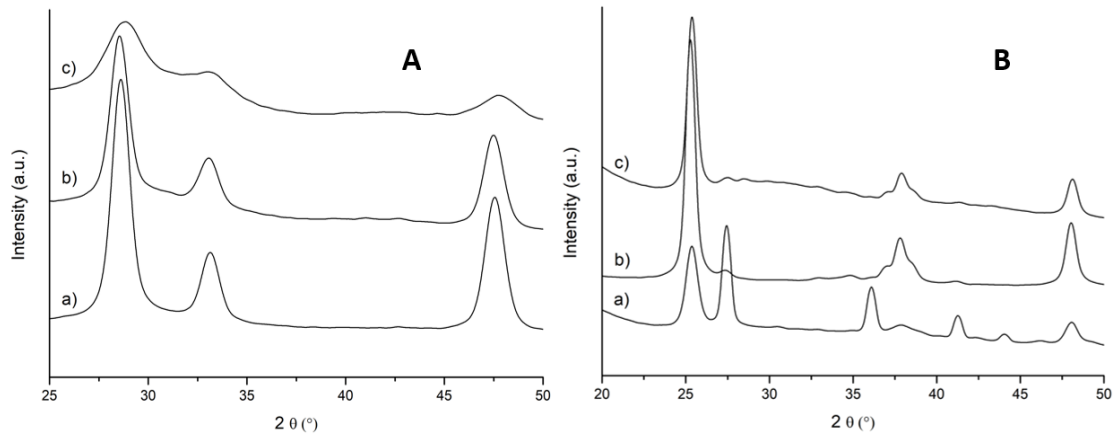

Fig. 5. 12 XRD Spectra comparison between CeO_2 and TiO_2 supported catalyst (A and B respectively): a) pure support, b) Rhodium supported catalysts synthetized by Ball Milling, c) Rhodium supported catalysts synthetized by Incipient Wet impregnation

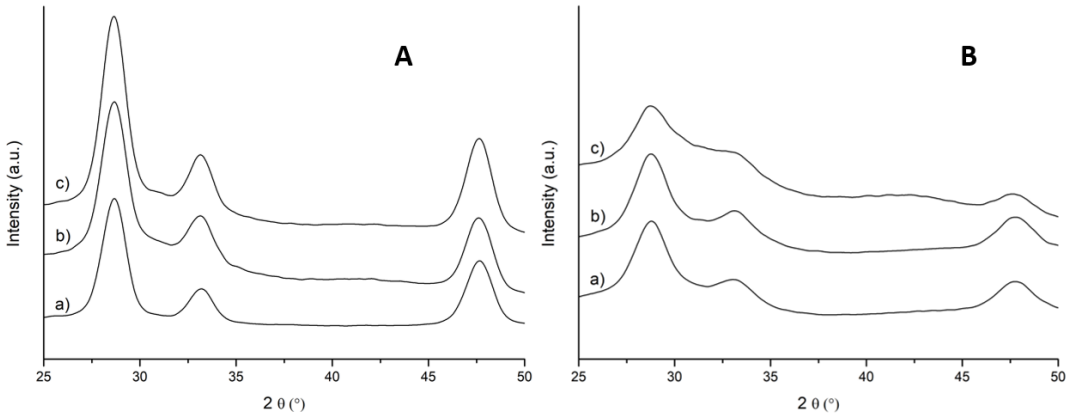

Fig. 5. 13 XRD Spectra comparison between CeO_2-TiO_2 mixed oxides, Ce:Ti(80:20) and Ce:Ti(50:50) respectively A and B: a) pure support, b) Rhodium supported catalysts synthetized by Ball Milling (BM), c) Rhodium supported catalysts synthetized by Incipient Wet impregnation (IW)

Table 5. 5 Crystalline Structure, Lattice Parameter, and Crystallite Size of TiO_2-CeO_2 Mixed Oxides supported Rhodium with different techniques.

Catalyst	Func. Method		a (nm)	c (nm)	size (nm)	Area Sup. [m^2/g]	Pore Volume [cm^3/g]	Pores Distrib. [nm]
Rh/CeO_2	**BM**	Fluorite	0.5387	-	3.2	57.4	0.042	4.7
	IW	Fluorite	0.5418	-	7.7	60.1	0.041	4.5
$Rh/Ce_{0.8}Ti_{0.2}O_2$	**BM**	Fluorite	0.5396	-	5.7	101	0.113	4.2
	IW	Fluorite	0.5399	-	5.1	105	0.112	4.1
$Rh/Ce_{0.5}Ti_{0.5}O_2$	**BM**	Fluorite	0.5393	-	2.4	91	0.186	7.0
	IW	Fluorite	0.5371	-	3.8	97	0.174	6.7
Rh/TiO_2	**BM**	Anatase	0.3782	0.9383	31.7	15.2	0.059	16.1
	IW	Anatase	0.3789	0.9534	31.5	13.8	0.055	16.4

The functionalization of cerium and titanium oxide supports with rhodium using Ball Milling (BM) and Incipient Wetness (IW) impregnation reveals distinct structural and surface modifications compared to the bare supports. A comparative analysis between these two functionalization methods, as well as with the original support materials, provides insights into their effects on crystallite size, lattice parameters, surface area, and porosity.

For the Rh-functionalized cerium oxide, the BM method (Fig. 5.12 A-c) results in a reduced lattice parameter (0.5387 nm) and a smaller crystallite size (3.2 nm) compared to the IW method (Fig. 5.12 A-b), which shows a lattice parameter of 0.5418 nm and a crystallite size of 7.7 nm. This suggests that BM introduces additional strain in the crystal lattice, likely due to the high mechanical forces involved, which leads to smaller crystallites. In comparison, the IW technique, which involves a more gradual impregnation process, allows

the rhodium particles to distribute with less induced lattice strain, resulting in larger crystallites. These differences in crystallite size have important implications for catalytic performance, as smaller crystallites, like those produced by BM, often enhance metal-support interactions, which are crucial for catalytic reactions. Interestingly, it appears that for cerium-containing samples, the measured surface area of IW samples is slightly higher than that of the ball-milled samples. This could be attributed to partial clustering of particles induced by the mechanical forces in the presence of the metal precursor during the milling process. This explanation is further supported by the observed inverse relationship between surface area and pore size distribution, which conversely increases. Analysing the XRD diffractograms of pure ceria-supported rhodium samples, it is reasonable to assert that the ball milling technique induces a reduction in the crystallite size compared to the pure support of the IW technique, as confirmed by the crystallite size values in Table 5.6. While this observation may seem contradictory to the BET-derived assumption of clustering, both scenarios could coexist. It could be hypothesized that the oxide support crystallites decrease in dimension and may aggregate due to superficial tension, indeed coalescence behaviour is influenced by the surface defect chemistry of the support and the metal [236b]. Moreover, a complex heterostructure may arise from the presence of a heterogeneous mixture of rhodium species in a sub-stoichiometric mixture of Rh^0/Rh^{3+} in strong interaction with the support nanoparticles, formed during acetate decomposition during thermal treatment following the mechanosynthesis, as suggested for other platinum group metals on ceria [237].

Additionally, a noticeable reduction in the lattice parameter "a" with mechanical treatment is observable, consistent with the reduction in crystallite size, suggesting a certain degree of inclusion of rhodium (ionic radius Rh^{4+}: 0.75 Å) into the support lattice (Ce^{4+}: 0.97 Å), which is not observed with the IW loading. This suggests that BM may promote stronger incorporation of rhodium into the cerium oxide lattice, leading to a more integrated structure with altered lattice properties. The hysteresis observed in the adsorption/desorption curves for Rh/CeO_2 further supports this hypothesis, showing limited hysteresis typical of microporosity and minimal mesopore contributions.

For $Rh/Ce_{0.8}Ti_{0.2}O_2$, BM (Fig. 5.13 A-c) produced a slightly smaller lattice parameter (0.5396 nm) and larger crystallite size (5.7 nm) compared to IW (Fig. 5.13 A-b), where the lattice parameter was 0.5399 nm and crystallite size 5.1 nm. The specific surface area is also notably affected by the functionalization methods: the BM-treated sample shows a slightly lower surface area compared to IW, indicating that the higher mechanical energy may lead to partial pore collapse or a denser packing of particles. The N_2-adsorption/desorption isotherm curves for this support show increased hysteresis relative to Rh/CeO_2, indicating a higher mesoporous contribution and a redistribution of porosity induced by mechanical treatment. This observation is consistent across other mixed oxide samples, where BM generally results in smaller crystallites and slightly altered textural properties.

For $Rh/Ce_{0.5}Ti_{0.5}O_2$, the BM method (Fig. 5.13 B-c) produced a smaller crystallite size (2.4 nm) compared to IW (3.8 nm), along with a slight increase in the lattice parameter (0.5393 nm vs. 0.5371 nm). The specific surface area of BM samples (91 m^2/g) is slightly lower than that of IW (97 m^2/g) (Fig. 5.13 B-b), which may reflect partial pore collapse due to the high mechanical energy. Additionally, the pore volume is slightly higher for BM (0.186 cm^3/g compared to 0.174 cm^3/g for IW), as is the average pore size (7 nm for BM vs. 6.7 nm for IW). These observations suggest that BM induces a redistribution of porosity, resulting in a broader pore size distribution and slightly denser packing. This redistribution is evident in the hysteresis curves, where BM-treated samples show pronounced hysteresis at higher relative pressures, indicative of meso-macropore transitions. The interplay between the reduced crystallite size and the altered porosity underscores the complex effects of mechanical treatment, which enhance metal-support interactions while slightly compromising surface area. This behaviour highlights the intermediate structural characteristics of the $Ce_{0.5}Ti_{0.5}O_2$ support, balancing features of both cerium and titanium oxides, and the potential for unique catalytic properties.

These results agree with previous findings by Gionco et al. (2013), who reported that mixed oxides of cerium and titanium display altered structural properties when subjected to mechanical treatments. Specifically, the formation of cerium titanate ($Ce_2Ti_2O_7$) with Rh addition may further contribute to unique properties, including a red shift in the band gap transition and enhanced reducibility [224]. This suggests that the strain introduced by BM can also favour the formation of mixed phases and the enhancement of catalytic properties.

The Rh-loaded TiO_2 samples provide further evidence of the impact of functionalization technique. BM (Fig. 5.12 B-c) sample resulted in a significant increase in crystallite size (31,7 nm) compared to the original anatase TiO_2 (20.7 nm), while IW led to a similar crystallite size of 31.5 nm. Despite the increase in crystallite size, BM treatment produced a slight increase in the surface area (15.2 m^2/g) compared to IW (13.8 m^2/g) (Fig. 5.12 B-b), which may indicate that BM enhances the dispersion of rhodium particles on the surface. This increase in dispersion is advantageous for catalytic applications, as it facilitates better accessibility of active sites. The adsorption/desorption curves for Rh/TiO_2 reveal minimal hysteresis, consistent with macroporous structures and non-adsorptive behaviour at lower pressures.

In contrast, both methods appeared to suppress the Rutile phase in titania, suggesting that the interaction between Rh and TiO_2, along with the post-calcination step, contributes to the stabilization of the anatase phase of TiO_2. Additionally, for the BM sample, it is also possible to hypothesize that mechanical stress favours lattice reorganization, thereby influencing the crystallite structure. Furlani et al. (2014) demonstrated, conversely, that high-energy ball milling of titania can lead to the transformation of anatase to rutile, although subsequent thermal treatment can partially reverse this transformation, depending on the milling time and conditions [238]. This implies that BM may facilitate phase transformations that are not achievable through traditional impregnation methods, thereby influencing the catalytic properties of titania-based supports.

More interestingly, BM showed an appreciable reduction in crystallite size for the $Ce_{0.5}Ti_{0.5}O_2$ support, while the IW method did not change this parameter compared to the unloaded support. Furthermore, along with the reduction in size, there was a slight increase in the lattice parameter "a" Considering that the ionic radius of Ti^{4+} is smaller than Rh^{3+}, partial inclusion into the lattice is reasonable, indicating the formation of an interface where Ti atoms are displaced, making room for rhodium species. These results align with the observations by Gionco et al. (2013), which indicated that mechanical treatments could lead to increased defect density and enhanced interaction between the active species and support, resulting in improved catalytic performance [224].

On the other hand, mechanical synthesis on the $Ce_{0.8}Ti_{0.2}O_2$ support did not influence the crystallite size of the prepared catalyst compared to the support. Additionally, as observed for the ceria-supported sample, the lattice parameter decreased for both BM and IW samples. However, for this support, the difference in this parameter is less marked between the two differently loaded samples. This observation suggests a different metal/support interface interaction, which could influence catalytic performance. The positive effects of Ball Milling are further corroborated by experimental catalytic tests reported in the literature. Studies have demonstrated that BM can enhance the catalytic activity of mixed oxides due to several factors: increased defect density, improved metal dispersion, and enhanced metal-support interaction. Watanabe et al. (2009) found that the mechanical forces during BM generate structural defects, including oxygen vacancies, which can significantly improve the reducibility of cerium oxide and enhance the oxygen storage capacity [226].

Similarly, Gionco et al. (2013) reported that mixed oxide phases with increased defect density, induced by mechanical treatment, exhibit better catalytic performance in oxidation reactions, partly due to enhanced redox properties and greater interaction between the active metal sites and the support [224]. A recent study by Danielis et al. (2020) further supports the beneficial effects of Ball Milling in metal-ceria systems, particularly in improving methane oxidation activity [237]. The study highlighted that Pd/CeO_2 catalysts prepared by dry milling showed superior catalytic performance compared to those prepared by traditional incipient wetness impregnation. This enhanced performance was attributed to the formation of a mixed Pd-CeO_2 amorphous layer on the surface, which creates a unique interface conducive to methane activation. This study provides additional evidence that mechanical treatments like BM can significantly alter the metal-support interface, leading to enhanced catalytic properties and improved metal dispersion.

In summary, the functionalization of cerium and titanium oxide supports with rhodium via Ball Milling shows promising effects in terms of reducing crystallite size and enhancing catalytic properties through increased defect density and an improved metal-supports synergism. Compared to Incipient Wetness impregnation, BM produces supports that are structurally more strained, with smaller crystallites and enhanced metal-support interactions, which are beneficial for catalytic activity.

H_2 - Temperature Programmed-Reduction characterization- Rh supported catalysts

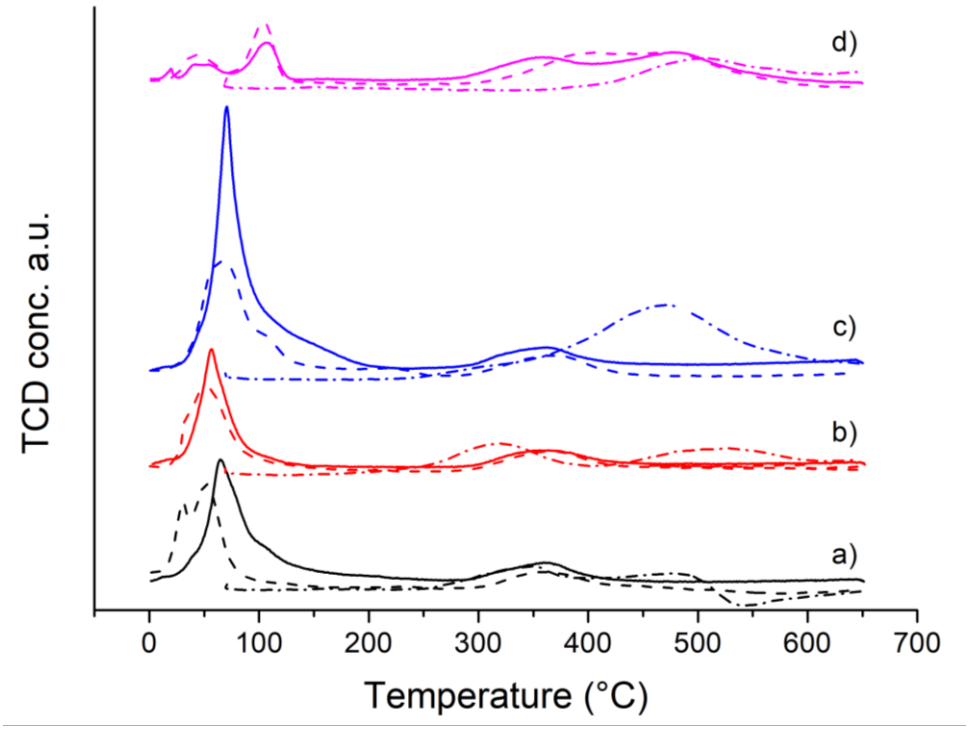

Fig. 5. 14 TPR profile of BM (solid line) and IW (dash line) rhodium supported catalyst on Ceria-Titania oxides compared with TPR profile of the only support (dot-dash line); a) Rh/CeO_2, b) Rh/CeO_2-TiO_2 (80:20), c) Rh/CeO_2-TiO_2 (50:50), d) Rh/TiO_2

Table 5. 6 Reduction temperature of differently supported IW and BM rhodium samples, for different reducing species at different temperature intervals - H_2 consumption percentage with respect to the reduction of Rh species on different series of catalysts

Sample	IW Catalysts			BM Catalysts		
	$Rh^{3+} \rightarrow Rh^0$ (°C)	MO_x-Rh (°C)	H_2 cons. %	$Rh^{3+} \rightarrow Rh^0$(°C)	MO_x -Rh (°C)	H_2 cons. %
Rh/CeO_2	51	360	137	64	359	187
$Rh/Ce_{0.8}Ti_{0.2}O_2$	53	363	113	56	355	127
$Rh/Ce_{0.5}Ti_{0.5}O_2$	64	366	165	70	361	196
Rh/TiO_2	47-103	390-480	119	18-51-105	353-475	96

The results of the H_2-TPR experiments on Rh catalysts supported on cerium oxide, titanium oxide, and their solid solutions reveal significant differences depending on the preparation method, namely incipient wetness impregnation (IW) and Mechanosynthesis (BM). The reduction temperatures of the samples, attributed to a combination of processes including both the reduction of the noble metal oxide ($Rh_2O_3 \rightarrow Rh^0$) and the reduction of the oxide support (e.g., $Ce^{4+} \rightarrow Ce^{3+}$ or $Ti^{4+} \rightarrow Ti^{3+}$), are similar between IW and BM in ceria-based and ceria-titania solid solutions. However, pure titania samples exhibit higher reduction temperatures over a broader range, indicating the lower effectiveness of this support in dispersing and activating the metal.

The higher consumption of H_2 with respect to the expected consumption to reduce the loaded metal (see formula below) is a measure of the phenomena of H_2 spillover. This term lamps different phenomena such

as the transfer of atomic H on the surface of support or a promotion and enhancement of support reduction due to a strong metal support interaction. Differently functionalized catalysts were also compared for this parameter.

$$H_{2_{cons}}\% = \frac{consumed\ H_2\ moles}{theoretical\ H_2\ moles\ to\ reduce\ all\ Rh^{3+} \rightarrow Rh^0}; \quad Eq.(5.1)$$

BM-prepared catalysts consistently show higher spillover values compared to their IW counterparts, reflecting improved Rh dispersion and stronger metal-support interactions. For instance, in $Rh/Ce_{0.5}Ti_{0.5}O_2$, the highest spillover reaches 196% for BM and 165% for IW, highlighting the critical role of synthesis in optimizing catalyst properties. More in general is clear how the metal functionalization method is crucial on this aspect for every ceria containing sample, indeed we observe, except for Titania supported sample, a higher value of hydrogen consumption for samples prepared by ball-milling method. In the next paragraph TEM images may explain the exception of Rh/TiO_2 and later suggest clues of the studied reaction mechanisms.

The interaction between Rh and its support significantly influences reducibility and catalytic behaviour. For $(IW)Rh/TiO_2$, reduction profiles exhibit peaks at 47°C and 103°C, which are indicative of processes involving the reduction of Rh species (e.g., $Rh^{3+} \rightarrow Rh^{1+}$ and $Rh^{1+} \rightarrow Rh^0$), on the other hand BM sample shows slightly higher temperature for the same reduction (51°-105°C) and a minor peak at 18°C which suggests the presence of highly dispersed RhO_x nanoparticles that are particularly reducible or the presence of oxygen species physisorbed on the surface. However, the hydrogen consumption for $(IW)Rh/TiO_2$ exceeds stoichiometric requirements for Rh_2O_3 reduction alone, further supporting the hypothesis that additional reduction processes, such as the partial reduction of the support, are also occurring in this temperature range, this effect for BM sample apparently seem not to happen because of different metal nanostructured formations due to the functionalization method. The observed shift of titania surface oxide reduction to lower temperatures (~350°C) of Rh/TiO_2 with respect to unloaded sample, and particularly when mechanosynthesis is used, highlights the strong metal-support interaction (SMSI) effect, which stabilizes Rh species and facilitates electronic interactions [239, 240]. Furthermore, hydroxylated surfaces of TiO_2 enhance hydrogen spillover, while dehydroxylation at higher temperatures diminishes this effect, underscoring the importance of maintaining surface hydroxyl groups for efficient catalytic activity [241, 229].

Ball Milling metal loading on mixed oxide in presence of Ceria seems to increase metal/support interaction, the increase of RhO_x reduction temperature is evident and coherent with the H_2 consumption and spillover effect consequently, the lowest increase in temperature corresponds to the lowest increase in consumption.

On the other hand, $(BM)Rh/Ce_{0.8}Ti_{0.2}O_2$ shows the highest shift to lower values for MO_x -Rh reduction temperature, while the same peaks for $(BM)Rh/CeO_2$ and $(BM)Rh/Ce_{0.5}Ti_{0.5}O_2$ are almost unvaried. Those

observations should point out how critical the metal/support interaction may be when catalytic activity will be analysed as a function of the support composition and the amount of titania in the solid solution.

We can conclude that Rh enhancing the reducibility of the system by promoting the formation of oxygen vacancies and facilitating hydrogen spillover in presence of ceria and a mechanosynthetic process. This behaviour aligns with observations in ceria-rich systems, where the interaction between Rh and CeO_2 clusters has been shown to promote reversible H_2 adsorption and efficient redox cycling [229, 242]. Mixed oxides such as $Ce_{0.5}Ti_{0.5}O_2$ display intermediate characteristics, with titanium contributing structural stability but limiting the synergistic redox interactions seen in cerium-rich compositions [240].

Transmission Electron Microscopy – Functionalization method effect

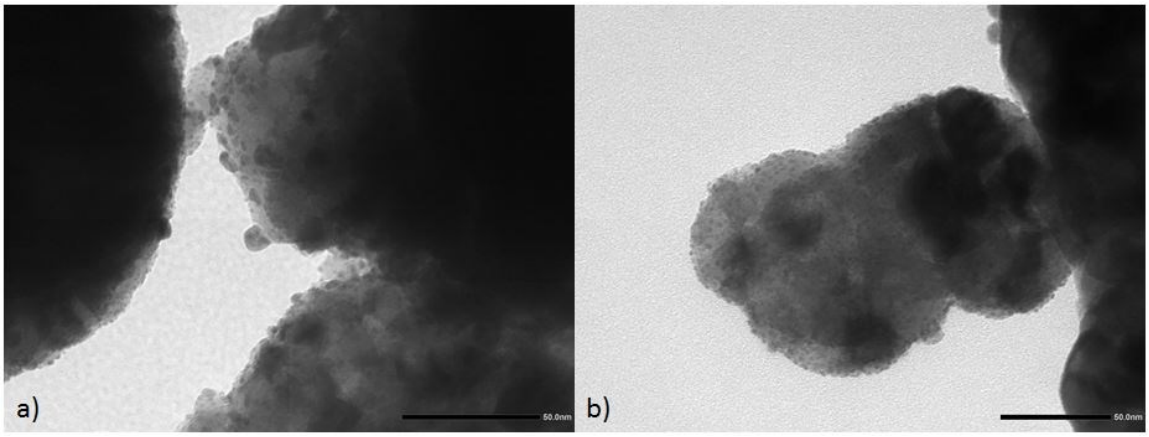

Fig. 5. 15 TEM images of Rh/TiO_2 a) Ball Milled, b) Incipient Wet impregnation.

To explore the surface morphology of the prepared catalyst a TEM observation of both BM and IW reduced catalyst were done. As an example, we report in figure 5.15 the observable differences between the two functionalization method consequences on the distribution of the rhodium metal. We can observe (5.15a) the formation of protruding quasi-spherical metal nanoparticles, like already observed for platinoids metals like Rhodium [237, 243], while in other zones the metal darker zones seem to be sparser, alike the metal crystal growth was preferential on sites. On the other hand, smaller and more uniformly dispersed metal particle appear in fig. 5.15b for IW samples. In conclusion the lower spillover shown by ball milled Rh/TiO_2 appear to be due to a different growth of the rhodium metal formations on the support, reasonably due to mechanical stress.

Diffuse Reflectance Spectroscopy – Catalysts

Both pure supports and rhodium loaded BM prepared catalysts were also studied with the DRS technique and the absorption spectra are in figures below.

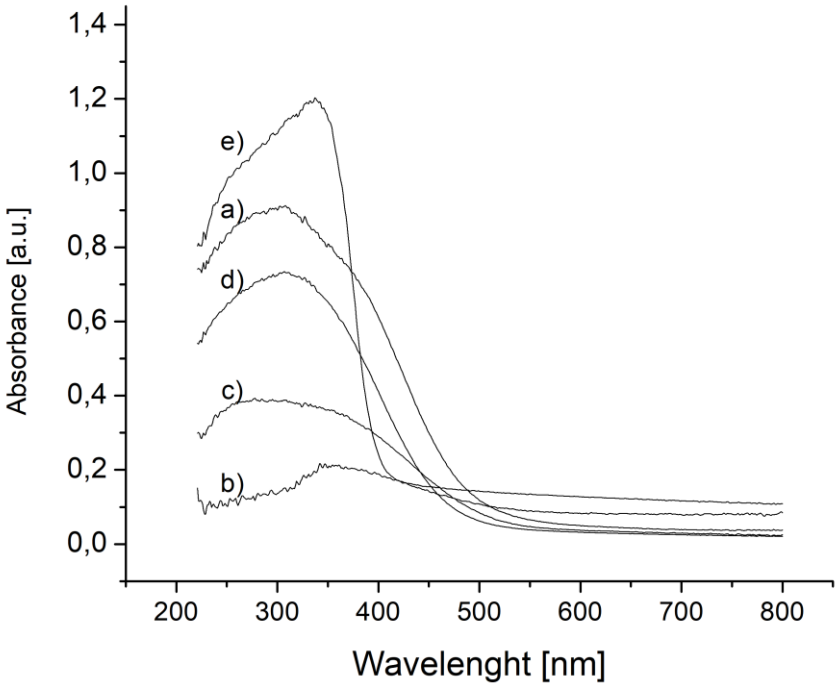

Fig. 5. 16 DRS derived Absorbance of Ceria and Titania pure and mixed oxide supports as a function of the wavelength. a) CeO_2 , b)$Ce_{0.8}Ti_{0.2}O_2$, c) $Ce_{0.5}Ti_{0.5}O_2$, d) $Ce_{0.2}Ti_{0.8}O_2$, e) TiO_2

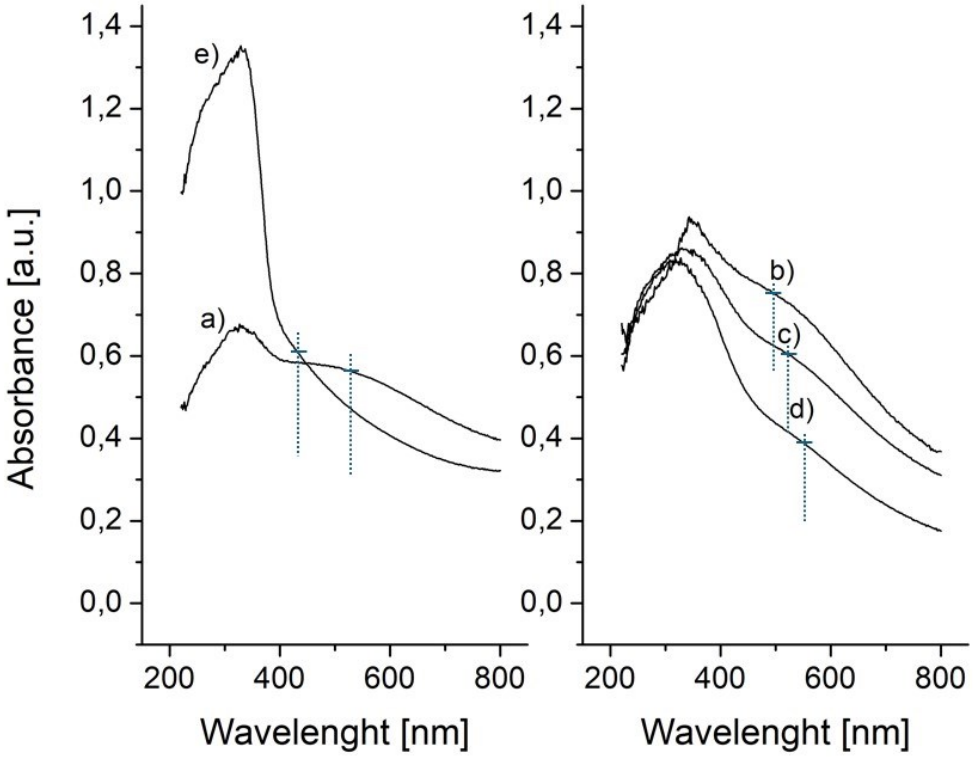

Fig. 5. 17 DRS derived Absorbance of Ceria and Titania pure and mixed oxide supported Rhodium catalysts as a function of the wavelength. a) Rh/CeO_2 , b) $Rh/Ce_{0.8}Ti_{0.2}O_2$, c) $Rh/Ce_{0.5}Ti_{0.5}O_2$, d) $Rh/Ce_{0.2}Ti_{0.8}O_2$, e) Rh/TiO_2

It is worth noting that in the presence of wide-ranging absorption peaks, as observed in Fig. 5.17, the evaluation of the band gap using the Tauc method, as shown in Fig. 5.9/10, may not be feasible [244]. This

limitation arises from the presence of metals and peak broadening. Therefore, we only present the Kubelka-Munk function of the collected reflectance spectra.

As previously discussed, ceria semiconductors typically display a band gap of around 3.3 eV, which can be significantly reduced due to defect-induced modifications such as oxygen vacancies and lattice strain, especially in nanoscale ceria. These phenomena, extensively examined in $Ce_{0.8}Ti_{0.2}O_2$ and $Ce_{0.5}Ti_{0.5}O_2$ systems, lead to a red shift in the absorption edge, extending the optical response into the visible region [232, 233, 234].

In Fig. 5.17, Rh/CeO_2 and Rh/TiO_2 ((a) and (e) profiles respectively) catalysts are presented. For the ceria-supported sample, the presence of a broadened absorption peak in the visible range is present, specifically in the green light around 530 nm, especially comparing it with support profiles in Fig. 5.16. These kinds of peaks are typical of the localized surface plasmon resonance (LSPR) effect [245, 246, 162]. Rh/TiO_2 does not exhibit this broad absorption peak as clearly; however, observing the absorption scales on the Y-axis, this difference is likely due to the dominant absorption in the UV range (<400 nm). Nonetheless, a distortion of the tail is visible, and its absorbance is comparable with $Rh/Ce_{0.8}Ti_{0.2}O_2$ sample.

Interestingly, for the mixed oxide supports, the visible region absorption spectra reveal a shoulder peaking at around 500-550 nm, which is most intense at around 500 nm in the 80:20 composition and intensity decreases with increasing titania content, however the center of the shoulder seam to shift also to 550 nm in the same way.

Further examining the UV range peaks, both catalysts exhibit a broadened absorption peak along with a shoulder appearing below 280 nm. The higher-energy photon absorption peak varies depending on the support and corresponds to the absorption peaks of ceria and titania semiconductors. Interestingly, the 80:20 composition shares the ~350 nm peak with TiO_2, both in the bare supports (Fig. 5.16b and e) and in the loaded samples (Fig. 5.17b and e). This observation suggests that this specific peak should be attributed to the presence of Titania and a peculiar interaction within the solid solution of this oxide with metal nanoparticles, on the other hand, we observed a decreasing intensity trend as Ti content increase. We also observe, comparing support and rhodium-loaded samples in Fig. 5.18, that the relative increase in intensity when loading the mixed oxide support is the highest for the 80:20 composition, decreasing with increasing titania content. This trend is accompanied by a noticeable blue shift of the peak, which can be attributed to rhodium plasmonic absorption in the UV range [247, 248]. Observing Ceria (100:0) loaded Vs unloaded sample to be the only sample we can not appreciate an increase in UV region absorption, the rhodium absorption peak shift should be explained with a particular interaction with titania in the solid solution when its content is decreasing, finding the optimum with $Ce_{0.8}Ti_{0.2}O_2$ composition.

Rh/TiO_2, characterized by its significantly larger crystallite size (~315 Å) and lower surface area (13.8-15.2 m^2/g), emphasizes UV-range absorption due to its crystalline nature. The pore distribution in Rh/TiO_2 (161-164 Å) underscores its distinct optical behaviour compared to ceria-containing samples. The structural differences of TiO_2, compared to the other samples, influence its light absorption properties observed in the DRS spectra, highlighting a strong interplay between morphology and optical characteristics in these catalysts, driving its interaction with rhodium metal nanoparticles and its response to light as will be discussed later.

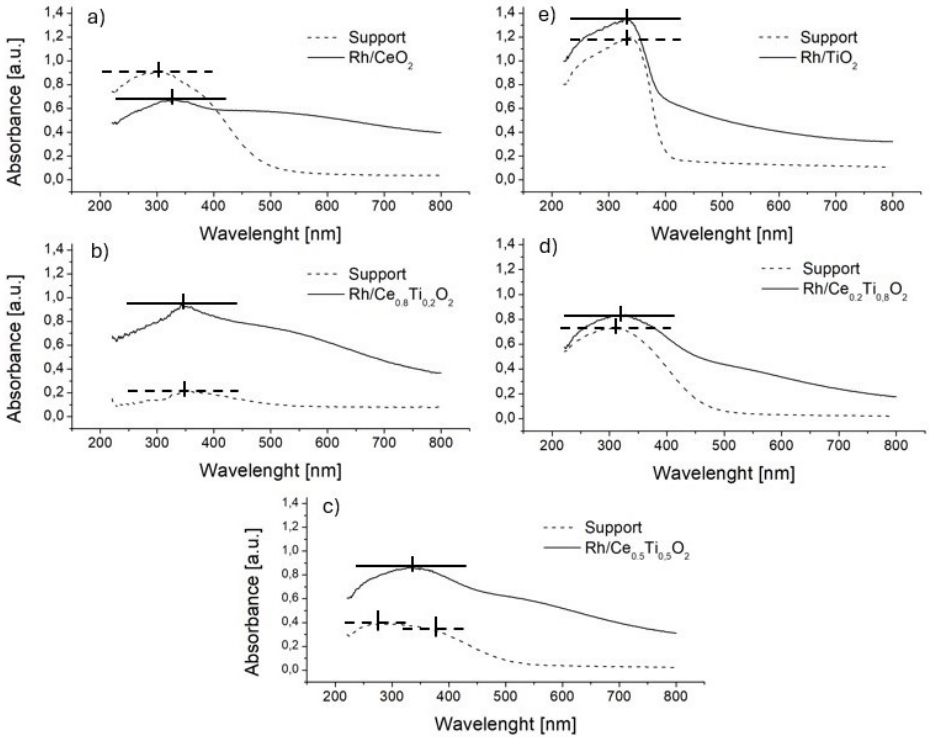

Fig. 5. 18 DRS derived Absorbance of Ceria and Titania pure and mixed oxide supported Rhodium catalysts as a function of the wavelength (solid line), comparison with pure support DRS profiles (dash line). a) Rh/CeO_2, b) $Rh/Ce_{0.8}Ti_{0.2}O_2$, c) $Rh/Ce_{0.5}Ti_{0.5}O_2$, d) $Rh/Ce_{0.2}Ti_{0.8}O_2$, e) Rh/TiO_2

The optical changes of samples correlate well with structural data derived from XRD and BET measurements. For instance, $Rh/Ce_{0.8}Ti_{0.2}O_2$, characterized by its intermediate crystallite size (~51-57 Å) and highest surface area (101-105 m^2/g), demonstrates enhanced light interaction within its porous matrix, amplifying the convoluted absorption effects observed. Similarly, the decreasing pore size distribution (42-41 Å) with increasing titania content suggests a denser and potentially more uniform solid solution. This structural evolution likely modifies the electronic interactions within the lattice and enhances light scattering effects, contributing to the observed spectral shifts.

The presence of a shoulder in the visible range (~550 nm) in rhodium-loaded samples suggests additional contributions from metal-support interactions, including electronic coupling and plasmonic effects. The

morphological properties of the mixed oxides, such as their crystallite size and pore structure, play a critical role in shaping these interactions. For example, the intermediate characteristics of $Rh/Ce_{0.8}Ti_{0.2}O_2$ may provide an optimal balance of porosity and surface area, enhancing light absorption and scattering effects within the material's structure.

Moreover, the apparent blue shift in the visible range absorption peak could reflect changes in the localized electronic structure of the mixed oxide solid solutions. As the titania content increases, oxygen vacancies and defect states introduced by cerium doping may decrease, reducing the density of mid-gap states responsible for visible light absorption. This trend aligns with the reported behaviour of cerium-titanium mixed oxides, where the interplay between band gap tuning and defect engineering governs their optical and electronic properties [232, 236].

These findings underline the significant influence of the morphological and electronic properties of mixed oxides on their optical behaviour, which is particularly evident in rhodium-loaded samples. The observed spectral shifts and intensity changes highlight the interplay between structural characteristics, electronic interactions, and light absorption properties, making these materials promising candidates for thermo-photo catalytic applications under visible light.

6 Experimental campaign

In this chapter, we explore the experimental investigations into the catalytic performance of the materials studied in this research. Specifically, we focus on the catalytic materials described in detail in Chapter 5, comparing their performance in terms of methane (CH_4) production yields and carbon dioxide (CO_2) conversion rates. Particular emphasis will be placed on the improvements achieved through the light-induced plasmonic photothermal effect.

In subsequent sections, we will examine a series of experiments designed to assess how variations in reaction conditions influence catalytic activity. This analysis aims to provide a comprehensive understanding of the enhancements driven by light stimulation under optimal reaction conditions.

6.1 Experimental Data collection

The set of materials used and compared in the experimental campaign were previously deeply described, here a summary table is reported:

Type	Support material	Functionalization – Rh 4%wt	
	Sol-Gel	Impregnation (IW)	Ball Milled (BM)
CeO_2	C-Ce		✓
	Ce_SG	✓	✓
TiO_2	C-Ti		✓
	Ti_SG	✓	✓
$Ce_{0.8}Ti_{0.2}O_2$	CeTi(80:20)	✓	✓
$Ce_{0.5}Ti_{0.5}O_2$	CeTi(50:50)		✓
$Ce_{0.2}Ti_{0.8}O_2$	CeTi(20:80)		✓

[a-]C-Ce and C-Ti indicate purchased materials

As previously mentioned, the production of comparison materials aimed to investigate the influence of metal-support interactions on their catalytic behaviour through experimental analysis. Emphasis was placed on maximizing yields at lower temperatures through the utilization of light. The selection of experimental conditions was guided by key parameters impacting the methanation reaction, as outlined in *materials and methods* chapter. This allowed us to enhance catalytic activity toward the desired product while optimizing the resulting plasmonic photothermal effect.

Here are the specific experimental conditions employed:

- **Experiment Structure Type**: Isothermal Step Experiment

- **Working Temperature Range**: 250-400°C
- **Gas Mix**: A ratio of 5.5 parts hydrogen (H_2) to 1 part carbon dioxide (CO_2), composed of 61% H_2, 11% CO_2, and 28% He (used as a carrier gas and Mass Spectrometer internal standard), all at ambient pressure.
- **Light Filter**: A Heat-Reflecting Near-Infrared (NIR) to Infrared (IR) Filter with an 800-1100 nm cut-off wavelength.
- **Flow Rate (ϕ)**: Set at 35 ml/min.

These conditions were carefully selected based on insights from relevant literature, the expertise developed within our research group, and prior experimental findings. The isothermal step experiment structure, operating within a 250-400°C temperature range, ensures a robust investigation of catalytic processes under stationary conditions. By maintaining hyperstoichiometric conditions with a gas mix of 61% H_2, 11% CO_2, and 28% He with 35 ml/min total flow rate, side products reactions are minimized, and the yield per unit mass of catalyst is maximized. The incorporation of a Heat-Reflecting Near-Infrared (NIR) to Infrared (IR) filter (800-1100 nm cut-off) further allows for precise evaluation of the influence of light on the system. This deliberate approach enables an in-depth analysis of the catalyst's behaviour and interactions with the support material, enhancing our understanding of the methanation reaction at lower temperatures under light exposure. Moreover, in this section, we will conduct comparisons to achieve two main objectives:

1. **Metal Loading Techniques Comparison**: We will investigate how different metal loading techniques, specifically Ball Milling (BM) and Incipient Wet Impregnation (IW), affect catalytic performances. This analysis aims to experimentally validate some of the assumptions made during the characterization results described in Chapter 5 regarding the different resulting materials.

2. **Metal-Support Interaction Effect Investigation**: We will delve into the impact of the interaction between the metal catalyst and different compositions of the Ceria-Titania support on experimental performances. In this investigation, Ball Milling will serve as the reference metal loading technique.

By conducting these comparisons and experiments, we aim to gain valuable insights into how various metal loading techniques and the composition of the support material influence catalytic performances leading to a deeper understanding of the factors that govern catalytic reactions and the photo-thermal promotion, thus paving the way for potential optimizations in advanced catalyst design and performance.

6.2 Experimental Data discussion

As introduced in the previous paragraph, a comparison graph described in Chapter 4 (Fig. 4.6) has been employed to identify the top-performing materials in the context and with the objectives outlined earlier. This graph serves as a visual tool to help assess and rank the catalyst materials based on their performance in CO_2 conversion and CH_4 yield, obtained under well-established reaction conditions at a temperature of 300°C, aligning with our experimental goals and criteria.

Metal Loading Techniques Comparison

As introduced in Chapter 4 and 5, the method used for functionalizing the metal on the catalyst's surface can significantly influence its catalytic performance. This influence stems from various concurrent factors, including variables like metal dispersion and particle size [249, 250, 251], which can impact the metal's reducibility [252], the abundance of active sites [253], the morphology of metal/support interface, and consequently, the contribution of the plasmonic photothermal effect to the overall catalyst activity [254].

It's important to note that these factors are not the sole determinants affecting the reactivity of the catalyst in a thermo-photo catalytic system. There are other variables at play as well, these factors themselves are influenced not only by the loading technique, but also by support [253, 255] with respect to the different functionalization processes. However, in our investigation, the choice of a functionalization technique that enhances performance and ensures repeatability is a crucial detail. Such a choice can have a profound impact on the reliability and effectiveness of the catalytic system, aligning with our research objectives. For this reason, we decided to investigate the catalytic response in the presence of light and then compare the dispersed metal characteristics to justify the observed behaviour.

In the figure below (Fig. 6.1), we present a comparison of catalytic performance in Dark (solid symbols) and Light (empty symbols) conditions for different supports loaded with the same amount of metal, using Incipient Wet Impregnation (IW) and Ball Milling (BM) techniques, as previously described.

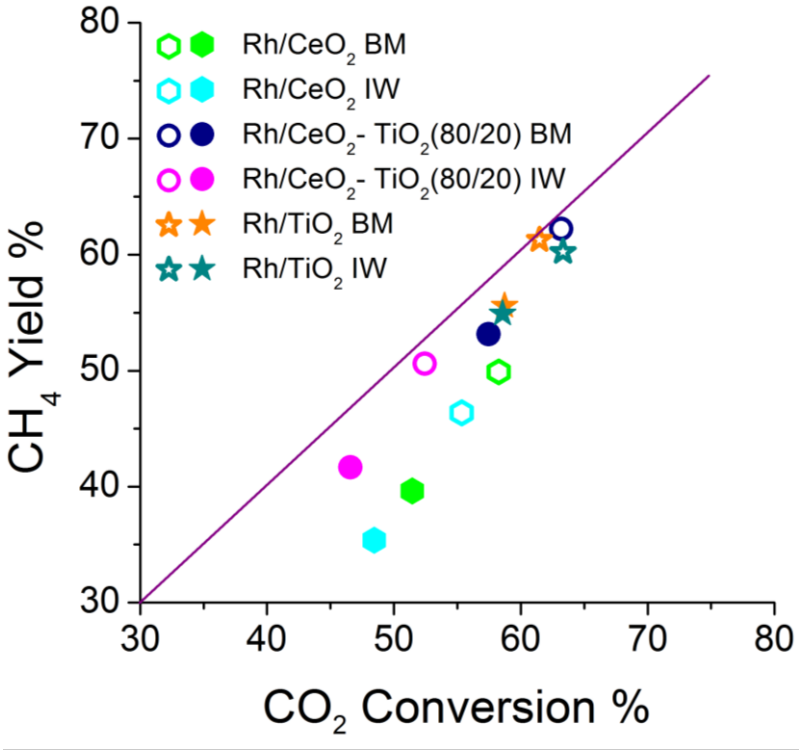

Fig. 6.1 Comparison in Dark(solid) and Light (empty) condition: Tchamber =300°C, 61% H_2/11% CO_2/28% He, ϕ=35ml/min, for different supports metal loaded by Incipient Wet impregnation (IW) and Ball Milling (BM)

When considering dark activity, it's evident that samples prepared using the Ball Milling (BM) technique exhibit superior yields compared to the Incipient Wet Impregnation (IW) samples. Notably, in the presence of Ceria, the CO_2 conversion is significantly improved, accompanied by a minor enhancement in terms of selectivity (distance from the bisector). Furthermore, the most significant improvement when using BM instead of IW is observed in the case of Rhodium supported on Ceria/Titania (80/20). Conversely, the Titania-supported sample shows minimal enhancements in both conversion and selectivity. Upon examining the results in the presence of light, the enhancements in dark conditions are relatively consistent and higher for samples containing Ceria compared to the Titania-supported metal samples. Additionally, the improvement in selectivity in the presence of light is quite similar for all the samples. These observations suggest that employing milling technique to load Ceria-Titania mixed oxide supports may be more effective at enhancing catalytic activity under light conditions than single metal oxide-supported metal samples. As previously discussed in this work about H_2-TPR experiments (Par. 5.2), mechanosynthesis appears to modify the interaction between metal and support. This effect is particularly evident when examining Rh/CeO_2-TiO_2 (80:20), where remarkable yield improvements were observed. This effect is particularly evident when examining Rh/CeO_2-TiO_2 (80/20), where remarkable yield improvements were observed.

Metal/Support Interaction Effect Investigation

As discussed above, the choice of support material can have a critical influence on the characteristics of the catalyst and, consequently, on its overall performance. In our case, it was of particular interest to investigate how the composition of the Cerium/Titanium mixed oxide support would impact the results. We aimed to understand if there is any correlation between the metal-loaded samples of these compositions and the introduction of light stimuli, beyond their sole thermo-catalytic activity. In other words, this investigation aims at exploring how different support compositions may interact with light stimulation and influence catalytic behaviour, providing valuable insights into the multifaceted nature of catalytic reactions under varying conditions.

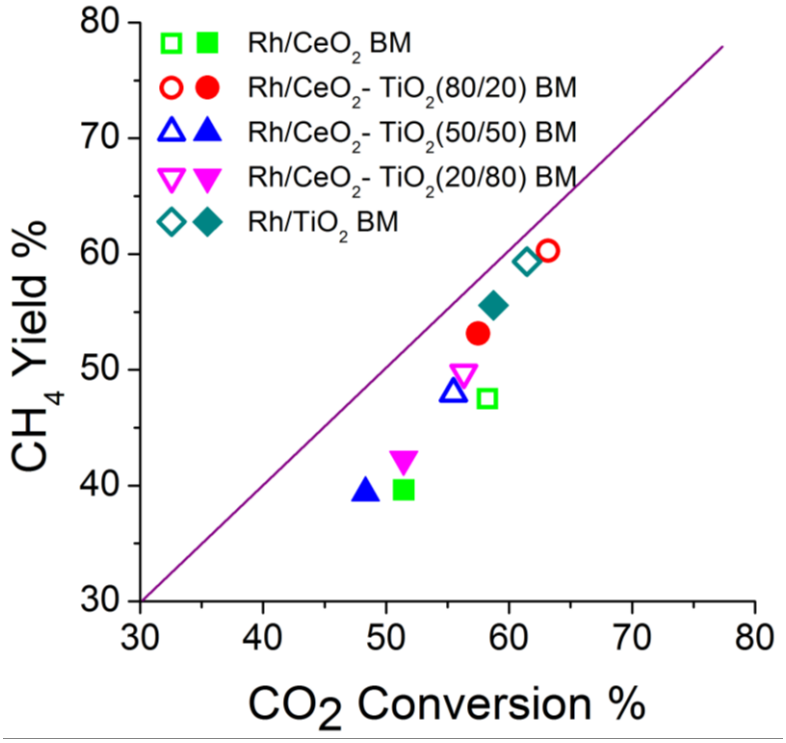

Fig. 6.2: Comparison in Dark(solid) and Light (empty) condition, : Tchamber =300°C, 61% H2/11% CO2/28% He, ϕ=35ml/min, for different Ceria-Titania mixed oxide composition supporting Ball Milling (BM) loaded 4%wt Rhodium.

In the graph above, experimental results in both Dark and Light conditions are presented for a set of materials where rhodium was loaded onto various compositions of Ceria-Titania mixed oxide, including the extreme cases where the metal is loaded onto pure Cerium or Titanium oxides ($Ce_xTi_{1-x}O_2$; $x = 0,0.2,0.5,0.8,1$).

Immediate observations reveal that both Rh/TiO_2 and Rh/CeO_2-TiO_2 (80:20) exhibited the best performances under our experimental conditions. Specifically, Rh/TiO_2 showed the best results in Dark conditions, both in terms of yield and selectivity to the product (value closer to the bisector, in the right part of the graph). Conversely, Rh/CeO_2-TiO_2 (80:20) exhibited the highest yield when exposed to light. Interestingly, these two materials were significantly more active than all the others, especially when compared to Rh/CeO_2, which

showed the worst selectivity and shared the lowest yield with Rh/CeO_2-TiO_2 (50:50); slightly better yielded resulted the yield of Rh/CeO_2-TiO_2 (20:80).

Additionally, it is worthy to note that Rh supported CeO_2 based catalysts exhibited a higher enhancement when exposed to light with respect to the Rh/TiO_2. This latter showed the highest performance in dark conditions, conversely, when considering the plasmonic contribution (see Fig.4.8) to the reaction, the order is reversed.

All the results suggested that the photo thermal methanation is drowned by the synergism of different parameters. A more in-depth investigation to better interpret the role of metal-support interactions, the redox properties of the support and the synergistic effect of plasmonic phenomena has been described in the following paragraphs.

6.3 Investigation on metal/support interface characteristics

The metal-support interaction plays a crucial role in catalyst performance, especially when reaction conditions are fixed. Given that rhodium metal is a constant parameter, the synergy between rhodium and the support is critical to maximizing material performance. Furthermore, this becomes even more important when the support is a mixed oxide because the interaction between the oxides can lead to unpredictable outcomes which need to be explained to enhance the development of helpful predictive models.

A significant amount of information to partially understand the observed behaviour in the activity tests was obtained through H_2-TPR (Hydrogen Temperature-Programmed Reduction) performed on all the catalysts. By measuring the hydrogen consumption at the reduction temperature corresponding to the reduction of the noble metal and assuming the metal is fully reduced, we could calculate the quantity of hydrogen that "spilled-over" onto the support. Spillover is a phenomenon observed in heterogeneous catalysis, where hydrogen molecules (H_2) dissociate on one part of a catalyst surface, typically the metal, and then migrate to another part of the surface, usually the support, where they participate in catalytic reduction of support oxide sites. On the other hand, even though the reduction of impurities cannot be excluded in advance to explain the negative peak at around 550°C on Rh/CeO_2 its absence on the other rhodium loaded samples H_2-TPR profiles suggests with a higher degree of confidence that part of the dissociated hydrogen may chemisorbed on the surface as it is shown in fig.5.7a, underlining the complexity of the phenomena.

However, assuming the general tendency of each sample to behave as the material intrinsic characteristics establish, the macroscopic observation of the % yield for each sample can be compared as an activity index, addressing whether the above-mentioned phenomena can impact on the catalytic behaviour.

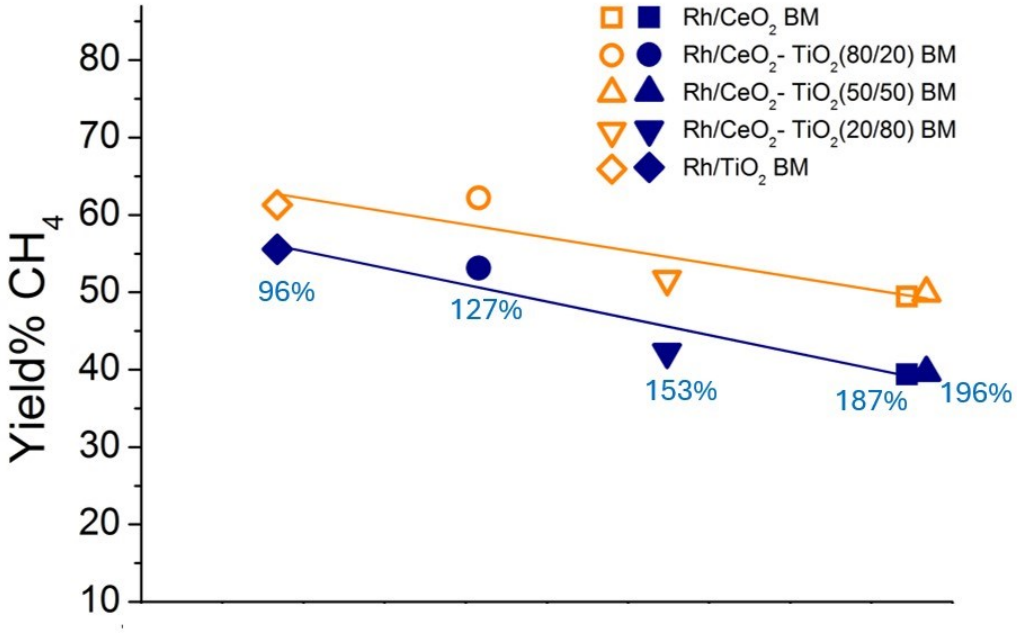

Fig. 6.3: Catalytic activity in terms of Yield% comparison between samples in both Light and Dark experimental conditions (empty and solid symbols respectively), for a set of catalyst metal loaded at 4%wt by Ball Milling, orange and blue solid lines represent the trend of light and dark experiments respectively; H_2 consumption % of H_2-TPR experiments in dark conditions.

The figure above illustrates an intriguing relationship between our experimental results and the percentage of hydrogen spilled onto the support. The graphical representation suggests an inverse proportionality, where higher performance corresponds to samples with lower spillover effects. As a result, support compositions of mixed ceria and titania demonstrate performance that lies between ceria (with the highest spillover) and titania (with the lowest spillover) pure oxide-supported catalysts. The impact of light in this correlation is expressed by the difference in terms of Yield ($Y_L - Y_B$), or graphically the distance between the blue and yellow segments, which seem to be higher with higher quantities of H_2 consumption. This indication, far from being a real comparison between samples in their red-ox potential in presence of light, on the other hand gave insights on how the material may behave in presence of a reactive atmosphere and light on the basis of literature indication and the experimental results.

In particular, the experimental results on the CeO_2 and TiO_2 pure oxide-supported catalysts, as well as the mixed oxides Ce:Ti 80:20, 50:50, and 20:80, confirm this trend. The Ce:Ti 80:20 catalyst, showing an intermediate spillover effect, exhibited one of the highest catalytic performances. This can be attributed to the optimized balance between spillover and the stabilization of key intermediate species facilitated by the mixed oxide composition. Conversely, Ce:Ti 50:50, despite exhibiting a higher spillover effect than Ce:Ti 80:20, demonstrated a lower performance, highlighting the nuanced role of spillover and its interaction with the catalytic mechanism.

Far from being a proof, a slight difference between the interpolation slopes drawn for the catalytic performance in dark and light conditions apparently suggested that possibly different coexisting and rather concurrent reaction mechanisms could be differently influenced by the spillover phenomena in presence of light, leading our attention on a deeper investigation of this intuition.

This indication was not intended as a direct comparison of the samples' redox potentials under illumination. Instead, it provided insights—based on both literature evidence and experimental observations—into how the materials might behave in a reactive atmosphere when exposed to light. Ideally, an assessment of the difference in hydrogen spillover between dark and illuminated conditions would have been desirable to clarify the influence of light on the process. However, due to instrumental limitations of H_2-TPR technique, it was not possible to directly obtain this information. For this reason, alternative analytical approaches were employed to infer the underlying mechanisms.

6.4 Experimental Hypothesis

To understand the role of spillover phenomenon and plasmonic effect on the methanation, it is essential to examine its mechanisms. Studies using in-operando DRIFT spectroscopy have provided crucial insights into the intermediate species and steps leading to methane formation. This methodology enables direct observation of surface species and their transformations during reaction conditions, bridging gaps in our understanding of catalytic processes [258, 259].

Mechanistically, CO_2 methanation proceeds via two primary pathways: the associative and dissociative mechanisms, each involving distinct steps and intermediates [233]:

Associative Mechanism (indirect pathway):

1) CO_2 adsorbs onto the support surface, forming intermediates such as bicarbonates or formates through reactions with hydroxyl groups on the support.
2) Formates are subsequently reduced through the reverse water-gas shift (RWGS) reaction, leading to the production of carbonyls on the metal surface. [264,265]
3) Hydrogen spillover from the metal to the support plays a pivotal role in these transformations, facilitating the reduction of formates and enhancing the formation of methane. This pathway is particularly significant on partially reducible oxides like ceria, which stabilize intermediates such as monodentate carbonates, enabling faster hydrogenation [47, 260].

Dissociative Mechanism (direct pathway):

1) CO_2 directly dissociates on the metal surface into adsorbed CO and oxygen atoms. This step is rate-limiting and relies on the catalytic metal's ability to break the C=O bond efficiently.

2) The adsorbed CO is hydrogenated to methane via sequential hydrogenation steps.
3) The dissociative pathway is more dominant on metallic rhodium sites and benefits less from the spillover effect compared to the associative pathway which is typical of not or poor reducible metal supported catalysts such as Rh/TiO_2 [261, 262, 263].

Recent investigations on Rh/CeO_2 systems further illuminate these mechanisms. Experiments have shown that the spillover rate is significantly influenced by the surface hydroxylation of the support. [258] In such catalysts H_2 spillover reduces the availability of adsorbed hydrogen on the metal surface, thereby slowing critical steps leading to methane production [264]. Additional studies on Rh/TiO_2 systems provide further insight on the possible effect of spillover on mechanism of hydrogenation of CO. For instance, it is reported that Hydrogen dissociates on Rh nanoparticles and spills over onto the TiO_2 support, protonating surface oxygen atoms and injecting electrons into the conduction band of the support. This process influences the behaviour of adsorbed CO species on metal, enhancing their density and compressing the CO adlayer, as evidenced by a blue shift of the Rh^0-CO absorption band. These changes highlight the role of hydrogen in altering the surface dynamics, promoting interactions between CO molecules, and impacting therefore their activation mechanism [259].

Both associative and dissociative routes may coexist especially in mixed oxide supported catalysts. The balance between these pathways is strongly influenced by the physical and chemical characteristics of the mixed oxide supports and the spillover phenomena may impact positively or negatively the methanation depending on the catalyst's compositions and the dominant mechanism.

The rate-determining step in CO_2 methanation, namely the formation of carbonyl species, is influenced by hydrogen spillover processes at the metal–support interface. In particular, spillover can affect the distribution and availability of hydrogen on the catalyst surface, thereby modulating the pathways and efficiency of methane formation. This relationship is supported by experimental observations showing that variations in spillover dynamics correlate with changes in catalytic performance [264, 265].

For example, in Rh/TiO_2 systems, hydrogen dissociation on Rh nanoparticles and subsequent migration onto the TiO_2 support can modify the support's electronic and surface properties, ultimately affecting the behaviour of adsorbed CO species [259]. Similarly, in Rh/CeO_2 catalysts, hydrogen spillover is associated with increased support reducibility and stabilization of key intermediates, as indicated by changes in magnetic susceptibility and conductivity [258].

Taken together, these findings highlight the complex interplay between hydrogen spillover, support properties, and the overall catalytic mechanism. A more detailed understanding of these interactions—

particularly as revealed by advanced surface-sensitive techniques such as DRIFT spectroscopy—will be discussed in the following sections.

To validate this hypothesis, FT-IR-DRIFT spectroscopy was employed under operando conditions. By introducing light stimuli during the experiments, it was also possible to observe how plasmonic effects influence the formation and consumption of intermediates. In particular, we focused on the formate species as a key target to demonstrate a direct effect of light on their kinetics of formation and reduction. This approach enabled the differentiation of thermal and plasmonic contributions, providing real-time evidence of the factors driving catalytic performance. The resulting data revealed a nuanced interplay between light-driven and thermally-driven mechanisms, offering deeper insights into the catalytic system's behaviour under varying conditions.

As previously mentioned, the potential connection between intermediate species on the catalyst surface and the observed differences in activity among the examined samples prompted us to formulate a hypothesis. This hypothesis suggests a direct correlation between the spillover effect and the formate route in the reaction mechanism. While samples with a higher percentage of spillover appear to be less active, a potentially higher content of formates could lead to poorer catalytic activity. Conversely, light appears to enhance performance, particularly for samples with a higher number of formate bonds. This suggests a direct effect of light on the reaction route and its kinetics, favoring samples with a "bigger reservoir" of formates.

In order to catch such specific and small signal intensity variations can be challenging with the in-operando DRIFT technique. Due to the peculiarity of the observations needed, a unique experimental setup was devised.

6.4.1 Experimental Setup

Previously explained aims lead to the definition of the experimental objectives:

i. Observe the evolution of the species adsorbed on the surface of the sample following exposure to the reaction atmosphere at a temperature of 50°C

ii. Observe the spectrum of the individual catalysts in the reaction atmosphere as the temperature varies between 150 and 250°C in the dark compared to a background detected on a pre-cleaned sample. Evaluate the composition of the reactant species found on the surface of the catalyst (carbonates, acid carbonates, formate, carbonyls, CO and adsorbed CO_2) and how these evolve with temperature.

iii. Observe, at various temperatures in the range 100-250°C, which species and how they evolve over time in Dark or Light conditions alternatively compared to a background detected in stationary conditions of temperature and reaction atmosphere

iv. Compare the response in light conditions with background in reaction atmosphere as the temperature varies for the single catalyst and between different catalysts for temperatures of 150-200-225-250°C, i.e. in the temperature range in which the methanation reaction begins to be thermodynamically favored.

A schematic representation of a typical experimet is proposed in the following figure:

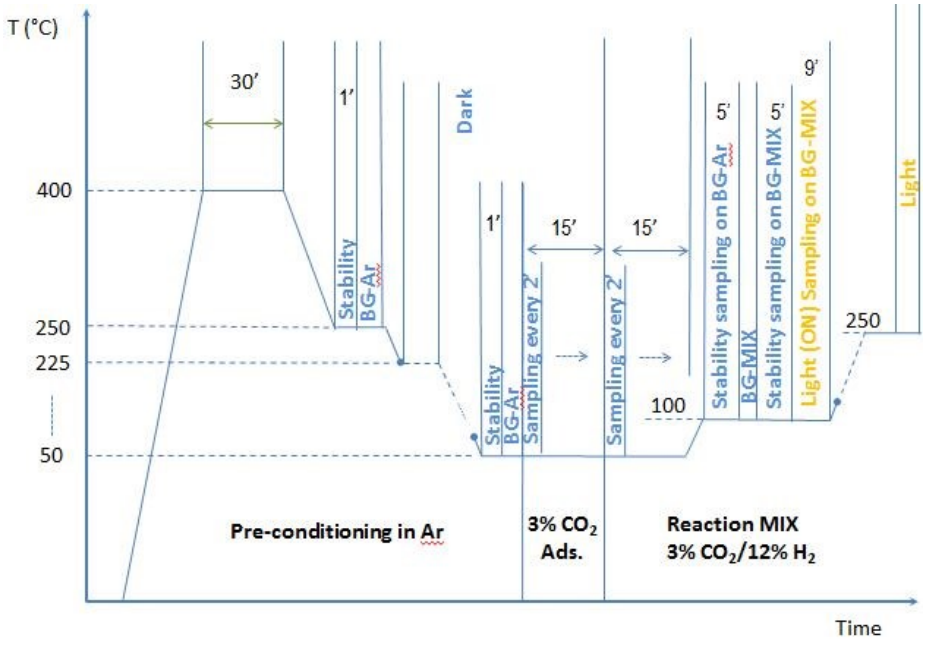

Fig. 6.4 Graphical representation of the whole FT-IR DRIFT in Dark/Light (Lamp ON/OFF) conditions experiment structure. The inert gas is Argon, and the total flow is constant 100ml/min, controlled by Mass Flow Controls and valves. A shutter is used to switch on/off the light.

Experiment description

After a pre-conditioning and cleaning treatment of the surface at 400°C with an inert gas atmosphere, the sample was than cooled in the same conditions. Background spectra in Argon atmosphere (BG-Ar) were collected for discrete values of temperature during cooling ramp in 250-50 °C interval, waiting for the system to stabilize before collection, usually within 1 minute. Subsequently, at the constant temperature of 50°, a 3% CO_2 gas mix was fed, sample was exposed for 15' and the adsorption of CO_2 was observed with spectra collected every 2' by using the afore collected background spectra (BG-Ar50). The exposition time was considered sufficient because the spectra was considered sufficiently stable almost immediately. After that 12% H_2 /3% CO_2/85% Ar gas mix was fed in, still in dark condition, so that we could observe the formation of those species supposed to be part of the reaction mechanism, together with the product gas. The reaction atmosphere exposition time was also 15' and in this case was considered sufficient because spectra reached stability within 9 minutes.

Then the temperature was raised to 100 °C and spectra were collected on BG-Ar100 until the the system was stable. After this a background could be collected in reaction atmosphere and named BG-MIX. New spectra were then collected using this new background for 5' and subsequently labelled as spectra taken in "dark" condition and used as a reference for comparison with those in "light" condition. The latter was achieved when the light beam shutter was open, and the sample irradiated; at the same time, the collection of the first spectra was started and then others collected for 9' every 2 minutes. The same procedure was repeated at 150-200-225-250 °C isotherms, results were eventually processed and analysed to produce the desired comparison and analysis that will be shown afterwards.

Methanation reaction - description of species:

For easy identification of the surface species on the spectra, the following scheme recalls the main surface species expected in CO_2 reduction reaction and trying to retrieve a clear indication of the reaction mechanism, together with the ranges of wavenumbers active in infrared.

			Wavenumbers (cm^{-1})			
Species			ν_{as}(CO)	ν_{as}(OCO)	ν_{s}(OCO)	Ref.
Carbonate:	m-CO_3		1470-1530	1300-1370	1040-1080	[266, 267, 268, 269]
	b-CO_3		1580-1700	1220-1290	980-1030	[266, 267]
	b-br-CO_3		1530-1710	1135		[269, 266, 270]
Bicarbonates			1610-1680	1400-1450	1200-1240	[268, 269]
Formate			ν_{as}(CH): 2900-3000	1550-1590	1330-1380	[271, 272, 269]
Rh-Carbonyl	L-CO(m-, di-, tri-)		2000-2090	-	-	[271, 273, 274]
	B-CO	Rh-C-Rh	1920-1990	-		[271, 273, 274]
		Ce-C-Rh	1720-1760	-		[274, 275]
	H-CO		1800-1890	-	-	[273, 274, 253]

Table 6. 1 Reference table of carbonaceous species typically adsorbate in a CO_2 reduction reaction and their FT-IR DRIFT stretching bands. Cabonates: Monodentate (m-), Bidentate (b-), Bidentate bridged (b-br-); Bicarbonates; Formate; Carbonyl species on Rh metal: Linear (mono, geminal or tri-carbonyl), Bridged, Hollow.

In the scheme above are reported the species which are formed on the support in presence of a reaction atmosphere, useful for a general indication, those wavenumber intervals may vary depending on several aspects depending by experimental conditions. The problem was studied in literature to understand if the peak position change may be caused by the actual frequency shift of a single absorption band or, alternatively, by the relative intensity changes of overlapped nearby bands, it results to be a well know problem when dealing with OH or C=O stretching. It was concluded that the correct interpretation is more likely to be that the shift is caused by a change in population of convoluted nearby stretching bands. [276]

Carbonate species are formed in presence of the only CO_2 gas phase which provides an intense double band at 2350 cm^{-1} together with two double bands localized between 3500−3750 cm^{-1}. On a pre-reduced surface, the presence of formate it is usually revealed when hydrogen gas is not already introduced. CH_4 reference band falls at 3015 - 1303 cm^{-1} [276].

Furthermore, when indications on the direct route are needed it is important to observe peaks of the species between 1720-2100 cm^{-1} which are attributed from literature to single linear or bridged CO bonding to reduced Rhodium vibrating with different modes and with different wavenumbers depending on the support used for rhodium metal, the size of particles and their dipole interactions. [277, 278].

CO adsorption on Mn, La, Ce, Fe promoted Rh/SiO_2 catalysts showed bands at wave numbers below 1790 cm^{-1} [279, 280, 274]. It was suggested that Lewis acid sites caused the downward shift of CO ligand wave number by the interaction of the Lewis acid with the oxygen atom of CO, the carbon atom of chemisorbed CO bonded to Rh atom and the oxygen tilted to the metal ion [279, 280, 274]. In our cases we are inclined to assign the band at about 1,740 cm^{-1} to such type of tilted CO which is bonded to the Rh and interacts with the oxygen vacancy of the support (lewis acid sites).

6.4.2 Experimental Data

The experimental setup described earlier was utilized to perform in-operando FT-IR DRIFT spectroscopy on all the samples previously tested in the experimental campaign. The primary goal of these experiments is to establish a correlation between the catalytic behaviour observed under Dark and Light conditions for the different samples, and to gather evidence regarding the global reaction mechanism, along with insights into the catalytic activity results from the earlier campaign.

Spectra were recorded after exposure of the samples to CO_2 and reaction atmosphere at 50°C. This initial identification of adsorbed species, such as carbonates, bicarbonates, and formates, provides insights into the reaction mechanisms. The investigation then advanced to reaction conditions under both dark and illuminated settings across a temperature range of 150°C to 250°C, with full activation of the reaction mechanism occurring at 250°C. By tracking the evolution of these species across the temperature range helps discern the impact of light on the reaction pathways and catalytic activity.

Soaking phase at 50°C samples comparison

CO_2 Adsorption:

The samples underwent the pre-conditioning Argon atmosphere at 400°C, as previously described in this chapter; this temperature was set because it can assure the degradation of any carbonate species on the catalyst surface prior to the exposition to reactants. Following the initial treatment, the samples were

subsequently cooled, collecting for a discrete number of temperatures a background spectrum on which, later after the exposition to reaction atmosphere, collect spectra for each of these isotherms.

Once cooled to 50°C and waited a stabilization time, the last background was collected and a stream of CO_2 gas was then supplied to the chamber and maintained for 15 minutes, collecting sample spectra every two minutes. The procedure described above was seemingly repeated for each catalyst; In the figure below are reported spectra at 15' of each catalyst considered solidly stable and comparable.

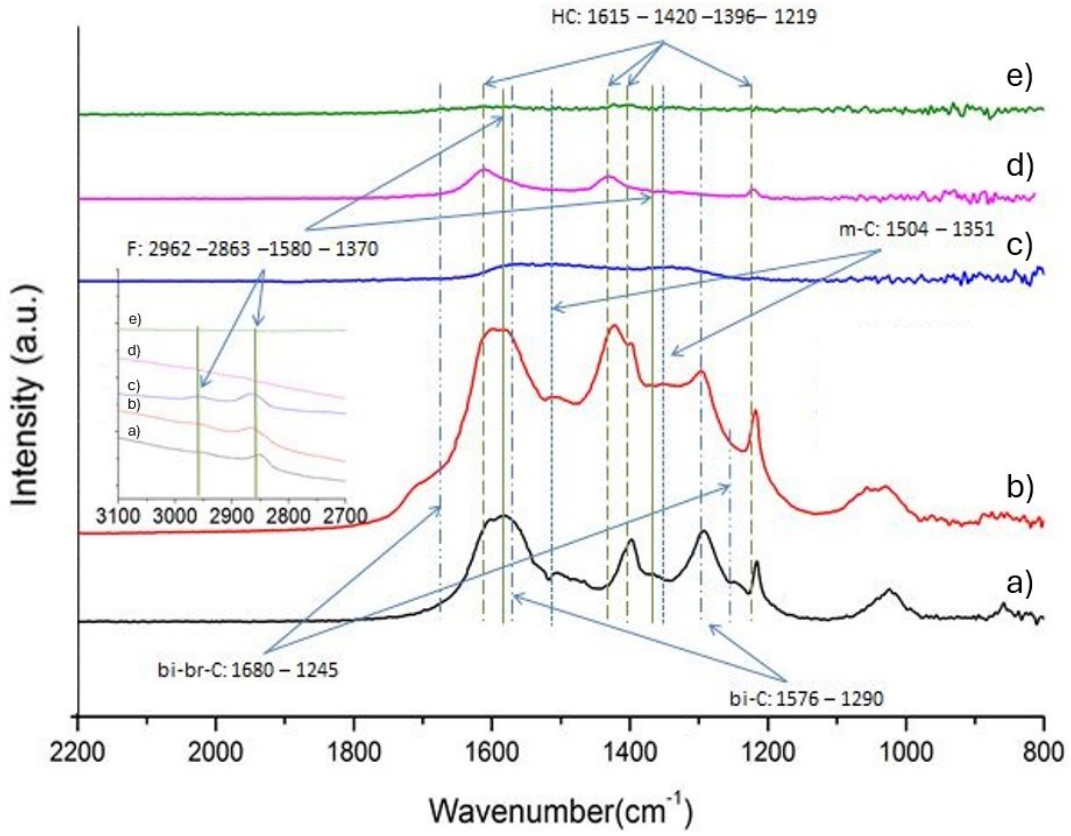

Fig. 6.5 illustrates DRIFT spectra of all catalyst samples collected in a 100ml/min 3% CO_2 .in Ar gas flow after 15 minutes of exposition at 50°C. Peaks of main species retrieved are reported, m-C: monodentate carbonate, bi-C: bidentate carbonate, bi-br-C: bidentate bridged carbonate, HC: hydrogen carbonate, F: formate. a) Rh/CeO_2, b) $Rh/Ce_{0.8}Ti_{0.2}O_2$, c) $Rh/Ce_{0.5}Ti_{0.5}O_2$, d) $Rh/Ce_{0.2}Ti_{0.8}O_2$, e) Rh/TiO_2

In these experimental conditions, spectra can result very different depending on the support material for the Rhodium metal nanoparticles. The presence and the abundance of carbonate species is undoubtedly linked to the CeO_2 amount in the mixed oxide.

Figure 6.5 illustrates the DRIFT spectra after 15 minutes of CO_2 exposure in a 3% CO_2/Ar gas flow. Peaks of the main identified species are as follows:

- **Monodentate carbonate (m-C):** Peaks at 1504 cm^{-1} and 1351 cm^{-1}
- **Bidentate carbonate (bi-C):** Peaks at 1576 cm^{-1} and 1290 cm^{-1}

- **Bidentate bridged carbonate (bi-br-C):** Distinct peaks at 1680 cm^{-1} and 1245 cm^{-1}
- **Hydrogen carbonate (HC):** Peaks at 1615 cm^{-1}, 1420 cm^{-1}, 1396 cm^{-1}, and 1219 cm^{-1}
- **Formate (F):** Peaks at 2962 cm^{-1} and 2863 cm^{-1}

The DRIFT spectra reveal notable differences based on the composition of the supports. For the Ce:Ti (50:50) sample, the bands corresponding to carbonates are broad and overlap significantly, reflecting a complex surface environment. This observation is consistent with BET analyses, which suggest a mesoporous structure with high heterogeneity [270]. In contrast, the Ce:Ti (80:20) sample displays sharper peaks, particularly for the bidentate bridged carbonate species at 1680 cm^{-1} and 1245 cm^{-1}. These features indicate a unique coordination environment, likely influenced by CeO_2's reducibility and the presence of oxygen vacancies, further supported by the pronounced shoulder at 1700-1680 cm^{-1}, attributed to the C–O stretch of CO_3^{-2} in a specific configuration. [281, 282]

Predominantly TiO_2-supported samples, on the other hand, exhibit a prevalence of hydrogen carbonate species, identified by peaks at 1615 cm^{-1}, 1420 cm^{-1}, 1396 cm^{-1}, and 1219 cm^{-1}. These findings align with the reduced surface area and lower oxygen vacancy density typical of TiO_2, which impacts its ability to stabilize carbonates [283].

The spectral profile of Ce:Ti (80:20) reflects its predominantly CeO_2-based surface, which is enriched with oxygen vacancies resulting from TiO_2 interaction. This unique structure enhances CO_2 adsorption and activation, aligning with experimental results that demonstrate the highest CO_2 activation rates for this composition [267].

The observed differences in the spectral profiles can be attributed to several interconnected factors. The coordination environment plays a fundamental role in influencing the spectral behaviour. Lower oxidation states, such as Ce^{3+}, enhance the strength of metal-carbonate bonds, leading to increased vibrational frequencies. This effect is particularly evident in Ce:Ti (80:20), where the higher reducibility of CeO_2 promotes the presence of Ce^{3+}, contributing to stronger carbonate binding and distinct vibrational modes [282].

Moreover, the interactions between CeO_2 and TiO_2 significantly modify the oxygen vacancy distribution. These interactions stabilize specific carbonate species, as highlighted by the sharper peaks observed for bidentate carbonate species in Ce:Ti (80:20). The interaction shifts vibrational frequencies, which is consistent with the unique surface chemistry of mixed oxides [281].

Finally, the surface characteristics of TiO_2-rich samples explain their spectral differences. The lower reducibility of TiO_2 results in weaker carbonate binding, favouring bicarbonate formation. This is reflected in

the prevalence of hydrogen carbonate peaks, particularly at 1615 cm^{-1}, 1420 cm^{-1}, 1396 cm^{-1}, and 1219 cm^{-1}, which are characteristic of TiO_2-dominated surfaces [267].

Gas MIX Adsorption

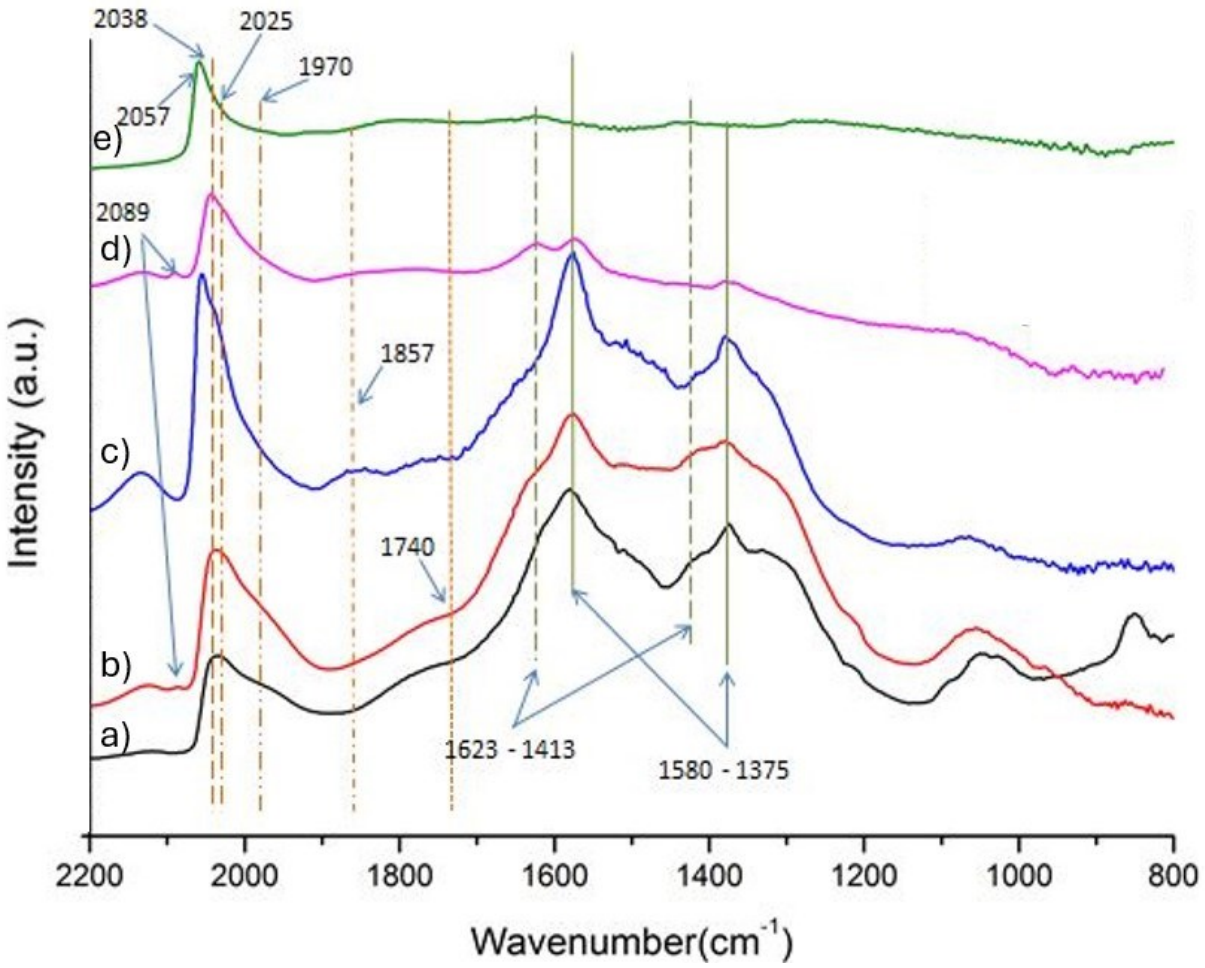

Fig. 6.6 Displays the Kubelka-Munk function of the DRIFT spectra collected for all sample at 50°C, with a flow rate of 100 ml/min comprising 12% H_2, 3% CO_2, and 85% Ar in the reaction atmosphere (MIX), with the lamp switched off. a) Rh/CeO_2, b) $Rh/Ce_{0.8}Ti_{0.2}O_2$, c) $Rh/Ce_{0.5}Ti_{0.5}O_2$, d) $Rh/Ce_{0.2}Ti_{0.8}O_2$, e) Rh/TiO_2

After CO_2 adsorption, in the same temperature condition (50°C), the introduction of hydrogen gas set a new surface composition of adsorbates. In Figure 6.6, the spectra collected on our set of samples in the reaction MIX atmosphere are plotted within the same wavenumber interval discussed earlier. Several differences are evident, particularly in the carbonates' region. The spectra are more intense for ceria-containing samples, suggesting that the reducing agent activates Rh metal active sites. This activation, supported by H_2-TPR experimental evidence, induces spillover on the support, forming hydroxyl groups on Ce^{3+} sites and significantly enhancing CO_2 adsorption.

Analysing differences among the samples, the (80:20)-Rh sample stands out, exhibiting the most intense signals for all carbonate species. This observation aligns with a Gaussian trend as TiO_2 doping increases.

Notably, this sample shows an abundance of hydrogen carbonates (1623–1413 cm^{-1}) and formate (1580–1375 cm^{-1}). Additionally, monodentate carbonate species (1520–1460 cm^{-1}) are particularly prominent, creating a plateau-like appearance in this spectral interval. Reduction of monodentate carbonate on Ce^{3+} sites directly form monodentate formate, facilitating a faster reduction pathway to methane [284]. This could explain the superior performance of this sample compared to others, except for the comparable performance of TiO_2-Rh. The latter's efficiency is attributed to its low spillover effect, enhancing the dissociative and direct reaction route. Conversely, (80:20)-Rh seems to overcome this limitation with an efficient indirect pathway.

In the >1700 cm^{-1} range, the 1740 cm^{-1} peak corresponds to Rh-Ce^{3+} bridged carbonyl species [274]. Ceria's defects are sufficiently close to active sites to catalyze reduction reactions but may inhibit methane formation if active sites are occupied. This highlights the importance of the metal-support interface and the support's structure in determining performance, as well as the metal's oxidation state [285, 286].

In the 1800–2100 cm^{-1} range, peaks associated with ν_{nh}(CO) of carbonyl species on rhodium are observed. The 1857 cm^{-1} peak is attributed to two-fold bridged carbonyl species, while the 1970 cm^{-1} peak corresponds to asymmetric stretches of bridged carbonyls. The formation of these bridged carbonyls decreases with increasing TiO_2 content, which predominantly exhibits linearly bonded carbonyls. Bridged carbonyl formation is favoured when metal atoms are closely spaced, allowing CO molecule sharing. Supports that aggregate metal clusters facilitate this formation, while those dispersing rhodium atoms inhibit. Bridged carbonyls stabilize clusters via electron density delocalization but reduce electron donation from CO, impacting reactivity [287].

In the 2000–2090 cm^{-1} range, mono-, di-, and tri-carbonyl structures appear, influenced by the oxidation state of the metal-support interaction. The 2090 cm^{-1} mono-carbonyl species is prominent in (80:20)-Rh and (20:80)-Rh, likely due to the mixed oxide composition. Terminal linear carbonyl bonds (2057 cm^{-1}) on titania-supported rhodium overlap with those on ceria, particularly in the (50:50)-Rh sample, suggesting some distribution of specific active sites influenced by the nearby support.

CO adsorbed on Ce^{3+} sites or oxygen vacancies is identified by the 2140 cm^{-1} peak [277]. This species, absent in TiO_2-Rh, is observed in ceria-containing samples, with a bell-shaped trend peaking at (50:50)-Rh. This indicates that ceria-titania lattice interactions influence the distribution of reduced sites and oxygen vacancies. However, the (50:50)-Rh sample performs poorly despite having active sites due to slower, less selective methanation pathways, which become rate-determining. Spillover effects and increased metal-support interaction with higher TiO_2 content, as seen in H_2-TPR data, may indicate that CO binding to the support reduces its availability on the metal, limiting catalytic activity.

In conclusion we can summarize, comparing those observation with catalytic performance that Titania supported sample is particularly efficient in methanation reaction following the direct pathway which is faster

nonetheless limited by the presence of intermediate products caused by spillover effect and involved in the indirect pathway in presence of Ceria in the mixed oxide and with increasing reduced active sites on the support. The optimum seem to be found with Ce:Ti (80:20) composition for which a peculiar equilibrium between this competing reaction mechanisms has been found.

Dark and Light in reaction condition:

For each isotherm step, a new background was acquired, and spectra were collected every 2 minutes to establish a dark condition reference, then compared with those acquired under light conditions. This technique is particularly useful for understanding the impact of light on reaction species, with the explicit purpose of identifying how the reaction mechanism may be enhanced by photo-induced activity.

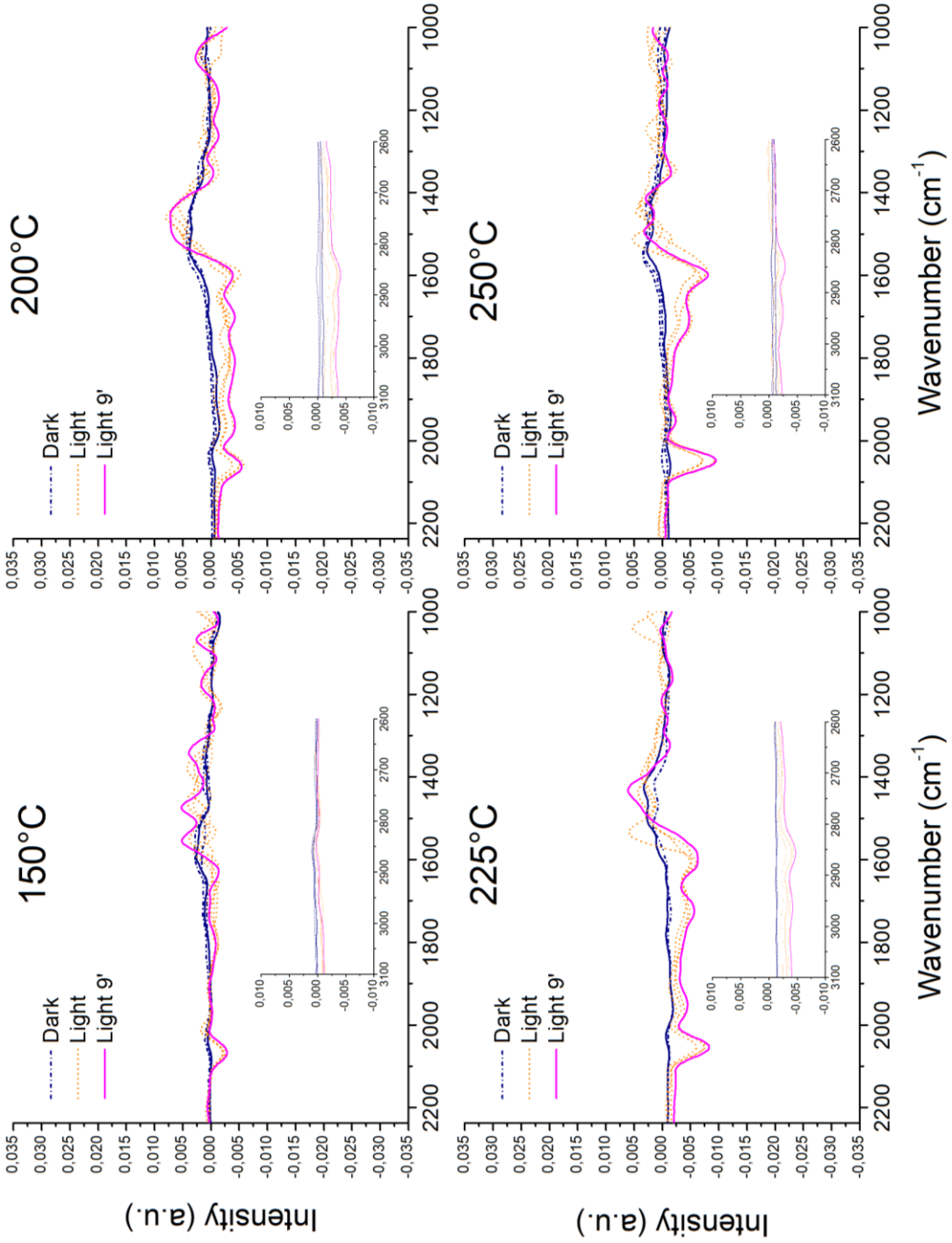

Fig. 6.7a Displays CeO_2-Rh Kubelka-Munk function of the DRIFT spectra, in the interval 2300-1000 cm^{-1} collected at 150-200-225-250°C on BG-MIX, with a flow rate of 100 ml/min comprising 12% H_2, 3% CO_2, and 85% Ar in the reaction atmosphere (MIX), with the lamp switched off (blue solid line) and on(yellow(dash)/purple(solid) line) .

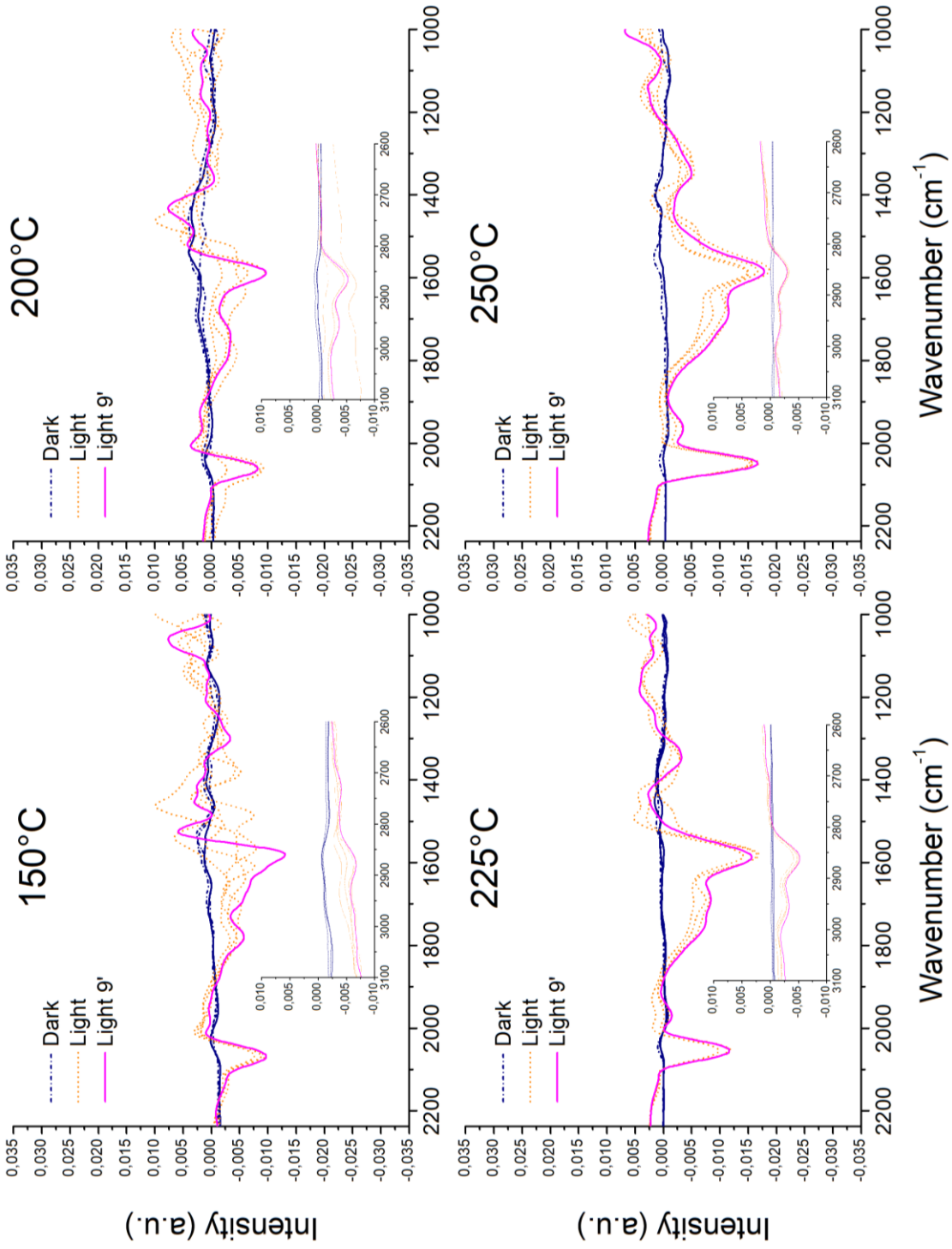

Fig. 6.7b Displays CeO_2:TiO_2(80:20)-Rh Kubelka-Munk function of the DRIFT spectra, in the interval 2300-1000 cm^{-1} collected at 150-200-225-250°C on BG-MIX, with a flow rate of 100 ml/min comprising 12% H2, 3% CO2, and 85% Ar in the reaction atmosphere (MIX), with the lamp switched off (blue solid line) and on(yellow(dash)/purple(solid) line) .

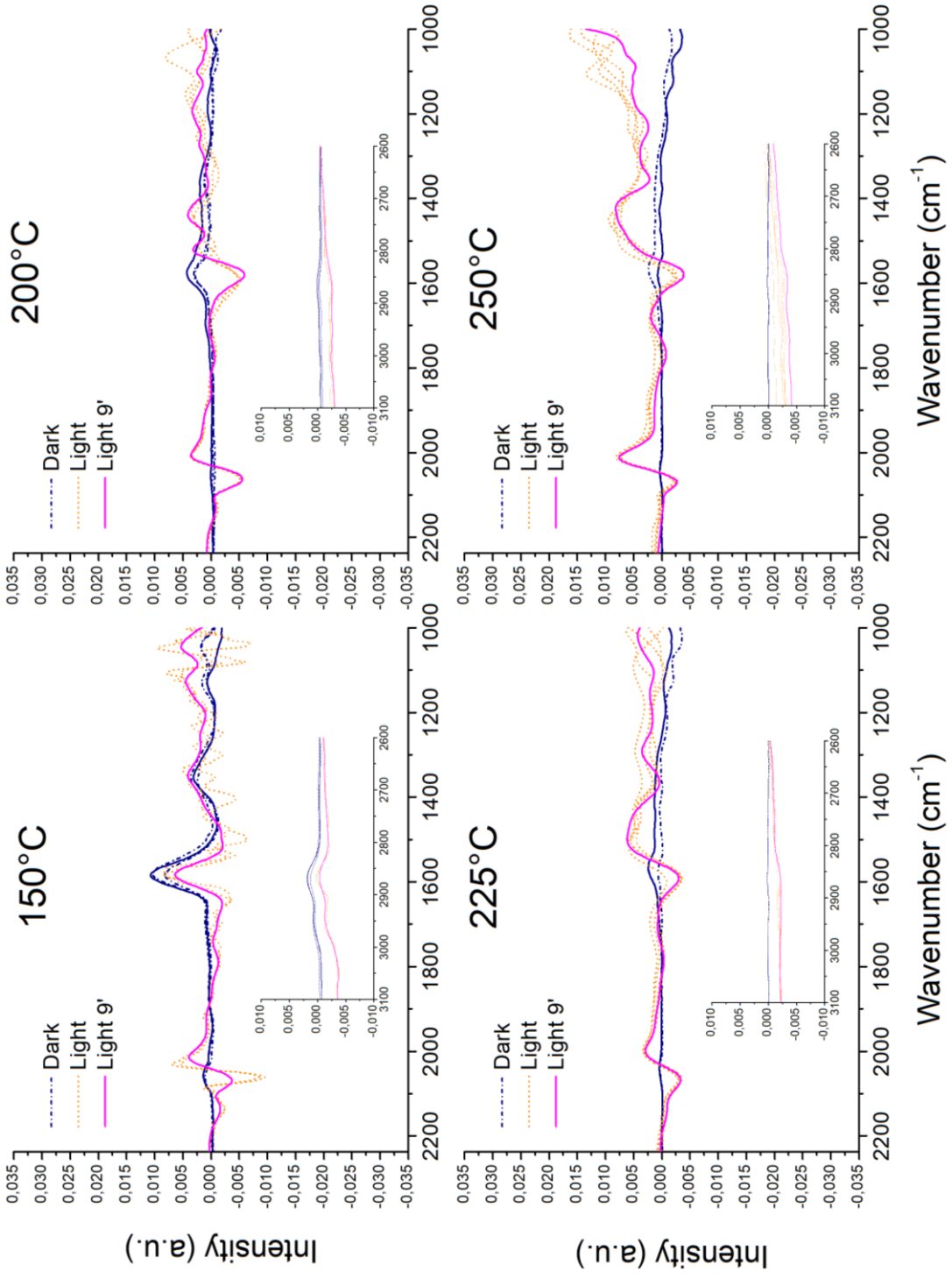

Fig. 6.7c Displays CeO_2:TiO_2(50:50)-Rh Kubelka-Munk function of the DRIFT spectra, in the interval 2300-1000 cm^{-1} collected at 150-200-225-250°C on BG-MIX, with a flow rate of 100 ml/min comprising 12% H_2, 3% CO_2, and 85% Ar in the reaction atmosphere (MIX), with the lamp switched off (blue solid line) and on(yellow(dash)/purple(solid) line) .

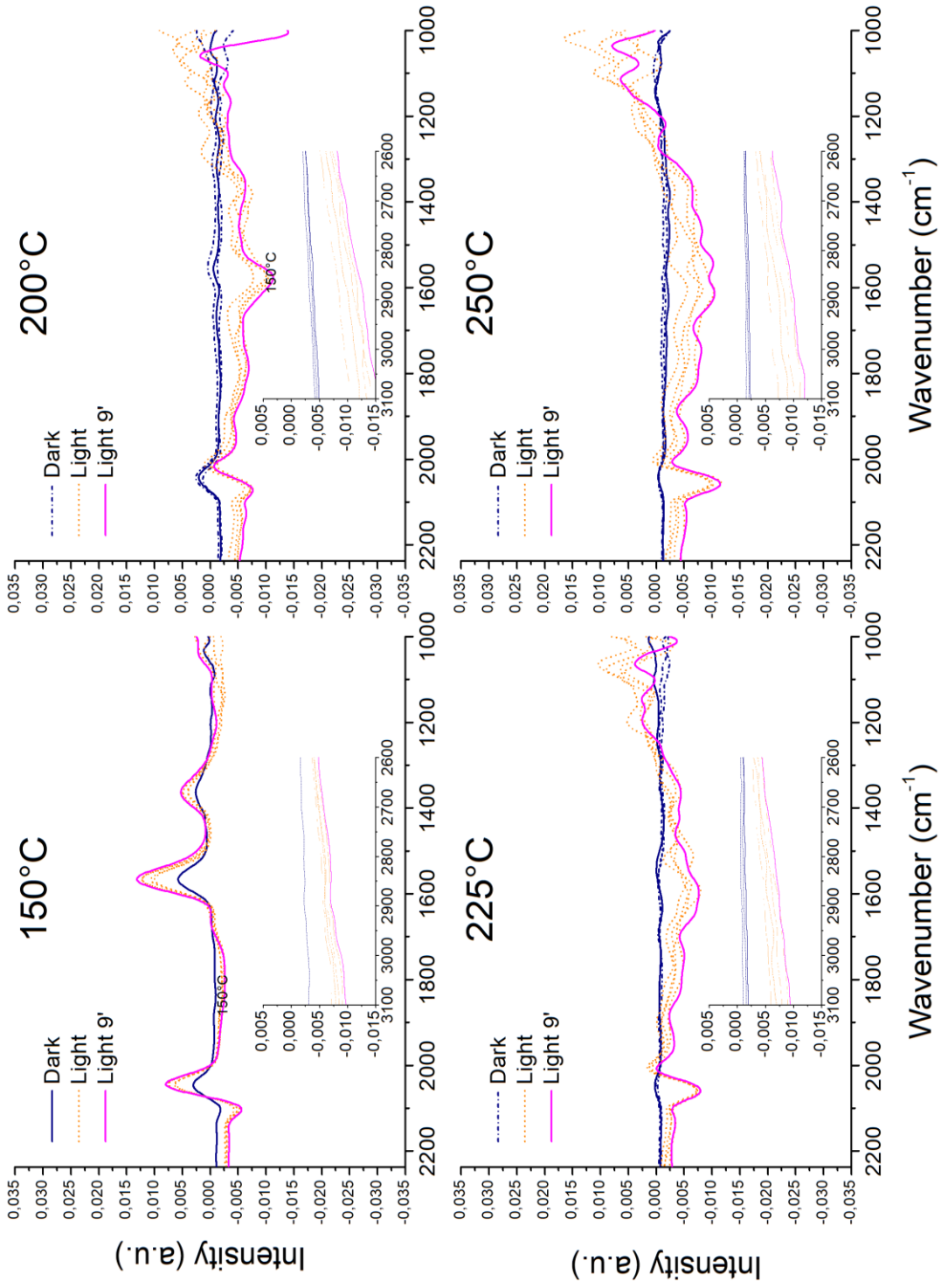

Fig. 6.7d Displays CeO_2:TiO_2(20:80)-Rh Kubelka-Munk function of the DRIFT spectra, in the interval 2300-1000 cm^{-1} collected at 150-200-225-250°C on BG-MIX, with a flow rate of 100 ml/min comprising 12% H_2, 3% CO_2, and 85% Ar in the reaction atmosphere (MIX), with the lamp switched off (blue solid line) and on(yellow(dash)/purple(solid) line) .

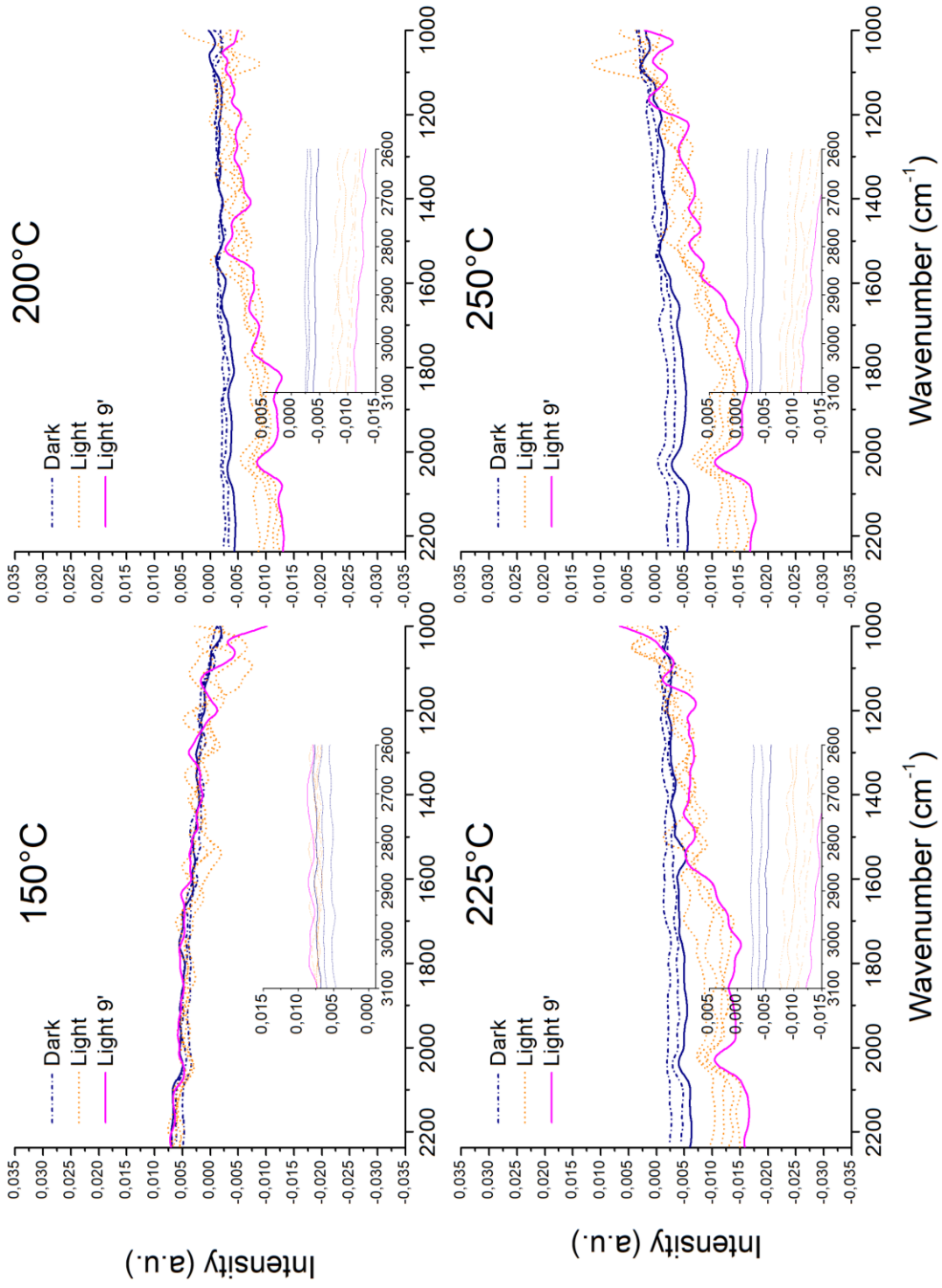

Fig. 6.7a Displays TiO_2-Rh Kubelka-Munk function of the DRIFT spectra, in the interval 2300-1000 cm^{-1} collected at 150-200-225-250°C on BG-MIX, with a flow rate of 100 ml/min comprising 12% H_2, 3% CO_2, and 85% Ar in the reaction atmosphere (MIX), with the lamp switched off (blue solid line) and on(yellow(dash)/purple(solid) line) .

Figures 6.7a-e illustrate the evolution of catalyst surfaces with temperature and the comparison between spectra collected under light and dark conditions. In blue, the spectra represent the dark condition at stability, while the yellow dashed lines show the spectra during the 5 minutes following lamp activation, and the purple solid lines indicate the stable light condition. Figure 6.7a presents the CeO_2-Rh sample experiment. At 150°C, differences between light and dark conditions are minimal, with peaks indicating an increased presence of carbonate species such as mono- and bidentate carbonates, as well as formates. However, for wavenumbers >1600 cm^{-1}, bicarbonates and rhodium carbonyl species decrease. At this temperature, the methanation reaction is not thermodynamically favored, resulting in minimal product formation.

As the temperature increases, the conversion rate rises, correlating with the disappearance of formates under light conditions at higher temperatures. This highlights the role of formates in the associative reaction mechanism, particularly for ceria-containing samples. The selective reduction of formates, compared to other species like carbonates, is indicative of their role in the reaction pathway. These findings align with H_2-TPR data, which demonstrated enhanced reducibility for ceria-containing supports showing surface reduction temperature peak is coherent with the plateau of performance (350°C).

In the TiO_2-Rh sample experiment (Fig. 6.7e), the presence of light does not produce significant changes in species, except for Rh carbonyl species and minor changes in the carbonate interval (1700–1200 cm^{-1}), which increase but remain stable at all temperatures. Notably, the intensity of spectra for this sample is an order of magnitude lower than for all other samples, this addresses a high IR absorbance of the catalyst that has been correlated to the formation of reduced titania species TiO_{2-x} and even higher in presence of reducing metal species, affecting the optical pathlength of the IR [288]. The most visible effect of light is a reduction in overall spectral intensity compared to the dark condition. This effect, likely observed when reactor temperature is ramped up, suggests a photothermal reduction effect, causing localized temperature increases and resulting in the observed spectral distortions. Hot-electron injection appears negligible for this sample, supporting the photothermal hypothesis, suggesting the thermally activated dissociative reaction route to be predominant compared to other light driven mechanisms.

What is noteworthy is the behaviour of mixed oxide compositions (Figs. 6.7b-d), reflecting tangible differences due to reciprocal doping of the oxides, which alters the environment where Rh metal active sites catalyze reactions. The selectivity of ceria-containing samples for species involved in the indirect methanation pathway suggests that the abundance of formate and bicarbonate, along with their selective reduction, contributes to the observed increase in methane yield under light conditions. This enhancement is significantly greater than that of the TiO_2-Rh sample. This conclusion is supported by BET and H_2-TPR characterizations, which demonstrate that mixed oxides provide an optimal environment for enhanced reducibility and active site dispersion.

This behaviour may be attributed to hot-electron injection, as discussed in Chapter 4. Although not evaluated optically, the macroscopic evidence suggests a quantum phenomenon in this complex reaction system. DRS experiments, the low band gap of defected ceria supports, and the intimate contact at the metal-support interface further support this hypothesis, as revealed by characterization experiments. The data align with evidence of a strong metal-support interaction (SMSI) observed for these systems, which facilitates charge transfer and enhances catalytic performance.

In this context, the Quantum-Spillover effect on these supports has been studied and demonstrated [289, 136]. The Quantum-Spillover mechanism involves the excitation of localized surface plasmon resonances (LSPR) on the Rh metal particles under light irradiation. These resonances decay into highly energetic electrons, or "hot electrons," which transfer into the support material. This transfer process selectively activates surface species, such as bicarbonates and formates, while facilitating the reduction of carbonyl intermediates. Notably, this mechanism not only increases the reaction rate but also enhances the selectivity of catalytic pathways by enabling transient occupation of antibonding states of adsorbed molecules.

Experimental data from in-operando DRIFT confirm this phenomenon, with mixed oxides demonstrating optimal reducibility and enhanced dispersion of active sites. Furthermore, plasmon-induced charge transfer across the metal-support interface, facilitated by the intimate contact between Rh and the oxide matrix, emerges as a crucial factor. This interface enables the efficient stabilization and utilization of hot electrons, extending their lifetimes and maximizing catalytic efficiency.

While the photothermal contribution cannot be neglected, particularly for TiO_2-Rh samples where hot-electron injection appears minimal, the Quantum-Spillover effect dominates in ceria-containing compositions. This is evident from their superior performance under light conditions, driven by the plasmon-mediated activation of reaction intermediates. This sophisticated interplay of plasmonic excitation and catalytic chemistry underscores the transformative potential of LSPR in designing advanced photocatalytic systems.

7 Conclusions

This study marks a significant milestone as the first approach of our research group to the innovative and interdisciplinary field of thermo-photo catalysis. Venturing into uncharted territory, this work required building knowledge and methodologies from scratch, overcoming numerous challenges along the way, and laying a solid foundation for future research in this domain. Here, we reflect on the journey, highlight the accomplishments, and identify areas of potential growth.

Historical Context and Motivation

The valorization of CO_2 through hydrogenation is a promising solution to address the dual challenges of climate change and energy sustainability. However, the integration of thermal and photocatalytic processes to enhance catalytic efficiency represents a novel frontier. For our group, embarking on this path meant addressing the fundamental question of how to synergistically combine thermal and photonic contributions to optimize catalytic performance. The field itself, offered limited established methodologies, further emphasizing the pioneering nature of this research.

From its inception, the project was driven by the vision of developing catalysts capable of utilizing renewable energy sources efficiently. The selection of rhodium-based catalysts supported on cerium-titanium mixed oxides, particularly the $Ce_{0.8}Ti_{0.2}O_2$ composition, was informed by an extensive review of literature and exploratory experiments, culminating in a material that showcased remarkable catalytic properties.

Overcoming Initial Challenges

The lack of prior expertise in thermophotocatalysis within our group necessitated a multifaceted approach to problem-solving. Key challenges included designing a reaction system that could effectively distinguish between thermal and photonic contributions, synthesizing and characterizing novel materials, and validating experimental protocols to ensure reproducibility and reliability.

Building the reaction test bench was a critical milestone. This bespoke system incorporated features such as precise temperature control, flexible gas feed configurations, and a solar simulator for photonic stimulation, enabling rigorous evaluation of catalytic activity. The development of this apparatus itself was a testament to the collaborative effort and ingenuity of the team.

Key Achievements and Insights

1. *Material Development and Characterization:*

   A comprehensive investigation was conducted on the complete series of pure and mixed cerium-titanium oxides. BET analysis yielded quantitative insights into surface area and porosity, demonstrating that the mixed oxides generally exhibited higher degrees of mesoporosity compared to their pure counterparts, with $Ce_{0.8}Ti_{0.2}O_2$ emerging as the most promising composition.

   X-ray diffraction (XRD) analysis confirmed that the fluorite structure characteristic of ceria is retained up to the $Ce_{0.5}Ti_{0.5}O_2$ composition. In contrast, the diffractogram of $Ce_{0.8}Ti_{0.2}O_2$ revealed the formation of a predominantly amorphous material, while pure titania exhibited the expected anatase and rutile crystalline phases.

   Temperature-programmed reduction with hydrogen (H_2-TPR) provided critical insights into the reducibility of the supports. Ceria-rich compositions displayed a higher density of oxygen vacancies and greater overall reducibility relative to titania-dominated systems. This enhanced reducibility was found to promote stronger metal-support interactions, particularly in catalysts synthesized via the Ball Milling (BM) method.

   Diffuse reflectance infrared Fourier transform (DRIFT) spectroscopy identified key surface species, including monodentate and bidentate carbonates as well as formates, which are believed to play a pivotal role in the reaction mechanisms.

2. *Photonic Contributions:*

   Diffuse reflectance spectroscopy (DRS) provided further evidence of a reduction in band gap energy across the series of mixed oxides, with $Ce_{0.8}Ti_{0.2}O_2$ exhibiting a value of approximately 2.6 eV. This narrowing of the band gap was found to enhance the absorption of visible light, thus improving the material's light-harvesting capabilities. In addition, the presence of oxygen vacancies contributed to further enhancement of light absorption and facilitated improved charge carrier mobility, both of which are considered critical factors underpinning the superior photocatalytic performance observed.

   Furthermore, experimental results highlighted the significant role of localized surface plasmon resonance (LSPR) effects associated with rhodium nanoparticles. Under illumination, these plasmonic effects were shown to markedly accelerate methane production, emphasizing the importance of nanoparticle-driven light-matter interactions in boosting photocatalytic activity.

3. *Catalytic Performance:*

This study has shown that the catalytic performance of Rh-based systems is strongly dependent on the nature of the oxide support, with light irradiation playing a decisive role in determining activity trends. Specifically, in dark conditions, Rh/TiO_2 exhibited higher CO_2 methanation activity compared to Rh/Ce:Ti(80:20) (see Section 6.2, Fig. 6.2), highlighting the intrinsic reactivity of titania as a support. However, upon illumination, the Ce:Ti(80:20) catalyst surpassed all others, showing up to a 35% increase in CO_2 conversion, and outperforming Rh/TiO_2 under identical conditions. This remarkable switch in activity is attributed to the coexistence of direct (plasmon-induced) and indirect (defect mediated) mechanisms in the mixed oxide system.

In Rh/TiO_2, light activation leads predominantly to a direct effect—plasmonic excitation of Rh—which enhances catalytic activity to a certain extent. In contrast, the presence of ceria in the mixed support introduces a high density of oxygen vacancies, as evidenced by TPR and DRS analyses (Sections 5.2, 5.4, Figs. 5.16–5.18), which act as active sites for hydrogen spillover and charge transfer. Under illumination, these defects facilitate the indirect (defect-driven) activation pathway, accelerating the rate-limiting steps of the reaction, and leading to a synergistic enhancement where both direct and indirect mechanisms contribute to the overall reactivity. This is further confirmed by FT-IR DRIFT experiments (Section 6.3, Fig. 6.5–6.7), which show a marked increase in the formation and reactivity of key intermediate species on Ce:Ti(80:20) under light.

These findings underline the importance of engineering both the metal and support properties to maximize the synergy between plasmonic effects and defect chemistry, and offer a clear mechanistic rationale for the superior photocatalytic performance of Rh/Ce:Ti(80:20) compared to either Rh/TiO_2 or Rh/CeO_2 alone.

4. *Comparison of Functionalization Methods:*

The catalysts were synthesized using two primary methods: Ball Milling (BM) and Incipient Wetness Impregnation (IW). Experimental data highlighted the superior performance of the BM method, particularly in catalysts containing ceria. BM facilitated stronger metal-support interactions, promoting better dispersion and stabilization of rhodium nanoparticles, which directly correlated with enhanced catalytic activity and stability. In contrast, IW, while offering precise control over nanoparticle size distribution, often exhibited agglomeration issues, particularly in ceria-rich supports, which negatively impacted catalytic performance. These findings underscore the critical role of synthesis methodology in tailoring catalyst properties and achieving optimal performance.

5. *Validation of Methodologies:*

The experimental approach adopted in this work, based on the integration of complementary characterization techniques (such as TPR, DRS, FT-IR DRIFT, and catalytic testing under both dark and illuminated conditions), has enabled a coherent interpretation of the observed catalytic phenomena. The cross-comparison of independent datasets—linking, for example, reducibility trends from TPR with light-induced effects seen in DRS and the evolution of surface intermediates identified by DRIFT—provided a consistent framework for understanding the mechanistic aspects of thermo-photocatalytic CO_2 methanation.

Nonetheless, it is important to acknowledge that the methodology, while robust and effective within the scope of this study, still leaves room for improvements in both experimental rigor and the breadth of validation. For instance, further refinements could include more advanced in situ or operando techniques, statistical analysis across a wider set of samples, and expanded testing under industrially relevant conditions. Future research should therefore aim to consolidate and extend this methodological framework, ensuring even greater reliability and generalizability of the findings.

Limitations and Lessons Learned

As with any pioneering work, this study faced limitations that offer valuable lessons for future research. The uniform distribution of rhodium nanoparticles remained a challenge, with preliminary TEM analyses indicating areas of agglomeration. Developing advanced synthesis methods, such as atomic layer deposition, could address this issue. Furthermore, distinguishing between photothermal and purely photonic effects requires more sophisticated analytical techniques, such as ultrafast spectroscopy. Additionally, the long-term stability of the catalysts under industrially relevant cyclic conditions needs to be thoroughly evaluated, particularly to assess potential degradation of both the support and the metal under prolonged illumination and thermal cycling.

Perspectives for Future Research

Looking ahead, this work lays the groundwork for exploring new frontiers in thermophotocatalysis. Future efforts could focus on:

- Material Innovations: Doping cerium-titanium supports with elements like tantalum or niobium to further enhance optical and catalytic properties.
- Synthesis Techniques: Employing advanced methods, such as hydrothermal synthesis or ball milling optimization, to achieve better control over material properties.
- Hybrid Systems: Integrating photocatalysis with technologies like photoelectrochemical cells to develop hybrid systems with higher energy efficiency.

- Industrial Applications: Scaling up the processes and testing catalyst stability under real-world conditions to bridge the gap between laboratory research and practical implementation.

Closing Reflections

Beyond a technical achievement, this study marks a milestone in our group's evolution, underscoring the promise of thermo-photo catalysis for addressing energy and environmental challenges—even as technical issues remain. One crucial aspect is the identification of appropriate analytical techniques for studying the various mechanisms contributing to the phenomenon and for distinguishing them from purely thermal catalytic effects. An effective strategy is to begin with simple, well-understood systems, postponing the analysis of more complex ones until a solid understanding of the underlying phenomena is achieved. We recommend starting with systems and reactions that are thoroughly described in the literature. With these principles in mind, we now plan to investigate plasmonic phenomena in more challenging processes, such as the reverse water-gas shift reaction and, more ambitiously, the co-reduction of CO_2 and H_2O for sustainable chemical and fuel production.

Bibliography

[1] . Feely, R. A., Sabine, C. L., Lee, K., Berelson, W., Kleypas, J., Fabry, V. J., & Millero, F. J. (2004). Impact of anthropogenic CO2 on the CaCO3 system in the oceans. Science, 305(5682), 362-366.

[2] . Sun, Z., Hu, Y., Zhou, D., Sun, M., Wang, S., & Chen, W. (2021). Factors influencing the performance of copper-bearing catalysts in the CO2 reduction system. ACS Energy Letters, 6(11), 3992-4022.

[3] . Kothandaraman, J., Goeppert, A., Czaun, M., Olah, G. A., & Prakash, G. S. (2016). CO 2 capture by amines in aqueous media and its subsequent conversion to formate with reusable ruthenium and iron catalysts. Green chemistry, 18(21), 5831-5838.

[4] . Rahman, A. (2010). Catalytic hydrogenation of acetone to isopropanol: an environmentally benign approach. Bulletin of Chemical Reaction Engineering & Catalysis, 5(2), 113-126.

[5] . Wang, C., Xie, Z., deKrafft, K. E., & Lin, W. (2011). Doping metal–organic frameworks for water oxidation, carbon dioxide reduction, and organic photocatalysis. Journal of the American Chemical Society, 133(34), 13445-13454.

[6] . Xu, H. Q., Hu, J., Wang, D., Li, Z., Zhang, Q., Luo, Y., ... & Jiang, H. L. (2015). Visible-light photoreduction of CO2 in a metal–organic framework: boosting electron–hole separation via electron trap states. Journal of the American Chemical Society, 137(42), 13440-13443.

[7] . Tranchemontagne, D. J., Mendoza-Cortés, J. L., O'keeffe, M., & Yaghi, O. M. (2009). Secondary building units, nets and bonding in the chemistry of metal–organic frameworks. Chemical Society Reviews, 38(5), 1257-1283.

[8] . Ding, M., & Jiang, H. L. (2018). Incorporation of imidazolium-based poly (ionic liquid) s into a metal–organic framework for CO2 capture and conversion. ACS Catalysis, 8(4), 3194-3201.

[9] . Modak, A., Nandi, M., Mondal, J., & Bhaumik, A. (2012). Porphyrin based porous organic polymers: novel synthetic strategy and exceptionally high CO 2 adsorption capacity. Chemical Communications, 48(2), 248-250.

[10] . Zhong, H., Su, Y., Chen, X., Li, X., & Wang, R. (2017). Imidazolium-and triazine-based porous organic polymers for heterogeneous catalytic conversion of CO2 into cyclic carbonates. ChemSusChem, 10(24), 4855-4863.

[11] . Hao, G. P., Li, W. C., Qian, D., & Lu, A. H. (2010). Rapid synthesis of nitrogen-doped porous carbon monolith for CO2 capture. Advanced materials, 22(7), 853-857.

[12] . Dutta, S., Bhaumik, A., & Wu, K. C. W. (2014). Hierarchically porous carbon derived from polymers and biomass: effect of interconnected pores on energy applications. Energy & Environmental Science, 7(11), 3574-3592.

[13] . Qi, G., Wang, Y., Estevez, L., Duan, X., Anako, N., Park, A. H. A., ... & Giannelis, E. P. (2011). High efficiency nanocomposite sorbents for CO2 capture based on amine-functionalized mesoporous capsules. Energy & Environmental Science, 4(2), 444-452.

[14] . Rao, N., Wang, M., Shang, Z., Hou, Y., Fan, G., & Li, J. (2018). CO2 adsorption by amine-functionalized MCM-41: a comparison between impregnation and grafting modification methods. Energy & fuels, 32(1), 670-677.

[15] . Wang, H., Jiang, D., Huang, D., Zeng, G., Xu, P., Lai, C., ... & Wang, Z. (2019). Covalent triazine frameworks for carbon dioxide capture. Journal of Materials Chemistry A, 7(40), 22848-22870.

[16] . Zeng, Y., Zou, R., & Zhao, Y. (2016). Covalent organic frameworks for CO2 capture. Advanced Materials, 28(15), 2855-2873.

[17] . Guan, P., Qiu, J., Zhao, Y., Wang, H., Li, Z., Shi, Y., & Wang, J. (2019). A novel crystalline azine-linked three-dimensional covalent organic framework for CO 2 capture and conversion. Chemical Communications, 55(83), 12459-12462.

[18] . Folgueras, M. B., Alonso, M., & Díaz, R. M. (2013). Influence of sewage sludge treatment on pyrolysis and combustion of dry sludge. Energy, 55, 426-435.

[19] . Mikkelsen, M., Jørgensen, M., & Krebs, F. C. (2010). The teraton challenge. A review of fixation and transformation of carbon dioxide. Energy & Environmental Science, 3(1), 43-81.

[20] . Maeda, C., Miyazaki, Y., & Ema, T. (2014). Recent progress in catalytic conversions of carbon dioxide. Catalysis Science & Technology, 4(6), 1482-1497.

[21] . Fiorani, G., Guo, W., & Kleij, A. W. (2015). Sustainable conversion of carbon dioxide: the advent of organocatalysis. Green Chemistry, 17(3), 1375-1389.

[22] . Wang, W., Wang, S., Ma, X., & Gong, J. (2011). Recent advances in catalytic hydrogenation of carbon dioxide. Chemical Society Reviews, 40(7), 3703-3727.

[23] . Wang, G., Jiang, M., Zhang, Q., Wang, R., & Zhou, G. (2017). Biobased multiblock copolymers: Synthesis, properties and shape memory performance of poly (ethylene 2, 5-furandicarboxylate)-b-poly (ethylene glycol). Polymer Degradation and Stability, 144, 121-127.

[24] . Guo, C. X., Yu, B., Xie, J. N., & He, L. N. (2015). Silver tungstate: a single-component bifunctional catalyst for carboxylation of terminal alkynes with CO 2 in ambient conditions. Green Chemistry, 17(1), 474-479.

[25] . Molla, R. A., Ghosh, K., Banerjee, B., Iqubal, M. A., Kundu, S. K., Islam, S. M., & Bhaumik, A. (2016). Silver nanoparticles embedded over porous metal organic frameworks for carbon dioxide fixation via carboxylation of terminal alkynes at ambient pressure. Journal of colloid and interface science, 477, 220-229.

[26] . Pramudita, R. A., & Motokura, K. (2018). Transformative reduction of carbon dioxide through organocatalysis with silanes. Green Chemistry, 20(21), 4834-4843.

[27] . Goodarzi, F., Kang, L., Wang, F. R., Joensen, F., Kegnæs, S., & Mielby, J. (2018). Methanation of Carbon Dioxide over Zeolite-Encapsulated Nickel Nanoparticles. ChemCatChem, 10(7), 1566-1570.

[28] . Kaiser, P., Unde, R. B., Kern, C., & Jess, A. (2013). Production of liquid hydrocarbons with CO2 as carbon source based on reverse water-gas shift and Fischer-Tropsch synthesis. Chemie Ingenieur Technik, 85(4), 489-499.

[29] . Xiaoding, X., & Moulijn, J. A. (1996). Mitigation of CO2 by chemical conversion: Plausible chemical reactions and promising products. Energy & Fuels, 10(2), 305-325.

[30] . Porosoff, M. D., Yan, B., & Chen, J. G. (2016). Catalytic reduction of CO 2 by H 2 for synthesis of CO, methanol and hydrocarbons: challenges and opportunities. Energy & Environmental Science, 9(1), 62-73.

[31] . Ragsdale, S. W. (2004). Life with carbon monoxide. Critical reviews in biochemistry and molecular biology, 39(3), 165-195.

[32] . Wang, G. C., & Nakamura, J. (2010). Structure sensitivity for forward and reverse water-gas shift reactions on copper surfaces: a DFT study. The Journal of Physical Chemistry Letters, 1(20), 3053-3057.

[33] . Vesselli, E., De Rogatis, L., Ding, X., Baraldi, A., Savio, L., Vattuone, L., ... & Comelli, G. (2008). Carbon dioxide hydrogenation on Ni (110). Journal of the American Chemical Society, 130(34), 11417-11422.

[34] . Kattel, S., Liu, P., & Chen, J. G. (2017). Tuning selectivity of CO2 hydrogenation reactions at the metal/oxide interface. Journal of the American Chemical Society, 139(29), 9739-9754.

[35] . Kwak, J. H., Kovarik, L., & Szanyi, J. (2013). CO2 reduction on supported Ru/Al2O3 catalysts: cluster size dependence of product selectivity. ACS catalysis, 3(11), 2449-2455.

[36] . de Leitenburg, C., Trovarelli, A., & Kašpar, J. (1997). A temperature-programmed and transient kinetic study of CO2Activation and methanation over CeO2Supported noble metals. Journal of Catalysis, 166(1), 98-107.

[37] . Tada, S., Ochieng, O. J., Kikuchi, R., Haneda, T., & Kameyama, H. (2014). Promotion of CO2 methanation activity and CH4 selectivity at low temperatures over Ru/CeO2/Al2O3 catalysts. International journal of hydrogen energy, 39(19), 10090-10100.

[38] . Deleitenburg, C., & Trovarelli, A. (1995). Metal-support interactions in Rh/CeO2, Rh/TiO2, and Rh/Nb2O5 catalysts as inferred from CO2 methanation activity. Journal of Catalysis, 156(1), 171-174.

[39] . Tauster, S. J., Fung, S. C., & Garten, R. L. (1978). Strong metal-support interactions. Group 8 noble metals supported on titanium dioxide. Journal of the American Chemical Society, 100(1), 170-175.

[40] . Sabatier, P., & Senderens, J. B. (1902). Comptes Rendus Des Séances De L'Académie Des Sciences, Section VI– Chimie. Paris: Imprimerie Gauthier-Villars.

[41] . Mills, G. A., & Steffgen, F. W. (1974). Catalytic methanation. Catalysis Reviews, 8(1), 159-210.

[42] . Rönsch, S., Schneider, J., Matthischke, S., Schlüter, M., Götz, M., Lefebvre, J., ... & Bajohr, S. (2016). Review on methanation–From fundamentals to current projects. Fuel, 166, 276-296.

[43] . Fechete, I., & Vedrine, J. C. (2015). Nanoporous materials as new engineered catalysts for the synthesis of green fuels. Molecules, 20(4), 5638-5666.

[44] . Solis-Garcia, A., & Fierro-Gonzalez, J. C. (2019). Mechanistic insights into the CO2 methanation catalyzed by supported metals: a review. Journal of nanoscience and nanotechnology, 19(6), 3110-3123.

[45] . Aziz, M. A. A., Jalil, A. A., Triwahyono, S., & Ahmad, A. (2015). CO 2 methanation over heterogeneous catalysts: Recent progress and future prospects. Green Chemistry, 17(5), 2647-2663.

[46] . Younas, M., Loong Kong, L., Bashir, M. J., Nadeem, H., Shehzad, A., & Sethupathi, S. (2016). Recent advancements, fundamental challenges, and opportunities in catalytic methanation of CO2. Energy & Fuels, 30(11), 8815-8831.

[47] . Aziz, M. A. A., Jalil, A. A., Triwahyono, S., & Sidik, S. M. (2014). Methanation of carbon dioxide on metal-promoted mesostructured silica nanoparticles. Applied Catalysis A: General, 486, 115-122.

[48] . Solymosi, F., & Erdöhelyi, A. (1980). Hydrogenation of CO2 to CH4 over alumina-supported noble metals. Journal of Molecular Catalysis, 8(4), 471-474.

[49] . Panagiotopoulou, P. (2017). Hydrogenation of CO2 over supported noble metal catalysts. Applied Catalysis A: General, 542, 63-70.

[50] . Panagiotopoulou, P., Kondarides, D. I., & Verykios, X. E. (2008). Selective methanation of CO over supported noble metal catalysts: Effects of the nature of the metallic phase on catalytic performance. Applied Catalysis A: General, 344(1-2), 45-54.

[51] . Martin, N. M., Velin, P., Skoglundh, M., Bauer, M., & Carlsson, P. A. (2017). Catalytic hydrogenation of CO 2 to methane over supported Pd, Rh and Ni catalysts. Catalysis Science & Technology, 7(5), 1086-1094.

[52] . Younas, M., Sethupathi, S., Kong, L. L., & Mohamed, A. R. (2018). CO2 methanation over Ni and Rh based catalysts: Process optimization at moderate temperature. International Journal of Energy Research, 42(10), 3289-3302.

[53] . Wambach, J., Baiker, A., & Wokaun, A. (1999). CO 2 hydrogenation over metal/zirconia catalysts. Physical Chemistry Chemical Physics, 1(22), 5071-5080.

[54] . Yaccato, K., Carhart, R., Hagemeyer, A., Lesik, A., Strasser, P., Volpe Jr, A. F., ... & Brooks, C. (2005). Competitive CO and CO2 methanation over supported noble metal catalysts in high throughput scanning mass spectrometer. Applied Catalysis A: General, 296(1), 30-48.

[55] . Haruna, A., Chong, F. K., Ho, Y. C., & Merican, Z. M. A. (2022). Preparation and modification methods of defective titanium dioxide-based nanoparticles for photocatalytic wastewater treatment—a comprehensive review. Environmental Science and Pollution Research, 29(47), 70706-70745.

[56] . Yu, Z., & Chuang, S. S. (2008). The effect of Pt on the photocatalytic degradation pathway of methylene blue over TiO2 under ambient conditions. Applied Catalysis B: Environmental, 83(3-4), 277-285.

[57] . Waldner, G., Pourmodjib, M., Bauer, R., & Neumann-Spallart, M. (2003). Photoelectrocatalytic degradation of 4-chlorophenol and oxalic acid on titanium dioxide electrodes. Chemosphere, 50(8), 989-998.

[58] . Daghrir, R., Drogui, P., & Robert, D. (2012). Photoelectrocatalytic technologies for environmental applications. Journal of Photochemistry and Photobiology A: Chemistry, 238, 41-52.

[59] . Ouyang, J., Chang, M., & Li, X. (2012). CdS-sensitized ZnO nanorod arrays coated with TiO 2 layer for visible light photoelectrocatalysis. Journal of Materials Science, 47, 4187-4193.

[60] . Di Valentin, C., Finazzi, E., Pacchioni, G., Selloni, A., Livraghi, S., Paganini, M. C., & Giamello, E. (2007). N-doped TiO2: Theory and experiment. Chemical Physics, 339(1-3), 44-56.

[61] . Robert, D. (2007). Photosensitization of TiO2 by MxOy and MxSy nanoparticles for heterogeneous photocatalysis applications. Catalysis Today, 122(1-2), 20-26.

[62] . Wang, H., & Lewis, J. P. (2005). Second-generation photocatalytic materials: anion-doped TiO2. Journal of Physics: Condensed Matter, 18(2), 421.

[63] . Sakthivel, S., Janczarek, M., & Kisch, H. (2004). Visible light activity and photoelectrochemical properties of nitrogen-doped TiO2. The Journal of Physical Chemistry B, 108(50), 19384-19387.

[64] . Fan, C., Xue, P., & Sun, Y. (2006). Preparation of nano-TiO2 doped with cerium and its photocatalytic activity. Journal of Rare Earths, 24(3), 309-313.

[65] . Teh, C. M., & Mohamed, A. R. (2011). Roles of titanium dioxide and ion-doped titanium dioxide on photocatalytic degradation of organic pollutants (phenolic compounds and dyes) in aqueous solutions: A review. Journal of Alloys and Compounds, 509(5), 1648-1660.

[66] . Wu, J. C., & Lin, H. M. (2005). Photo reduction of CO2 to methanol via TiO2 photocatalyst. International Journal of Photoenergy, 7(3), 115-119.

[67] . Xie, T. F., Wang, D. J., Zhu, L. J., Li, T. J., & Xu, Y. J. (2001). Application of surface photovoltage technique in photocatalysis studies on modified TiO2 photo-catalysts for photo-reduction of CO2. Materials chemistry and physics, 70(1), 103-106.

[68] . Nematollahi, R., Ghotbi, C., Khorasheh, F., & Larimi, A. (2020). Ni-Bi co-doped TiO2 as highly visible light response nano-photocatalyst for CO2 photo-reduction in a batch photo-reactor. Journal of CO2 Utilization, 41, 101289.

[69] . Wang, M., Shen, M., Jin, X., Tian, J., Li, M., Zhou, Y., ... & Shi, J. (2019). Oxygen vacancy generation and stabilization in CeO2–x by Cu introduction with improved CO2 photocatalytic reduction activity. ACS Catalysis, 9(5), 4573-4581.

[70] . Ullah, R., & Dutta, J. (2008). Photocatalytic degradation of organic dyes with manganese-doped ZnO nanoparticles. Journal of Hazardous materials, 156(1-3), 194-200.

[71] . Lu, C. H., Hu, C. Y., & Wu, C. H. (2008). Low-temperature preparation and characterization of iron-ion doped titania thin films. Journal of hazardous materials, 159(2-3), 636-639.

[72] . Cao, J., Zhang, Y., Liu, L., & Ye, J. (2013). A p-type Cr-doped TiO 2 photo-electrode for photo-reduction. Chemical Communications, 49(33), 3440-3442.

[73] . Kuriakose, S., Satpati, B., & Mohapatra, S. (2014). Enhanced photocatalytic activity of Co doped ZnO nanodisks and nanorods prepared by a facile wet chemical method. Physical chemistry chemical physics, 16(25), 12741-12749.

[74] . Li, W., Wu, Z., Wang, J., Elzatahry, A. A., & Zhao, D. (2014). A perspective on mesoporous TiO2 materials. Chemistry of materials, 26(1), 287-298.

[75] . Avanesian, T., Gusmão, G. S., & Christopher, P. (2016). Mechanism of CO2 reduction by H2 on Ru (0 0 0 1) and general selectivity descriptors for late-transition metal catalysts. Journal of Catalysis, 343, 86-96.

[76] . Zhang, X., Li, X., Zhang, D., Su, N. Q., Yang, W., Everitt, H. O., & Liu, J. (2017). Product selectivity in plasmonic photocatalysis for carbon dioxide hydrogenation. Nature communications, 8(1), 14542.

[77] . Huakang, Y., Yusi, P., Yang, Y., & Zhi-Yuan, L. (2019). Plasmon-enhanced light–matter interactions and applications. NPJ Computational Materials, 5(1).

[78] . Verbruggen, S. W., Keulemans, M., Martens, J. A., & Lenaerts, S. (2013). Predicting the surface plasmon resonance wavelength of gold–silver alloy nanoparticles. The Journal of Physical Chemistry C, 117(37), 19142-19145.

[79] . Link, S., Wang, Z. L., & El-Sayed, M. A. (1999). Alloy formation of gold− silver nanoparticles and the dependence of the plasmon absorption on their composition. The Journal of Physical Chemistry B, 103(18), 3529-3533.

[80] . Wiley, B. J., Im, S. H., Li, Z. Y., McLellan, J., Siekkinen, A., & Xia, Y. (2006). Maneuvering the surface plasmon resonance of silver nanostructures through shape-controlled synthesis. The Journal of Physical Chemistry B, 110(32), 15666-15675.

[81] . Chen, Y., Munechika, K., & Ginger, D. S. (2007). Dependence of fluorescence intensity on the spectral overlap between fluorophores and plasmon resonant single silver nanoparticles. Nano letters, 7(3), 690-696.

[82] . Shen, S., Liu, T., & Guo, J. (1998). Optical phase-shift detection of surface plasmon resonance. Applied optics, 37(10), 1747-1751.

[83] . Boyd, R. W., Gaeta, A. L., & Giese, E. (2008). Nonlinear optics. In Springer Handbook of Atomic, Molecular, and Optical Physics (pp. 1097-1110). Cham: Springer International Publishing.

[84] . Moskovits, M. (1985). Surface-enhanced spectroscopy. Reviews of modern physics, 57(3), 783.

[85] . Otto, A., Mrozek, I., Grabhorn, H., & Akemann, W. (1992). Surface-enhanced Raman scattering. Journal of Physics: Condensed Matter, 4(5), 1143.

[86] . Campion, A., & Kambhampati, P. (1998). Surface-enhanced Raman scattering. Chemical society reviews, 27(4), 241-250.

[87] . Pettinger, B., Schambach, P., Villagómez, C. J., & Scott, N. (2012). Tip-enhanced Raman spectroscopy: near-fields acting on a few molecules. Annual review of physical chemistry, 63(1), 379-399.

[88] . Schmid, T., Opilik, L., Blum, C., & Zenobi, R. (2013). Nanoscale chemical imaging using tip-enhanced Raman spectroscopy: a critical review. Angewandte Chemie International Edition, 52(23), 5940-5954.

[89] . Zhang, Z., Sheng, S., Wang, R., & Sun, M. (2016). Tip-enhanced Raman spectroscopy.

[90] . Govorov, A. O., & Richardson, H. H. (2007). Generating heat with metal nanoparticles. Nano today, 2(1), 30-38.

[91] . Baffou, G., & Quidant, R. (2013). Thermo-plasmonics: using metallic nanostructures as nano-sources of heat. Laser & Photonics Reviews, 7(2), 171-187.

[92] . Brongersma, M. L., Halas, N. J., & Nordlander, P. (2015). Plasmon-induced hot carrier science and technology. Nature nanotechnology, 10(1), 25-34.174. 10.1038/s41929-020-00544-3

[93] . Link, S., Burda, C., Mohamed, M. B., Nikoobakht, B., & El-Sayed, M. A. (1999). Laser photothermal melting and fragmentation of gold nanorods: energy and laser pulse-width dependence. The Journal of Physical Chemistry A, 103(9), 1165-1170.

[94] . Link, S., Burda, C., Nikoobakht, B., & El-Sayed, M. A. (2000). Laser-induced shape changes of colloidal gold nanorods using femtosecond and nanosecond laser pulses. The Journal of Physical Chemistry B, 104(26), 6152-6163.

[95] . Richardson, H. H., Thomas, A. C., Carlson, M. T., Kordesch, M. E., & Govorov, A. O. (2007). Thermo-optical responses of nanoparticles: Melting of ice and nanocalorimetry approach. Journal of electronic materials, 36, 1587-1593.

[96] . Liu, G. L., Kim, J., Lu, Y. U., & Lee, L. P. (2006). Optofluidic control using photothermal nanoparticles. Nature materials, 5(1), 27-32.

[97] . Boyd, D. A., Adleman, J. R., Goodwin, D. G., & Psaltis, D. (2008). Chemical separations by bubble-assisted interphase mass-transfer. Analytical Chemistry, 80(7), 2452-2456.

[98] . Doane, T. L., & Burda, C. (2012). The unique role of nanoparticles in nanomedicine: imaging, drug delivery and therapy. Chemical Society Reviews, 41(7), 2885-2911.

[99] . Kim, C., Favazza, C., & Wang, L. V. (2010). In vivo photoacoustic tomography of chemicals: high-resolution functional and molecular optical imaging at new depths. Chemical reviews, 110(5), 2756-2782.

[100] . Boyer, D., Tamarat, P., Maali, A., Lounis, B., & Orrit, M. (2002). Photothermal imaging of nanometer-sized metal particles among scatterers. Science, 297(5584), 1160-1163.

[101] . Hu, M., Chen, J., Li, Z. Y., Au, L., Hartland, G. V., Li, X., ... & Xia, Y. (2006). Gold nanostructures: engineering their plasmonic properties for biomedical applications. Chemical Society Reviews, 35(11), 1084-1094.

[102] . Hirsch, L. R., Stafford, R. J., Bankson, J. A., Sershen, S. R., Rivera, B., Price, R. E., ... & West, J. L. (2003). Nanoshell-mediated near-infrared thermal therapy of tumors under magnetic resonance guidance. Proceedings of the National Academy of Sciences, 100(23), 13549-13554.

[103] . Huang, X., El-Sayed, I. H., Qian, W., & El-Sayed, M. A. (2006). Cancer cell imaging and photothermal therapy in the near-infrared region by using gold nanorods. Journal of the American Chemical Society, 128(6), 2115-2120.

[104] . Pissuwan, D., Valenzuela, S. M., & Cortie, M. B. (2006). Therapeutic possibilities of plasmonically heated gold nanoparticles. TRENDS in Biotechnology, 24(2), 62-67.

[105] . Skirtach, A. G., Dejugnat, C., Braun, D., Susha, A. S., Rogach, A. L., Parak, W. J., ... & Sukhorukov, G. B. (2005). The role of metal nanoparticles in remote release of encapsulated materials. Nano letters, 5(7), 1371-1377.

[106] . Zharov, V. P., Mercer, K. E., Galitovskaya, E. N., & Smeltzer, M. S. (2006). Photothermal nanotherapeutics and nanodiagnostics for selective killing of bacteria targeted with gold nanoparticles. Biophysical journal, 90(2), 619-627.

[107] . Neumann, O., Feronti, C., Neumann, A. D., Dong, A., Schell, K., Lu, B., ... & Halas, N. J. (2013). Compact solar autoclave based on steam generation using broadband light-harvesting nanoparticles. Proceedings of the National Academy of Sciences, 110(29), 11677-11681.

[108] . Zhang, Y., He, S., Guo, W., Hu, Y., Huang, J., Mulcahy, J. R., & Wei, W. D. (2017). Surface-plasmon-driven hot electron photochemistry. Chemical reviews, 118(6), 2927-2954.

[109] . Kale, M. J., Avanesian, T., & Christopher, P. (2014). Direct photocatalysis by plasmonic nanostructures. Acs Catalysis, 4(1), 116-128.

[110] . Fu, G., Jiang, M., Liu, J., Zhang, K., Hu, Y., Xiong, Y., ... & Jin, Z. (2021). Rh/Al nanoantenna photothermal catalyst for wide-spectrum solar-driven CO2 methanation with nearly 100% selectivity. Nano Letters, 21(20), 8824-8830.

[111] . Park, J. Y., Baker, L. R., & Somorjai, G. A. (2015). Role of hot electrons and metal–oxide interfaces in surface chemistry and catalytic reactions. Chemical reviews, 115(8), 2781-2817.

[112] . Boerigter, C., Campana, R., Morabito, M., & Linic, S. (2016). Evidence and implications of direct charge excitation as the dominant mechanism in plasmon-mediated photocatalysis. Nature communications, 7(1), 10545.

[113] . Foerster, B., Joplin, A., Kaefer, K., Celiksoy, S., Link, S., & Sönnichsen, C. (2017). Chemical interface damping depends on electrons reaching the surface. ACS nano, 11(3), 2886-2893.

[114] . Hou, C., Zhao, G., Ji, Y., Niu, Z., Wang, D., & Li, Y. (2014). Hydroformylation of alkenes over rhodium supported on the metal-organic framework ZIF-8. Nano Research, 7, 1364-1369.

[115] . Xie, S., Liu, X. Y., & Xia, Y. (2015). Shape-controlled syntheses of rhodium nanocrystals for the enhancement of their catalytic properties. Nano Research, 8, 82-96.

[116] . Zhang, X., Li, X., Reish, M. E., Zhang, D., Su, N. Q., Gutiérrez, Y., ... & Liu, J. (2018). Plasmon-enhanced catalysis: distinguishing thermal and nonthermal effects. Nano letters, 18(3), 1714-1723.

[117] . Christopher, P., & Moskovits, M. (2017). Hot charge carrier transmission from plasmonic nanostructures. Annual review of physical chemistry, 68(1), 379-398.

[118] . Doiron, B., Li, Y., Mihai, A., Bower, R., Alford, N. M., Petrov, P. K., ... & Oulton, R. F. (2019). Plasmon-enhanced electron harvesting in robust titanium nitride nanostructures. The Journal of Physical Chemistry C, 123(30), 18521-18527.

[119] Thampi, K. R., Kiwi, J., & Graetzel, M. (1987). Methanation and photo-methanation of carbon dioxide at room temperature and atmospheric pressure. Nature, 327(6122), 506-508.

[120] . Melsheimer, J., Guo, W., Ziegler, D., Wesemann, M., & Schlögl, R. (1991). Methanation of carbon dioxide over Ru/titania at room temperature: explorations for a photoassisted catalytic reaction. Catalysis letters, 11, 157-168.

[121] . O'Brien, P. G., Sandhel, A., Wood, T. E., Ali, F. M., Hoch, L. B., Perovic, D. D., ... & Ozin, G. A. (2014). Photomethanation of gaseous CO2 over Ru/Silicon nanowire catalysts with visible and near-infrared photons. Advanced Science, 1(1), 1400001.5. 10.1002/aenm.202201009

[122] . Chen, Y., Long, J., & Li, Z. (2019). Efficient photothermal CO2 methanation over RuO2/SrTiO3. Trends in Chemistry, 1(5), 459-460.

[123] . Ghoussoub, M., Xia, M., Duchesne, P. N., Segal, D., & Ozin, G. (2019). Principles of photothermal gas-phase heterogeneous CO 2 catalysis. Energy & Environmental Science, 12(4), 1122-1142.

[124] . Zhang, X., Liu, H., Wang, Y., Yang, S., Chen, Q., Zhao, Z., ... & Xie, Z. (2022). Hot-electron-induced CO2 hydrogenation on Au@ AuRu/g-C3N4 plasmonic bimetal–semiconductor heterostructure. Chemical Engineering Journal, 443, 136482.

[125] . Hartland, G. V., Besteiro, L. V., Johns, P., & Govorov, A. O. (2017). What's so hot about electrons in metal nanoparticles?. ACS Energy Letters, 2(7), 1641-1653.

[126] . Gelle, A., Jin, T., de la Garza, L., Price, G. D., Besteiro, L. V., & Moores, A. (2019). Applications of plasmon-enhanced nanocatalysis to organic transformations. Chemical reviews, 120(2), 986-1041.

[127] . Jiao, J., Wei, Y., Zhao, Z., Zhong, W., Liu, J., Li, J., ... & Jiang, G. (2015). Synthesis of 3D ordered macroporous TiO2-supported Au nanoparticle photocatalysts and their photocatalytic performances for the reduction of CO2 to methane. Catalysis Today, 258, 319-326.

[128] . Xiong, Y., Liu, X., Hu, Y., Gu, D., Jiang, M., Tie, Z., & Jin, Z. (2022). Ag24Au cluster decorated mesoporous Co3O4 for highly selective and efficient photothermal CO2 hydrogenation. Nano Research, 15(6), 4965-4972.

[129] . Tahir, M., Tahir, B., & Amin, N. A. S. (2015). Gold-nanoparticle-modified TiO2 nanowires for plasmon-enhanced photocatalytic CO2 reduction with H2 under visible light irradiation. Applied Surface Science, 356, 1289-1299.

[130] . He, X., Liu, M., Liang, Z., Wang, Z., Wang, P., Liu, Y., ... & Huang, B. (2021). Photo-enhanced CO2 hydrogenation by plasmonic Cu/ZnO at atmospheric pressure. Journal of Solid State Chemistry, 298, 122113.

[131] . Ullah, S., Lovell, E. C., Wong, R. J., Tan, T. H., Scott, J., & Amal, R. (2020). Light-enhanced CO2 reduction to CH4 using nonprecious transition-metal catalysts. ACS Sustainable Chemistry & Engineering, 8(13), 5056-5066.

[132] . Mateo, D., Navarro, J. C., Khan, I. S., Ruiz-Martinez, J., & Gascon, J. (2022). Plasmonic titanium nitride tubes decorated with Ru nanoparticles as photo-thermal catalyst for CO2 methanation. Molecules, 27(9), 2701.

[133] . Li, J., Ye, Y., Ye, L., Su, F., Ma, Z., Huang, J., ... & Zhou, Y. (2019). Sunlight induced photo-thermal synergistic catalytic CO 2 conversion via localized surface plasmon resonance of MoO 3− x. Journal of Materials Chemistry A, 7(6), 2821-2830.

[134] . Christopher, P., Xin, H., & Linic, S. (2011). Visible-light-enhanced catalytic oxidation reactions on plasmonic silver nanostructures. Nature chemistry, 3(6), 467-472.

[135] . Xiong, Y., Chen, H., Hu, Y., Yang, S., Xue, X., He, L., ... & Jin, Z. (2021). Photodriven catalytic hydrogenation of CO2 to CH4 with nearly 100% selectivity over Ag25 clusters. Nano Letters, 21(20), 8693-8700.

[136] . Mukherjee, S., Libisch, F., Large, N., Neumann, O., Brown, L. V., Cheng, J., ... & Halas, N. J. (2013). Hot electrons do the impossible: plasmon-induced dissociation of H2 on Au. Nano letters, 13(1), 240-247.

[137] . Guan, P., Qiu, J., Zhao, Y., Wang, H., Li, Z., Shi, Y., & Wang, J. (2019). A novel crystalline azine-linked three-dimensional covalent organic framework for CO 2 capture and conversion. Chemical Communications, 55(83), 12459-12462.

[138] . Avanesian, T., Gusmão, G. S., & Christopher, P. (2016). Mechanism of CO2 reduction by H2 on Ru (0 0 0 1) and general selectivity descriptors for late-transition metal catalysts. Journal of Catalysis, 343, 86-96.

[139] Tan, T. H., Xie, B., Ng, Y. H., Abdullah, S. F. B., Tang, H. Y. M., Bedford, N., ... & Scott, J. (2020). Unlocking the potential of the formate pathway in the photo-assisted Sabatier reaction. Nature Catalysis, 3(12), 1034-1043.

[140] . Zhao, J., Bai, Y., Liang, X., Wang, T., & Wang, C. (2021). Photothermal catalytic CO2 hydrogenation over molybdenum carbides: Crystal structure and photothermocatalytic synergistic effects. Journal of CO2 Utilization, 49, 101562.

[141] . Zhao, B., Sun, M., Chen, F., Wang, W., Lu, S., & Zhang, B. (2021). Photoinduced reaction pathway change for boosting CO2 hydrogenation over a MnO-Co catalyst. ACS Catalysis, 11(16), 10316-10323.

[142] . Tang, Y., Yang, Z., Guo, C., Han, H., Jiang, Y., Wang, Z., ... & Wang, F. (2022). Encapsulating Ir nanoparticles into UiO-66 for photo-thermal catalytic CO 2 methanation under ambient pressure. Journal of Materials Chemistry A, 10(22), 12157-12167.

[143] . Marchuk, K., & Willets, K. A. (2014). Localized surface plasmons and hot electrons. Chemical Physics, 445, 95-104.

[144] . Wu, K., Chen, J., McBride, J. R., & Lian, T. (2015). Efficient hot-electron transfer by a plasmon-induced interfacial charge-transfer transition. Science, 349(6248), 632-635.

[145] . Watanabe, K., Menzel, D., Nilius, N., & Freund, H. J. (2006). Photochemistry on metal nanoparticles. Chemical reviews, 106(10), 4301-4320.

[146] . Boerigter, C., Aslam, U., & Linic, S. (2016). Mechanism of charge transfer from plasmonic nanostructures to chemically attached materials. ACS nano, 10(6), 6108-6115.

[147] . Kim, C., Hyeon, S., Lee, J., Kim, W. D., Lee, D. C., Kim, J., & Lee, H. (2018). Energy-efficient CO2 hydrogenation with fast response using photoexcitation of CO2 adsorbed on metal catalysts. Nature communications, 9(1), 3027.

[148] . Naldoni, A., Montini, T., Malara, F., Mróz, M. M., Beltram, A., Virgili, T., ... & Fornasiero, P. (2017). Hot electron collection on brookite nanorods lateral facets for plasmon-enhanced water oxidation. ACS Catalysis, 7(2), 1270-1278.

[149] . Ratchford, D. C., Dunkelberger, A. D., Vurgaftman, I., Owrutsky, J. C., & Pehrsson, P. E. (2017). Quantification of efficient plasmonic hot-electron injection in gold nanoparticle–TiO2 films. Nano letters, 17(10), 6047-6055.

[150] . Tan, S., Argondizzo, A., Ren, J., Liu, L., Zhao, J., & Petek, H. (2017). Plasmonic coupling at a metal/semiconductor interface. Nature Photonics, 11(12), 806-812.

[151] . Yu, S., Wilson, A. J., Kumari, G., Zhang, X., & Jain, P. K. (2017). Opportunities and challenges of solar-energy-driven carbon dioxide to fuel conversion with plasmonic catalysts. ACS Energy Letters, 2(9), 2058-2070.

[152] . Rohlfs, J., Bossers, K. W., Meulendijks, N., Valega Mackenzie, F., Xu, M., Verheijen, M. A., ... & Sastre, F. (2022). Continuous-flow sunlight-powered CO2 methanation catalyzed by γ-Al2O3-supported plasmonic Ru nanorods. Catalysts, 12(2), 126.

[153] . Chen, G., Gao, R., Zhao, Y., Li, Z., Waterhouse, G. I., Shi, R., ... & Zhang, T. (2018). Alumina-supported CoFe alloy catalysts derived from layered-double-hydroxide nanosheets for efficient photothermal CO2 hydrogenation to hydrocarbons. Advanced Materials, 30(3), 1704663.

[154] . Li, Q., Gao, Y., Zhang, M., Gao, H., Chen, J., & Jia, H. (2022). Efficient infrared-light-driven photothermal CO2 reduction over MOF-derived defective Ni/TiO2. Applied Catalysis B: Environmental, 303, 120905.

[155] . Khan, I. S., Mateo, D., Shterk, G., Shoinkhorova, T., Poloneeva, D., Garzón-Tovar, L., & Gascon, J. (2021). An Efficient Metal–Organic Framework-Derived Nickel Catalyst for the Light Driven Methanation of CO2. Angewandte Chemie, 133(51), 26680-26686.

[156] . Chen, X., Li, Q., Zhang, M., Li, J., Cai, S., Chen, J., & Jia, H. (2020). MOF-templated preparation of highly dispersed Co/Al2O3 composite as the photothermal catalyst with high solar-to-fuel efficiency for CO2 methanation. ACS applied materials & interfaces, 12(35), 39304-39317.

[157] . Li, Z., Shi, R., Zhao, J., & Zhang, T. (2021). Ni-based catalysts derived from layered-double-hydroxide nanosheets for efficient photothermal CO 2 reduction under flow-type system. Nano Research, 14, 4828-4832.

[158] . Christopher, P., Xin, H., Marimuthu, A., & Linic, S. (2012). Singular characteristics and unique chemical bond activation mechanisms of photocatalytic reactions on plasmonic nanostructures. Nature materials, 11(12), 1044-1050.

[159] . Li, X., Everitt, H. O., & Liu, J. (2019). Confirming nonthermal plasmonic effects enhance CO 2 methanation on Rh/TiO 2 catalysts. Nano research, 12, 1906-1911.

[160] . He, Z. H., Li, Z. H., Wang, Z. Y., Wang, K., Sun, Y. C., Wang, S. W., ... & Liu, Z. T. (2021). Photothermal CO 2 hydrogenation to hydrocarbons over trimetallic Co–Cu–Mn catalysts. Green Chemistry, 23(16), 5775-5785.

[161] . Olsen, T., & Schiøtz, J. (2009). Origin of power laws for reactions at metal surfaces mediated by hot electrons. Physical review letters, 103(23), 238301.

[162] . Maeda, K. (2014). Rhodium-doped barium titanate perovskite as a stable p-type semiconductor photocatalyst for hydrogen evolution under visible light. ACS applied materials & interfaces, 6(3), 2167-2173.

[163] . Yu, Y., Williams, J. D., & Willets, K. A. (2018). Quantifying photothermal heating at plasmonic nanoparticles by scanning electrochemical microscopy. Faraday discussions, 210, 29-39.

[164] . Li, X., Everitt, H. O., & Liu, J. (2020). Synergy between thermal and nonthermal effects in plasmonic photocatalysis. Nano Research, 13, 1268-1280.

[165] . Hammer, B., & Norskov, J. K. (1995). Why gold is the noblest of all the metals. Nature, 376(6537), 238-240.

[166] . Grote, R., Habets, R., Rohlfs, J., Sastre, F., Meulendijks, N., Xu, M., ... & Buskens, P. (2020). Collective photothermal effect of Al2O3-supported spheroidal plasmonic Ru nanoparticle catalysts in the sunlight-powered Sabatier reaction. ChemCatChem, 12(22), 5618-5622.

[167] . Li, Y., Wang, C., Song, M., Li, D., Zhang, X., & Liu, Y. (2019). TiO2-x/CoOx photocatalyst sparkles in photothermocatalytic reduction of CO2 with H2O steam. Applied Catalysis B: Environmental, 243, 760-770.

[168] . Li, L., Guo, C., Ning, J., Zhong, Y., Chen, D., & Hu, Y. (2021). Oxygen-vacancy-assisted construction of FeOOH/CdS heterostructure as an efficient bifunctional photocatalyst for CO2 conversion and water oxidation. Applied Catalysis B: Environmental, 293, 120203.

[169] . Sun, M., Zhao, B., Chen, F., Liu, C., Lu, S., Yu, Y., & Zhang, B. (2021). Thermally-assisted photocatalytic CO2 reduction to fuels. Chemical Engineering Journal, 408, 127280.

[170] . Jin, B., Ye, X., Zhong, H., Jin, F., & Hu, Y. H. (2022). Enhanced photocatalytic CO2 hydrogenation with wide-spectrum utilization over black TiO2 supported catalyst. Chinese Chemical Letters, 33(2), 812-816.

[171] Liu, X., Xing, C., Yang, F., Liu, Z., Wang, Y., Dong, T., ... & Zhou, W. (2022). Strong interaction over Ru/Defects-Rich aluminium oxide boosts photothermal CO2 methanation via microchannel flow-type system. Advanced Energy Materials, 12(31), 2201009.

[172] . Ge, H., Kuwahara, Y., Kusu, K., Bian, Z., & Yamashita, H. (2022). Ru/HxMoO3-y with plasmonic effect for boosting photothermal catalytic CO2 methanation. Applied Catalysis B: Environmental, 317, 121734.

[173] . Jantarang, S., Lovell, E. C., Tan, T. H., Xie, B., Scott, J., & Amal, R. (2021). Altering the influence of ceria oxygen vacancies in Ni/Ce x Si y O 2 for photothermal CO 2 methanation. Catalysis Science & Technology, 11(15), 5297-5309.

[174] . Wang, T., Li, W., Xu, D., Wu, X., Cao, L., & Meng, J. (2017). Strong visible absorption and excellent photocatalytic performance of brown TiO2 nanoparticles synthesized using one-step low-temperature process. Chinese Journal of Catalysis, 38(7), 1184-1195.

[175] . Yang, X., Tan, F., Wang, D., Feng, Q., Qiu, D., Dang, D., & Wang, X. (2021). Entrapping Ru nanoparticles into TiO2 nanotube: Insight into the confinement synergy on boosting pho-thermal CO2 methanation activity. Ceramics International, 47(19), 27316-27323.

[176] . Sastre, F., Versluis, C., Meulendijks, N., Rodriguez-Fernandez, J., Sweelssen, J., Elen, K., ... & Buskens, P. (2019). Sunlight-fueled, low-temperature Ru-catalyzed conversion of CO2 and H2 to CH4 with a high photon-to-methane efficiency. ACS omega, 4(4), 7369-7377.

[177] . Mateo, D., Morlanes, N., Maity, P., Shterk, G., Mohammed, O. F., & Gascon, J. (2021). Efficient visible-light driven photothermal conversion of CO2 to methane by nickel nanoparticles supported on barium titanate. Advanced Functional Materials, 31(8), 2008244.

[178] . Jiang, R., Yue, X., Wang, K., Yang, Z., Dai, W., & Fu, X. (2022). Photothermal-Catalyzing CO2 Methanation over Different-Shaped CeO2-Based Ru Nanoparticles. Energy & Fuels, 36(19), 11636-11646.

[179] . Kong, N., Han, B., Li, Z., Fang, Y., Feng, K., Wu, Z., ... & He, L. (2020). Ruthenium nanoparticles supported on Mg (OH) 2 microflowers as catalysts for photothermal carbon dioxide hydrogenation. ACS Applied Nano Materials, 3(3), 3028-3033.

[180] . Kim, S. S., Lee, H. H., & Hong, S. C. (2012). The effect of the morphological characteristics of TiO2 supports on the reverse water–gas shift reaction over Pt/TiO2 catalysts. Applied Catalysis B: Environmental, 119, 100-108.

[181] . Kim, S. S., Park, K. H., & Hong, S. C. (2013). A study of the selectivity of the reverse water–gas-shift reaction over Pt/TiO2 catalysts. Fuel processing technology, 108, 47-54.

[182] . Rahmani, S., Rezaei, M., & Meshkani, F. (2014). Preparation of highly active nickel catalysts supported on mesoporous nanocrystalline γ-Al2O3 for CO2 methanation. Journal of Industrial and Engineering Chemistry, 20(4), 1346-1352.

[183] . Wang, L., Liu, H., Chen, Y., Zhang, R., & Yang, S. (2013). K-Promoted Co–CeO2 catalyst for the reverse water–gas shift reaction. Chemistry Letters, 42(7), 682-683.

[184] . Garbarino, G., Riani, P., Magistri, L., & Busca, G. (2014). A study of the methanation of carbon dioxide on Ni/Al2O3 catalysts at atmospheric pressure. International journal of hydrogen energy, 39(22), 11557-11565.

[185] . Lu, B., & Kawamoto, K. (2012). Direct synthesis of highly loaded and well-dispersed NiO/SBA-15 for producer gas conversion. RSC advances, 2(17), 6800-6805.

[186] . Lu, B., & Kawamoto, K. (2013). Preparation of the highly loaded and well-dispersed NiO/SBA-15 for methanation of producer gas. Fuel, 103, 699-704.

[187] . Goguet, A., Meunier, F. C., Tibiletti, D., Breen, J. P., & Burch, R. (2004). Spectrokinetic investigation of reverse water-gas-shift reaction intermediates over a Pt/CeO2 catalyst. The Journal of Physical Chemistry B, 108(52), 20240-20246.

[188] . Sun, Q., Ye, J., Liu, C. J., & Ge, Q. (2014). In2O3 as a promising catalyst for CO2 utilization: A case study with reverse water gas shift over In2O3. Greenhouse Gases: Science and Technology, 4(1), 140-144.

[189] . Jürgensen, L., Ehimen, E. A., Born, J., & Holm-Nielsen, J. B. (2015). Dynamic biogas upgrading based on the Sabatier process: Thermodynamic and dynamic process simulation. Bioresource technology, 178, 323-329.

[190] . Gao, J., Wang, Y., Ping, Y., Hu, D., Xu, G., Gu, F., & Su, F. (2012). A thermodynamic analysis of methanation reactions of carbon oxides for the production of synthetic natural gas. RSC advances, 2(6), 2358-2368.

[191] . Azpiroz, R., Carretero, E., Cueva, A., González, A., Iglesias, M., & Pérez-Torrente, J. J. (2022). In-flow photocatalytic oxidation of NO on glasses coated with nanocolumnar porous TiO2 thin films prepared by reactive sputtering. Applied Surface Science, 606, 154968.

[192] . Shwetharani, R., Chandan, H. R., Sakar, M., Balakrishna, G. R., Reddy, K. R., & Raghu, A. V. (2020). Photocatalytic semiconductor thin films for hydrogen production and environmental applications. International Journal of Hydrogen Energy, 45(36), 18289-18308.

[193] . Proença, M., Rodrigues, M. S., Meira, D. I., Castro, M. C. R., Rodrigues, P. V., Machado, A. V., ... & Vaz, F. (2022). Optimization of Au: CuO thin films by plasma surface modification for high-resolution LSPR gas sensing at room temperature. Sensors, 22(18), 7043.

[194] . Stucchi, M., Bianchi, C. L., Pirola, C., Vitali, S., Cerrato, G., Morandi, S., ... & Capucci, V. (2015). Surface decoration of commercial micro-sized TiO2 by means of high energy ultrasound: A way to enhance its photocatalytic activity under visible light. Applied Catalysis B: Environmental, 178, 124-132.

[195] . Klein, M., Grabowska, E., & Zaleska, A. (2015). Noble metal modified TiO2 for photocatalytic air purification. Physicochemical Problems of Mineral Processing, 51.

[196] . Ehsan, M. F., Ashiq, M. N., Bi, F., Bi, Y., Palanisamy, S., & He, T. (2014). Preparation and characterization of SrTiO 3–ZnTe nanocomposites for the visible-light photoconversion of carbon dioxide to methane. RSC Advances, 4(89), 48411-48418.

[197] . Sun, X., Xu, K., Chatzitakis, A., & Norby, T. (2021). Photocatalytic generation of gas phase reactive oxygen species from adsorbed water: Remote action and electrochemical detection. Journal of Environmental Chemical Engineering, 9(2), 104809.

[198] . Vilar, V. J., da Costa Filho, B. M., Araújo, A. L., Silva, G. V., Boaventura, R. A., Dias, M. M., & Lopes, J. C. (2017). Intensification of heterogeneous TiO2 photocatalysis using an innovative micro-meso-structured-photoreactor for n-decane oxidation at gas phase.

[199] . Palumbo, R., Keunecke, M., Möller, S., & Steinfeld, A. (2004). Reflections on the design of solar thermal chemical reactors: thoughts in transformation. Energy, 29(5-6), 727-744.

[200] . Meng, X., Wang, T., Liu, L., Ouyang, S., Li, P., Hu, H., ... & Ye, J. (2014). Photothermal conversion of CO2 into CH4 with H2 over group VIII nanocatalysts: an alternative approach for solar fuel production. Angewandte Chemie International Edition, 53(43), 11478-11482.8. 10.1002/anie.201805929

[201] . Westrich, T. A., Dahlberg, K. A., Kaviany, M., & Schwank, J. W. (2011). High-temperature photocatalytic ethylene oxidation over TiO2. The Journal of Physical Chemistry C, 115(33), 16537-16543.

[202] . Tan, T. H., Scott, J., Ng, Y. H., Taylor, R. A., Aguey-Zinsou, K. F., & Amal, R. (2016). Understanding plasmon and band gap photoexcitation effects on the thermal-catalytic oxidation of ethanol by TiO2-supported gold. ACS catalysis, 6(3), 1870-1879.

[203] . Upadhye, A. A., Ro, I., Zeng, X., Kim, H. J., Tejedor, I., Anderson, M. A., ... & Huber, G. W. (2015). Plasmon-enhanced reverse water gas shift reaction over oxide supported Au catalysts. Catalysis Science & Technology, 5(5), 2590-2601.

[204] . Rynkowski, J., Farbotko, J., Touroude, R., & Hilaire, L. (2000). Redox behaviour of ceria–titania mixed oxides. Applied Catalysis A: General, 203(2), 335-348.

[205] . Zhou, G., Hanson, J., & Gorte, R. J. (2008). A thermodynamic investigation of the redox properties of ceria–titania mixed oxides. Applied Catalysis A: General, 335(2), 153-158.

[206] . Danielis, M., Divins, N. J., Llorca, J., Soler, L., Garcia, X., Serrano, I., ... & Trovarelli, A. (2023). In situ investigation of the mechanochemically promoted Pd–Ce interaction under stoichiometric methane oxidation conditions. EES Catalysis, 1(2), 144-152.

[207] Danielis, M., Colussi, S., de Leitenburg, C., Soler, L., Llorca, J., & Trovarelli, A. (2018). Outstanding methane oxidation performance of palladium-embedded ceria catalysts prepared by a one-step dry ball-milling method. Angewandte Chemie, 130(32), 10369-10373.

[208] . Enayati, M. H., & Mohamed, F. A. (2014). Application of mechanical alloying/milling for synthesis of nanocrystalline and amorphous materials. International Materials Reviews, 59(7), 394-416.

[209] . Xu, X. B., Luo, J. S., Liu, M., Wang, Y. Y., Yi, Z., Li, X. B., ... & Tang, Y. J. (2015). The influence of edge and corner evolution on plasmon properties and resonant edge effect in gold nanoplatelets. Physical Chemistry Chemical Physics, 17(4), 2641-2650.

[210] . Schwarz, R. B., & Koch, C. C. (1986). Formation of amorphous alloys by the mechanical alloying of crystalline powders of pure metals and powders of intermetallics. Applied Physics Letters, 49(3), 146-148.

[211] . Danielis, M., Colussi, S., de Leitenburg, C., Soler, L., Llorca, J., & Trovarelli, A. (2019). The effect of milling parameters on the mechanochemical synthesis of Pd–CeO 2 methane oxidation catalysts. Catalysis Science & Technology, 9(16), 4232-4238.

[212] . Brooks, K. P., Hu, J., Zhu, H., & Kee, R. J. (2007). Methanation of carbon dioxide by hydrogen reduction using the Sabatier process in microchannel reactors. Chemical Engineering Science, 62(4), 1161-1170.

[213] . Gao, F., & Goodman, D. W. (2012). Model catalysts: simulating the complexities of heterogeneous catalysts. Annual review of physical chemistry, 63(1), 265-286.

[214] . Abate, S., Mebrahtu, C., Giglio, E., Deorsola, F., Bensaid, S., Perathoner, S., ... & Centi, G. (2016). Catalytic performance of γ-Al2O3–ZrO2–TiO2–CeO2 composite oxide supported Ni-based catalysts for CO2 methanation. Industrial & Engineering Chemistry Research, 55(16), 4451-4460.

[215] . Zhang, Z. L., Tsipouriari, V. A., Efstathiou, A. M., & Verykios, X. E. (1996). Reforming of methane with carbon dioxide to synthesis gas over supported rhodium catalysts: I. Effects of support and metal crystallite size on reaction activity and deactivation characteristics. Journal of Catalysis, 158(1), 51-63.

[216] . Zhang, Z. L., Kladi, A., & Verykios, X. E. (1995). Surface species formed during CO and CO2 hydrogenation over Rh/TiO2 (W6+) catalysts investigated by FTIR and mass-spectroscopy. Journal of Catalysis, 156(1), 37-50.

[217] . Dwyer, D. J., & Hardenbergh, J. H. (1984). The catalytic reduction of carbon monoxide over iron surfaces: A surface science investigation. Journal of Catalysis, 87(1), 66-76.

[218] . Van't Blik, H. F. J., Van Zon, J. B. A. D., Huizinga, T., Vis, J. C., Koningsberger, D. C., & Prins, R. (1985). Structure of rhodium in an ultradispersed rhodium/alumina catalyst as studied by EXAFS and other techniques. Journal of the American Chemical Society, 107(11), 3139-3147.

[219] . Yates, D. J. C., & Sinfelt, J. H. (1967). The catalytic activity of rhodium in relation to its state of dispersion. Journal of Catalysis, 8(4), 348-358.

[220] . Schaepe, K., Borchert, H., Pohl, M. M., Armbrüster, M., & Behrens, M. (2020). Selective propane dehydrogenation with atomically dispersed rhodium–gallium catalysts. ChemCatChem, 12(2), 625–634.

[221] . Gascón, J., Müller, K., & Kapteijn, F. (2024). Deactivation of supported Rh catalysts in alkane dehydrogenation by coke formation: A microkinetic and experimental study. Catalysis Today. Advance online publication.

[222] . Mascaretti, L., & Naldoni, A. (2020). Hot electron and thermal effects in plasmonic photocatalysis. Journal of Applied Physics, 128(4).

[223] . Kuznetsov, A. Y., Machado, R., Gomes, L. S., Achete, C. A., Swamy, V., Muddle, B. C., & Prakapenka, V. (2009). Size dependence of rutile TiO2 lattice parameters determined via simultaneous size, strain, and shape modeling. Applied Physics Letters, 94(19).

[224] . Gionco, C., Paganini, M. C., Agnoli, S., Reeder, A. E., & Giamello, E. (2013). Structural and spectroscopic characterization of CeO 2–TiO 2 mixed oxides. Journal of Materials Chemistry A, 1(36), 10918-10926.

[225] . Johnston-Peck, A. C., Senanayake, S. D., Plata, J. J., Kundu, S., Xu, W., Barrio, L., ... & Rodriguez, J. A. (2013). Nature of the mixed-oxide interface in ceria–titania catalysts: Clusters, chains, and nanoparticles. The Journal of Physical Chemistry C, 117(28), 14463-14471.

[226] . Sutcu, M., Akkurt, S., & Okur, S. (2009). Influence of crystallographic orientation on hydration of MgO single crystals. Ceramics international, 35(7), 2571-2576.

[227] . Watanabe, S., Ma, X., & Song, C. (2009). Characterization of structural and surface properties of nanocrystalline TiO2− CeO2 mixed oxides by XRD, XPS, TPR, and TPD. The Journal of Physical Chemistry C, 113(32), 14249-14257.

[228] . Vidal, H., Kašpar, J., Pijolat, M., Colon, G., Bernal, S., Cordón, A., ... & Fally, F. (2000). Redox behaviour of CeO2–ZrO2 mixed oxides: I. Influence of redox treatments on high surface area catalysts. Applied Catalysis B: Environmental, 27(1), 49-63.

[229a] . Trovarelli, A. (1996). Catalytic properties of ceria and CeO2-containing materials. Catalysis Reviews, 38(4), 439-520.

[229b] . Fornasiero, P., Balducci, G., Di Monte, R., Kašpar, J., Sergo, V., Gubitosa, G.& Graziani, M. (1996). Modification of the redox behaviour of CeO2Induced by structural doping with ZrO2. Journal of Catalysis, 164(1), 173-183.

[230] . Buonsanti, R., & Milliron, D. J. (2013). Chemistry of doped colloidal nanocrystals. Chemistry of Materials, 25(8), 1305-1317.

[231] . Makuła, P., Pacia, M., & Macyk, W. (2018). How to correctly determine the band gap energy of modified semiconductor photocatalysts based on UV–Vis spectra. The journal of physical chemistry letters, 9(23), 6814-6817.

[232] . Gulicovski, J. J., Bračko, I., & Milonjić, S. K. (2014). Morphology and the isoelectric point of nanosized aqueous ceria sols. Materials chemistry and physics, 148(3), 868-873.

[233] . Thill, A. S., Lobato, F. O., Vaz, M. O., Fernandes, W. P., Carvalho, V. E., Soares, E. A., ... & Bernardi, F. (2020). Shifting the band gap from UV to visible region in cerium oxide nanoparticles. Applied Surface Science, 528, 146860.

[234] . Putri, G. E., Arief, S., Jamarun, N., Gusti, F. R., & Zainul, R. (2019). Microstructural analysis and optical properties of nanocrystalline cerium oxides synthesized by precipitation method. Rasayan J. Chem, 12(1), 85-90.

[235] . Reddy, B. M., & Khan, A. (2005). Nanosized CeO 2–SiO 2, CeO 2–TiO 2, and CeO 2–ZrO 2 mixed oxides: influence of supporting oxide on thermal stability and oxygen storage properties of ceria. Catalysis Surveys from Asia, 9, 155-171.

[236] Reddy, B. M., & Khan, A. (2005). Nanosized CeO2–SiO2, CeO2–TiO2, and CeO2–ZrO2 mixed oxides: influence of supporting oxide on thermal stability and oxygen storage properties of ceria. Catalysis Surveys from Asia, 9, 155-171.

[236b] Weber, M. L., Jennings, D., Fearn, S., Cavallaro, A., Prochazka, M., Gutsche, A., ... & Gunkel, F. (2024). Thermal stability and coalescence dynamics of exsolved metal nanoparticles at charged perovskite surfaces. Nature Communications, 15(1), 9724.

[237] . Danielis, M., Betancourt, L. E., Orozco, I., Divins, N. J., Llorca, J., Rodríguez, J. A., ... & Trovarelli, A. (2021). Methane oxidation activity and nanoscale characterization of Pd/CeO2 catalysts prepared by dry milling Pd acetate and ceria. Applied Catalysis B: Environmental, 282, 119567.

[238] . Furlani, E., Aneggi, E., de Leitenburg, C., & Maschio, S. (2014). High energy ball milling of titania and titania–ceria powder mixtures. Powder technology, 254, 591-596.

[239] . Camposeco, R., Castillo, S., Hinojosa-Reyes, M., Zanella, R., López-Curiel, J. C., Fuentes, G. A., & Mejía-Centeno, I. (2019). Active TiO 2-nanostructured surfaces for CO oxidation on Rh model catalysts at low-temperature. Catalysis Letters, 149, 1565-1578.

[240] . Pitkäaho, S., Matejova, L., Jiratova, K., Ojala, S., & Keiski, R. L. (2012). Oxidation of perchloroethylene—activity and selectivity of Pt, Pd, Rh, and V2O5 catalysts supported on Al2O3, Al2O3–TiO2 and Al2O3–CeO2. Part 2. Applied Catalysis B: Environmental, 126, 215-224.

[241] . Belzunegui, J. P., Rojo, J. M., & Sanz, J. (1989). Influence of oxidation/reduction pretreatment on hydrogen adsorption on Rh/TiO 2 catalysts. An 1 H nuclear magnetic resonance study. Journal of the Chemical Society, Faraday Transactions 1: Physical Chemistry in Condensed Phases, 85(12), 4287-4293.

[242] . Tournayan, L., Marcilio, N. R., & Frety, R. (1991). Promotion of hydrogen uptake in cerium dioxide: the role of iridium. Applied catalysis, 78(1), 31-43.

[243] . Singh, A. K., Pande, N. K., & Bell, A. T. (1985). Electron microscopy study of the interactions of rhodium with titania. Journal of Catalysis, 94(2), 422-435.

[244] . Makuła, P., Pacia, M., & Macyk, W. (2018). How to correctly determine the band gap energy of modified semiconductor photocatalysts based on UV–Vis spectra. The journal of physical chemistry letters, 9(23), 6814-6817.

[245] . Mateo, D., Cerrillo, J. L., Durini, S., & Gascon, J. (2021). Fundamentals and applications of photo-thermal catalysis. Chemical Society Reviews, 50(3), 2173-2210.

[246] . Liu, W., Chen, D., Yoo, S. H., & Cho, S. O. (2013). Hierarchical visible-light-response Ag/AgCl@ TiO2 plasmonic photocatalysts for organic dye degradation. Nanotechnology, 24(40), 405706.

[247] . Antosiewicz, T. J., & Apell, S. P. (2015). Optical enhancement of plasmonic activity of catalytic metal nanoparticles. RSC advances, 5(9), 6378-6384.

[248] . Alcaraz de la Osa, R., Sanz, J. M., Barreda, A. I., Saiz, J. M., González, F., Everitt, H. O., & Moreno, F. (2015). Rhodium tripod stars for UV plasmonics. The Journal of Physical Chemistry C, 119(22), 12572-12580.

[249] . Yang, W., Xia, B., Wang, L., Ma, S., Liang, H., Wang, D., & Huang, J. (2021). Shape effects of gold nanoparticles in photothermal cancer therapy. Materials Today Sustainability, 13, 100078.

[250] . Yadav, R., Verma, V., Mishra, A., Pal, N., Khan, A., & Sinha, A. K. (2021). Si incorporated Pt nanoparticles on TixSi1-xO2 support: Photo-thermal CO2 reduction. Journal of CO2 Utilization, 47, 101502.

[251] . Deng, B., Song, H., Peng, K., Li, Q., & Ye, J. (2021). Metal-organic framework-derived Ga-Cu/CeO2 catalyst for highly efficient photothermal catalytic CO2 reduction. Applied Catalysis B: Environmental, 298, 120519.

[252] . Montini, T., Melchionna, M., Monai, M., & Fornasiero, P. (2016). Fundamentals and catalytic applications of CeO2-based materials. Chemical reviews, 116(10), 5987-6041.

[253] . Golovanova, V., Spadaro, M. C., Arbiol, J., Golovanov, V., Rantala, T. T., Andreu, T., & Morante, J. R. (2021). Effects of solar irradiation on thermally driven CO2 methanation using Ni/CeO2–based catalyst. Applied Catalysis B: Environmental, 291, 120038.

[254] . Muller, M. B., Kuttner, C., Konig, T. A., Tsukruk, V. V., Forster, S., Karg, M., & Fery, A. (2014). Plasmonic library based on substrate-supported gradiential plasmonic arrays. ACS nano, 8(9), 9410-9421.

[255] . Wang, S., Zeng, B., & Li, C. (2018). Effects of Au nanoparticle size and metal-support interaction on plasmon-induced photocatalytic water oxidation. Chinese Journal of Catalysis, 39(7), 1219-1227.

[256] . Pinto, F. M., Suzuki, V. Y., Silva, R. C., & La Porta, F. A. (2019). Oxygen defects and surface chemistry of reducible oxides. Frontiers in Materials, 6, 260.

[257] . Wang, F., Jiang, J., & Wang, B. (2019). Recent in situ/operando spectroscopy studies of heterogeneous catalysis with reducible metal oxides as supports. Catalysts, 9(5), 477.

[258] . Bernal, S., Calvino, J. J., Cifredo, G. A., Laachir, A., Perrichon, V., & Herrmann, J. M. (1994). Influence of the reduction/evacuation conditions on the rate of hydrogen spillover on Rh/CeO2 catalysts. Langmuir, 10(3), 717-722.

[259] . Panayotov, D., Mihaylov, M., Nihtianova, D., Spassov, T., & Hadjiivanov, K. (2014). Spectral evidence for hydrogen-induced reversible segregation of CO adsorbed on titania-supported rhodium. Physical Chemistry Chemical Physics, 16(26), 13136-13144.

[260] . Falbo, L., Visconti, C. G., Lietti, L., & Szanyi, J. (2019). The effect of CO on CO2 methanation over Ru/Al2O3 catalysts: a combined steady-state reactivity and transient DRIFT spectroscopy study. Applied Catalysis B: Environmental, 256, 117791.

[261] . Beuls, A., Swalus, C., Jacquemin, M., Heyen, G., Karelovic, A., & Ruiz, P. (2012). Methanation of CO2: Further insight into the mechanism over Rh/γ-Al2O3 catalyst. Applied Catalysis B: Environmental, 113, 2-10.

[262] . Jacquemin, M., Beuls, A., & Ruiz, P. (2010). Catalytic production of methane from CO2 and H2 at low temperature: Insight on the reaction mechanism. Catalysis Today, 157(1-4), 462-466.

[263] . Karelovic, A., & Ruiz, P. (2013). Mechanistic study of low temperature CO2 methanation over Rh/TiO2 catalysts. Journal of Catalysis, 301, 141-153.

[264] . Prairie, M. R., Renken, A., Highfield, J. G., Thampi, K. R., & Grätzel, M. (1991). A fourier transform infrared spectroscopic study of C02 methanation on supported ruthenium. Journal of Catalysis, 129(1), 130-144.

[265] . Williams, K. J., Boffa, A. B., Salmeron, M., Bell, A. T., & Somorjai, G. A. (1991). The kinetics of CO 2 hydrogenation on a Rh foil promoted by titania overlayers. Catalysis letters, 9, 415-426.

[266] . Cárdenas-Arenas, A., Quindimil, A., Davó-Quiñonero, A., Bailón-García, E., Lozano-Castello, D., De-La-Torre, U., ... & Bueno-López, A. (2020). Isotopic and in situ DRIFTS study of the CO2 methanation mechanism using Ni/CeO2 and Ni/Al2O3 catalysts. Applied Catalysis B: Environmental, 265, 118538.

[267] . Wang, Y., Liu, Z., Confer, M. P., Li, J., & Wang, R. (2021). In-situ DRIFTS study of chemically etched CeO2 nanorods supported transition metal oxide catalysts. Molecular Catalysis, 509, 111629.

[268] . Köck, E. M., Kogler, M., Bielz, T., Klötzer, B., & Penner, S. (2013). In situ FT-IR spectroscopic study of CO2 and CO adsorption on Y2O3, ZrO2, and yttria-stabilized ZrO2. The Journal of Physical Chemistry C, 117(34), 17666-17673.

[269] . Vayssilov, G. N., Mihaylov, M., Petkov, P. S., Hadjiivanov, K. I., & Neyman, K. M. (2011). Reassignment of the vibrational spectra of carbonates, formates, and related surface species on ceria: a combined density functional and infrared spectroscopy investigation. The Journal of Physical Chemistry C, 115(47), 23435-23454.

[270] . Rizzetto, A., Piumetti, M., Pirone, R., Sartoretti, E., & Bensaid, S. (2024). Study of ceria-composite materials for high-temperature CO2 capture and their ruthenium functionalization for methane production. Catalysis Today, 429, 114478.

[271] . Aldana, P. U., Ocampo, F., Kobl, K., Louis, B., Thibault-Starzyk, F., Daturi, M., ... & Roger, A. C. (2013). Catalytic CO2 valorization into CH4 on Ni-based ceria-zirconia. Reaction mechanism by operando IR spectroscopy. Catalysis Today, 215, 201-207.

[272] . Eckle, S., Denkwitz, Y., & Behm, R. J. (2010). Activity, selectivity, and adsorbed reaction intermediates/reaction side products in the selective methanation of CO in reformate gases on supported Ru catalysts. Journal of Catalysis, 269(2), 255-268.

[273] . Karelovic, A., & Ruiz, P. (2013). Improving the hydrogenation function of Pd/γ-Al2O3 catalyst by Rh/γ-Al2O3 addition in CO2 methanation at low temperature. ACS catalysis, 3(12), 2799-2812.

[274] . Martin, N. M., Hemmingsson, F., Schaefer, A., Ek, M., Merte, L. R., Hejral, U., ... & Carlsson, P. A. (2019). Structure–function relationship for CO 2 methanation over ceria supported Rh and Ni catalysts under atmospheric pressure conditions. Catalysis Science & Technology, 9(7), 1644-1653.

[275] . Tóth, M., Kiss, J., Oszkó, A., Pótári, G., László, B., & Erdőhelyi, A. (2012). Hydrogenation of carbon dioxide on Rh, Au and Au–Rh bimetallic clusters supported on titanate nanotubes, nanowires and TiO 2. Topics in Catalysis, 55, 747-756.

[276] . Solis-Garcia, A., Zepeda, T. A., & Fierro-Gonzalez, J. C. (2022). Spectroscopic evidence of the simultaneous participation of rhodium carbonyls and surface formate species during the CO2 methanation catalyzed by ZrO2-supported Rh. Applied Catalysis B: Environmental, 304, 120955.

[277] . Magee, J. W., Palomino, R. M., & White, M. G. (2016). Infrared spectroscopy investigation of Fe-promoted Rh catalysts supported on titania and ceria for CO hydrogenation. Catalysis Letters, 146, 1771-1779.

[278] . Zeinalipour-Yazdi, C. D., Cooksy, A. L., & Efstathiou, A. M. (2007). A diffuse reflectance infrared Fourier-transform spectra and density functional theory study of CO adsorption on Rh/γ-Al2O3. The Journal of Physical Chemistry C, 111(37), 13872-13878.

[279] . Ichikawa, M., & Fukushima, T. (1985). Infrared studies of metal additive effects on carbon monoxide chemisorption modes on silicon dioxide-supported rhodium-manganese,-titanium and iron catalysts. The Journal of Physical Chemistry, 89(9), 1564-1567.

[280] . Stevenson, S. A., Lisitsyn, A., & Knoezinger, H. (1990). Adsorption of carbon monoxide on manganese-promoted rhodium/silica catalysts as studied by infrared spectroscopy. Journal of Physical Chemistry, 94(4), 1576-1581.

[281] . Zhao, Z., Kong, X., Yuan, Q., Xie, H., Yang, D., Zhao, J., ... & Jiang, L. (2018). Coordination-induced CO 2 fixation into carbonate by metal oxides. Physical Chemistry Chemical Physics, 20(29), 19314-19320.

[282] . Badri, A., Binet, C., Saussey, J., & Lavalley, J. C. (1997). In situ FT-IR study of ceria reduction by CO. In Progress in Fourier Transform Spectroscopy: Proceedings of the 10th International Conference, August 27–September 1, 1995, Budapest, Hungary (pp. 697-699). Springer Vienna.

[283] . Mino, L., Spoto, G., & Ferrari, A. M. (2014). CO2 capture by TiO2 anatase surfaces: a combined DFT and FTIR study. The Journal of Physical Chemistry C, 118(43), 25016-25026.

[284] . Pan, Q., Peng, J., Wang, S., & Wang, S. (2014). In situ FTIR spectroscopic study of the CO 2 methanation mechanism on Ni/Ce 0.5 Zr 0.5 O 2. Catalysis Science & Technology, 4(2), 502-509.

[285] . Alonso-Vante, N., & Alonso-Vante, N. (2018). Effect of Supports on Catalytic Centers. Chalcogenide Materials for Energy Conversion: Pathways to Oxygen and Hydrogen Reactions, 169-201.

[286] . Varga, E., Pusztai, P., Oszkó, A., Baán, K., Erdőhelyi, A., Kónya, Z., & Kiss, J. (2016). Stability and temperature-induced agglomeration of Rh nanoparticles supported by CeO2. Langmuir, 32(11), 2761-2770.

[287] . Gates, B. C. (1995). Supported metal clusters: synthesis, structure, and catalysis. Chemical reviews, 95(3), 511-522.

[288] . Bredy, P., Fine, L., Farrusseng, D., Schuurman, Y., & Meunier, F. C. (2023). Evolution of sample optical pathlength during diffuse reflectance FT-IR analyses. Catalysis Today, 424, 114301.

[289] . Jin, D., Hu, Q., Neuhauser, D., Von Cube, F., Yang, Y., Sachan, R., ... & Fang, N. X. (2015). Quantum-spillover-enhanced surface-plasmonic absorption at the interface of silver and high-index dielectrics. Physical review letters, 115(19), 193901.